

Seismic time-lapse interferometry across scales

Anne Obermann^{a,*}, Gregor Hillers^b

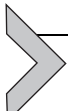
^aSwiss Seismological Service, ETH, Zurich, Switzerland

^bInstitute of Seismology, University of Helsinki, Helsinki, Finland

*Corresponding author: e-mail address: anne.obermann@sed.ethz.ch

Contents

1. Introduction	66
2. Basic principles of seismic interferometry	69
2.1 Reconstruction of the Green's function	69
2.2 Requirements for time-lapse monitoring	73
3. Noise-based interferometry	74
3.1 Spatio-temporal distribution of seismic noise sources	74
3.2 Noise-based tomographic imaging	78
3.3 Noise-based monitoring	79
4. Reflected-wave interferometry	80
5. Coda-wave interferometry (CWI)	82
5.1 Seismic coda waves	82
5.2 Different propagation regimes	84
5.3 Characteristic lengths in multiply scattering media	86
6. Detecting and locating time-lapse Changes	88
6.1 Conceptual differences between time-lapse changes in velocity and amplitude	88
6.2 Detecting time-lapse changes	89
6.3 Spatial location of CWI time-lapse changes	96
7. Applications across scales	98
7.1 Nondestructive material testing using diffuse ultrasound	99
7.2 Passive elastography: Seismology of the human body using shear waves from muscle activities	102
7.3 Monitoring applications on the local scale (meter–kilometer) using anthropogenic and oceanic noise	106
7.4 Passive monitoring at the regional scale using the ambient seismic field	118
8. Outlook	126
Acknowledgment	127
References	127



1. Introduction

The term seismic interferometry refers to the principle of reconstructing seismic responses associated with virtual sources by cross-correlating seismic wavefield records obtained at different receiver locations. The function or waveform that is obtained by cross-correlating the two receiver recordings can, under certain conditions, be interpreted as the response that would be measured at one of the receiver locations as if there was a source at the other location.

Depending on the source of the correlated seismic wavefield one can distinguish between *controlled-source interferometry* and *passive seismic interferometry* (Wapenaar, Draganov, Snieder, Campman, & Verdel, 2010). Controlled-source interferometry is mainly applied to seismic exploration data and involves the stacking of correlations associated with different active source positions (Bakulin & Calvert, 2004; Schuster, 2001). In passive seismic interferometry, deterministic seismic responses are obtained from passively recorded signals such as the ambient seismic field or noise, or the waveforms of microearthquakes (Wapenaar, Draganov, et al., 2010). Here, the explicit summation over active source signals is replaced by the implicit summation over signals resulting from the superposition of simultaneously acting uncorrelated sources.

Depending on the type of waves that are retrieved, one can further distinguish between *direct-wave interferometry* (Campillo & Paul, 2003; Sabra, Gerstoft, Roux, Kuperman, & Fehler, 2005; Shapiro & Campillo, 2004), used for the retrieval of ballistic body waves and surface waves; *reflected-wave interferometry* (Claerbout, 1968; Draganov, Campman, Thorbecke, Verdel, & Wapenaar, 2009; Draganov, Wapenaar, Mulder, Singer, & Verdel, 2007; Scherbaum, 1987b), which dominates the applications in exploration contexts; and *coda-wave interferometry* (Campillo et al., 2015; Snieder, 2006), which is the basis for time-lapse applications.

In theory, all methods allow time-lapse imaging, which refers to the construction of images at different times, i.e., dates. However, the sensitivity of the direct wave to small variations of physical properties is often limited. In practice, when studying the detection and location of small medium changes over time, a large body of work focuses on the reconstructed *seismic coda waves*. Similar to the coda of earthquakes, these long-lasting tails in the correlograms or correlation functions result from the scattering of the wave energy at the heterogeneities of the Earth (Fig. 1).

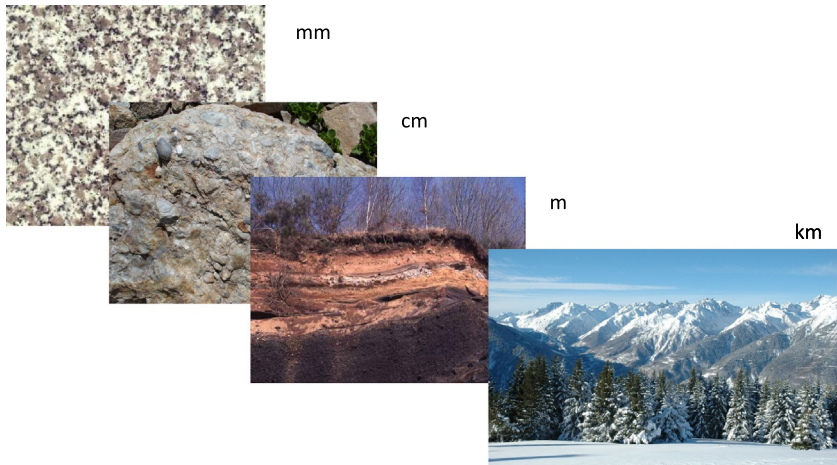


Fig. 1 Heterogeneities of the Earth at different scales ranging from mm to km lead to scattered wave propagation and are responsible for the long-lasting seismic coda waves.

Wave propagation in the presence of scattering quickly becomes complex and the travel-times of the randomly appearing coda phases do not allow the application of classic travel-time-based imaging approaches. As a consequence, seismic coda waves were often neglected until [Aki \(1969\)](#) and [Aki and Chouet \(1975\)](#) showed that coda waves contain conclusive information about regional scattering and attenuation properties.

Today, it is widely accepted that coda waves are deterministic, reproducible signals. As a consequence of scattering, coda waves sample large areas of the subsurface very densely. They are thus more sensitive to small changes in the medium compared with direct waves. This is a very relevant aspect for time-lapse monitoring that underpins the rapidly growing number of applications coda-wave interferometry ([Snieder, 2006](#)).

Reflection-interferometry was already introduced in the 1970s and 1980s ([Baskir & Weller, 1975](#); [Scherbaum, 1987a, 1987b](#)), with the main target of subsurface imaging. The method quickly expanded to various applications within exploration geophysics (e.g., [He, Hornby, & Schuster, 2007](#); [Mikesell, van Wijk, Calvert, & Haney, 2009](#); [Minato et al., 2007](#); [Wang, Luo, & Schuster, 2009](#); [Willis et al., 2006](#); [Xiao, Zhou, & Schuster, 2006](#); [Yu & Schuster, 2006](#)). In the early 2000s, [Lobkis and Weaver \(2001\)](#) and [Weaver and Lobkis \(2001\)](#) demonstrated in acoustics the possibility to reconstruct the Green's function by correlating diffuse wavefields, which motivated the subsequent applications in seismology. In seismology, interferometric

imaging and time-lapse applications then gained popularity after it was demonstrated that surface waves can be retrieved from the ambient seismic field with passive interferometry methods (Campillo & Paul, 2003; Sabra et al., 2005; Shapiro & Campillo, 2004). These works sparked numerous applications including laboratory and medical applications, nondestructive monitoring of concrete and infrastructures, reservoir monitoring for engineering projects, predictions of volcanic unrest and the assessment of crustal damage and healing processes after large earthquakes. We refer the interested reader to Wapenaar, Draganov, and Robertsson (2008) for a more detailed discussion of the historical development of seismic interferometry up to 2008.

As the applications range over various length scales, different scale dependent excitation mechanisms of the recorded seismic energy have to be considered. They can range from active or controlled sources, such as piezo-elements, hammer shots, sparkers, vibro-trucks, to passive or uncontrolled sources including earthquakes and micro-seismicity or ambient noise whose origin cannot always be unequivocally identified. In all cases, the central requirement for time-lapse applications is that the wavefield, from which the impulse response is reconstructed, are stable and time invariant to facilitate the association of observed waveform changes to changes in the medium.

This chapter is structured in two parts. In the first part, we introduce the principles underlying seismic interferometry by reviewing the three above-mentioned interferometric cases related to *direct waves*, *reflected waves*, and *coda waves*. In these introductions we focus on the aspects that are relevant for time-lapse applications. For further reading we refer to the books *Seismic Interferometry* by Schuster (2009), *Seismic Wave Propagation and Scattering in the Heterogeneous Earth* by Sato, Fehler, and Maeda (2012), and *Passive imaging with seismic noise* by Garnier and Papanicolaou (2016); the *Tutorial on seismic interferometry part I/II* by Wapenaar, Draganov, et al. (2010) and Wapenaar, Slob, Snieder, and Curtis (2010); the review article by Campillo (2006); the chapter *Crust and Lithospheric Structure—Seismic Imaging and Monitoring with Ambient Noise Correlations* by Campillo and Roux (2015), the chapters *Theoretical foundations of noise interferometry* and *Noise-Based Monitoring* in the textbook on Ambient Seismic Noise by Nakata, Gualtieri, and Fichtner (2019); and the paper *Theory of coda-wave interferometry* by Snieder (2006). In the second part, we provide a comprehensive, but again by no means complete, overview of the accomplishments of time-lapse interferometry applications across different scales. To highlight the applicability of the underlying wave physics principles we also discuss complementary applications of coda-wave interferometry from related laboratory and medical contexts.



2. Basic principles of seismic interferometry

A common aspect of interferometry is that virtual sources are created at positions where only receivers have been deployed, without requiring knowledge of either the medium parameters nor the positions of the sources that actually excite the wavefield. This procedure is also referred to as Green's function retrieval.

2.1 Reconstruction of the Green's function

We outline the basic principles for the reconstruction of the Green's function, with the help of an analogy between cross-correlations and time reversal (Derode, Larose, Campillo, & Fink, 2003; Derode, Larose, Tanter, et al., 2003). This analogy is based on the spatial reciprocity theorem (Aki & Richards, 1980) and the invariance of the seismic wave equation to time-reversed solutions (Fink, 1992). A collection of mathematically more rigorous derivations can be found, e.g., in Campillo and Roux (2015).

The following derivation considers the 2-D case analogous to the lateral propagation of surface waves or the 3-D full space, i.e., reflections on boundaries like the Earth's surface or other major interfaces are not considered. To understand the spatial reciprocity or *source-receiver reciprocity*, we consider a signal emitted by a source in point A and received in point B (Fig. 2A). For any complexity of the medium, this signal is identical to a signal emitted by a source in point B and received in point A. This implies

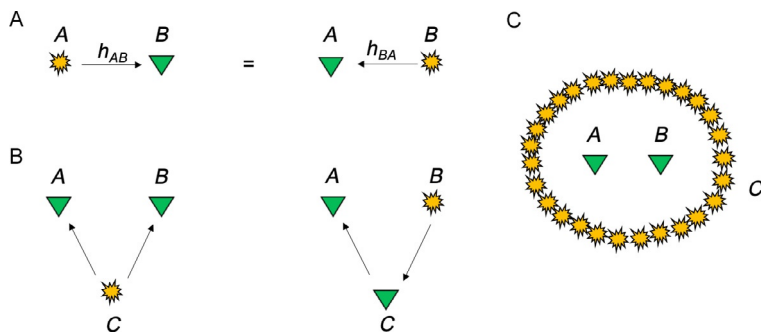


Fig. 2 Basic principles of seismic interferometry. (A) Source-receiver reciprocity. (B) Time reversal: C emits a signal that is registered by A and B. This is equivalent to a signal emitted by B, received by C and reemitted to be finally recorded by A. (C) Configuration with multiple sources C_i that surround A and B.

that interchanging the position of source and receiver does not change the properties of the waveform.

As the wave equation is symmetric, *time invariance* applies. To understand this concept, let us consider the acoustic case of the wave equation:

$$\frac{\partial^2 \phi}{\partial t^2} = c^2 \Delta \phi, \quad (1)$$

where c is the speed of the acoustic waves in the medium, ϕ the wavefield and Δ the Laplace-operator. Let $\phi(t)$ be a solution of Eq. (1). Then $\phi(-t)$, too, is a solution, as $\partial(\cdot)/\partial t^2 = \partial(\cdot)/\partial(-t)^2$. As a result of this symmetry, the minus sign implies that a “backward” propagation of waves in time is an equally viable solution.

To understand the analogy between cross-correlations and time reversal, we consider the following experiment (Fig. 2B): two receivers A and B and a source C are placed inside or at the surface of a propagation medium. The source C emits a signal $S_C(t) = e(t)$. The displacement registered in A and B corresponds to a convolution of the signal emitted at the source C with the impulse response of the medium, the Green’s function h , between A and C ($h_{AC}(t)$) and B and C ($h_{BC}(t)$):

$$\begin{aligned} S_A(t) &= e(t) * h_{AC}(t), \\ S_B(t) &= e(t) * h_{BC}(t), \end{aligned} \quad (2)$$

where the asterisk indicates the convolution operator. The correlation C between the signals registered in A and B is given by:

$$\begin{aligned} C_{AB}(\tau) &= S_A(t) * S_B(-t) \\ &= h_{AC}(t) * h_{BC}(-t) * g(t), \end{aligned} \quad (3)$$

where τ is the time of correlation and $g(t) = e(t) * e(-t)$. Note that the minus sign in $S_B(-t)$ is not associated with the physical time reversal, but with the mathematical relation between correlation and convolution. As we have seen, the wave propagation is reciprocal in space, and therefore $h_{BC}(t) = h_{CB}(t)$. Let us now consider an experiment of time reversal. The source is placed in point B and point C plays the role of a time reversal mirror. B emits an impulse that is registered in C ($h_{CB}(t)$). C then reverses this signal— $-h_{CB}(-t)$ (the minus sign is now associated with physical time reversal)—and reemits it into the medium, where A will record:

$$S_A(t) = h_{BC}(-t) * h_{AC}(t). \quad (4)$$

Note that the correlation formulation (Eq. 3) is identical to the time reversal (Eq. 4). However, both formulations depend explicitly on signals associated with the source C . Furthermore, these intermediate results have no reason to be proxies for the Green's function between A and B (h_{AB}). We thus look for a formulation of h_{AB} that is source independent.

We now consider an extension of the experiment, where instead of a unique mirror point C , we use an array of points C_i that surround A and B (Fig. 2C). A emits an impulse and the energy propagates in all directions. B will register the signal $h_{AB}(t)$ that corresponds to the Green's function that we are looking for. All the points C_i register the signal $h_{AC_i}(t)$ and reemit the time-reversed signal $h_{AC_i}(-t)$. If the number of mirror points C_i is sufficiently large and without any loss of information, there exists a time-reversed wave that propagates back to the source in point A and is registered in point B as $h_{AB}(-t)$. In other words, the time reversal experiment corresponds to the sum of the Green's functions between A and B at negative and positive times. As the time reversal is analogous to the cross-correlation, we can write:

$$\sum_{C_i} h_{AC_i}(t) * h_{C_iB}(-t) = h_{AB}(t) + h_{AB}(-t). \quad (5)$$

Eq. (5) expresses that continuously distributed stations, or, by analogy, sources, C_i as shown in Fig. 2C around A and B provide a perfect time reversal mirror in a homogeneous medium. To obtain the Green's function estimate, azimuthal averaging is implemented by stacking the correlations associated with each source. This applies also to the situation where the energy propagation is limited to the directions around the alignment of the sensors (Gouédard, Roux, Campillo, & Verdel, 2008), along the so-called end-fire lobes (Roux, Kuperman, & the NPAL Group, 2004), along which the contributions interfere constructively. In the multiple scattering regime, as opposed to the homogeneous medium, one time reversal mirror or source C is sufficient for isotropic refocusing. Correspondingly, the Green's function can be retrieved from diffuse field correlations. This is because scattering can be understood as the random excitation from secondary sources once the energy has been released into the system from that one mirror or active source. Gallot, Catheline, Roux, and Campillo (2012) and Hillers, Roux, Campillo, and Ben-Zion (2016) demonstrated the analogy of time reversal and noise correlation by reconstructing the time-reversed wavefields from correlation functions of dense array data (Fig. 3). Note that only the far-field waves are recorded and re-injected

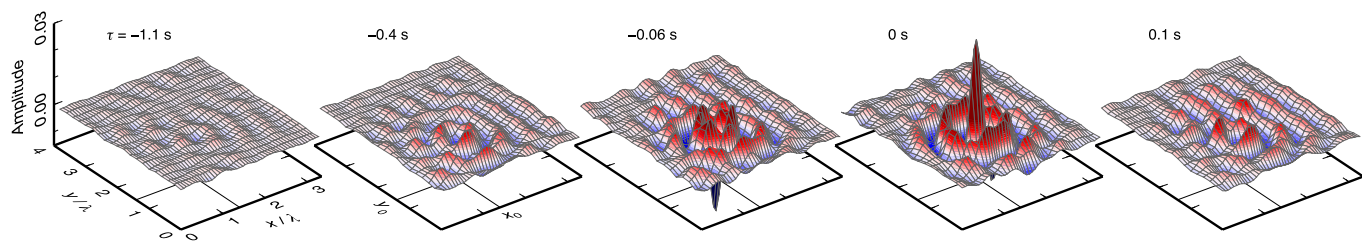


Fig. 3 Illustration of a converging, refocusing, and diverging wavefield (Hillers et al., 2016). The panels show amplitude distributions of noise correlation functions between the station at x_0, y_0 and all other 1100 stations in a dense seismic array at different correlation lag times τ . The size of the focal spot at zero lag time can be used for local imaging. Subparallel wavefronts along the y axis are associated with a similarly trending strike slip fault structure.

at the mirror locations, and therefore the refocusing waves lack the original near-field components of the Green's function (Aki & Richards, 1980). As a consequence, the refocusing or focal spot at zero time that is the superposition of the converging and diverging waves has a finite width that is related to the local phase velocity, even if the original excitation at the origin is a delta-function. Estimating the phase velocity from properties of the time-domain focal spot is related to Aki's frequency-domain Spatial Auto-correlation Method SPAC (Aki, 1957). For the connections between SPAC and cross-correlation see Tsai and Moschetti (2010).

2.2 Requirements for time-lapse monitoring

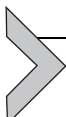
The basic premise of time-lapse monitoring is straightforward. Repeated surveys are performed with the aim of understanding changes in the volume of interest over time. During these repeated surveys, the difference in acquisition parameters has to be minimal. To reduce random noise, sensors and recorded wavefields are ideally stationary and fluctuations in the frequency content should also be minimal.

The observations made in seismic time-lapse studies frequently include changes in amplitude and changes in travel-time that can for instance be associated with changes in stress or pore pressure/pore filling. Typically, the better the survey repeatability, the smaller the detection threshold for the changes.

Seismic 4-D Time-Lapse Monitoring started to be used in the petroleum industry in the early 2000s and has gained considerable popularity. The understanding of changes in the oil and gas reservoirs over time, and particularly their behavior during production, can increase the recovery factor of a reservoir and thus have a tangible economic effect. In the exploration context, hundreds to thousands of seismic sensors are fully buried and/or cemented in during the entire production cycle. As repeatable sources, typically vibro-trucks are used and the standard workflow of seismic image processing is applied to the reconstructed reflection waveforms.

While this method is very successful in terms of sensitivity and resolution, it is also expensive and unfeasible over large areas, or in the presence of topography. For many small-scale engineering applications, such as Enhanced Geothermal Systems, as well as for academic or civil defense projects targeting the monitoring of volcanoes, earthquake faults, and other active tectonic phenomena, budget considerations can impose significant constraints. In these cases, and for surveys in environmentally sensitive or

densely populated areas, interferometric methods, and in particular the Green's function retrieval from the ubiquitous ambient seismic field, are essential.



3. Noise-based interferometry

As [Curtis, Gerstoft, Sato, Snieder, and Wapenaar \(2006\)](#) appropriately put it, “turning noise into data” is every geophysicists’ dream. While the foundations for interferometry were laid around the 1960s with the publications by [Aki \(1957\)](#) on the earlier mentioned SPAC method and by [Claerbout \(1968\)](#), it was not until the early 2000s that interferometry made its entry to the field of seismology. [Campillo and Paul \(2003\)](#) first showed the emergence of surface waves from cross-correlations of earthquake coda waves. Then [Shapiro and Campillo \(2004\)](#) and [Sabra, Roux, and Kuperman \(2005\)](#) used ambient seismic noise for the Green’s function reconstruction for tomographic imaging purposes. These discoveries persistently changed the way researchers now think about the “noisy” records that were typically discarded for most analyses. At the same time, developments in sensor technology and data storage and retrieval capacities have been fueling these developments by providing the actual raw observations—high-quality continuous records of the spatially densely sampled ambient field. Increasingly available computational facilities provide the processing power to turn these records efficiently into signal.

Seismic coda waveforms and long time series of seismic noise recordings can now be turned into coherent signals, which opens up numerous possibilities for applications in seismology. These applications can be roughly grouped into the three main topics; noise source studies, tomographic imaging, and time-lapse monitoring.

3.1 Spatio-temporal distribution of seismic noise sources

Several studies have made the attempt to characterize ambient seismic noise ([Friedrich, Kruger, & Klinge, 1998](#); [Nishida, Kobayashi, & Fukao, 2002](#); [Stehly, Campillo, & Shapiro, 2006](#)). [Gutenberg \(1936\)](#) already pointed out that the seismic noise intensity follows the atmospheric activity and the motion of the sea. These observations imply that the ambient field is generated at the Earth surface, which explains why the dominant part of the noise energy propagates as surface waves ([Friedrich et al., 1998](#)).

The origin of the ambient wavefield then depends strongly on the frequency range and location (Bonnefoy-Claudet, Cotton, & Bard, 2006). The ambient noise spectrum is dominated by the double-peak in the frequency range between 1 and 20 s that is associated with microseisms energy. The less energetic, single-frequency microseisms peak at periods around 14 s is a consequence of direct interactions between coastal seas and shallow bathymetry. The stronger double-frequency peak at 7 s results from nonlinear wave–wave interactions between ocean gravity waves that travel in opposite direction (Hasselmann, 1963; Longuet-Higgins, 1950). Opposing wave patterns arise through two primary mechanisms. First, they can occur when a (generally very small) fraction of the incoming wave incident on a coastline is reflected back, seawards (Bromirski & Duennbier, 2002; Elgar, Herbers, & Guza, 1994; Friedrich et al., 1998; Yang & Ritzwoller, 2008). The second important mechanism for opposing wave patterns is by association with mid-latitude storm systems (Kedar et al., 2008) and tropical cyclones (Zhang, Wen, Shen, & Chen, 2010) in the open oceans (Cessaro, 1994; Chevrot et al., 2007; Stehly et al., 2006).

Pressure fluctuations induced by waves with the same period propagating in opposite directions are modulated by the height of the resonating water column. The transmitted microseisms energy therefore depends on ocean wave state and bathymetry (Ardhuin, Stutzmann, Schimmel, & Mangeney, 2011; Kedar et al., 2008) which leaves a climate imprint on seismic noise properties (Stutzmann, Schimmel, Patau, & Maggi, 2009). Modern satellite imagery of the ocean wave state thus allows a detailed modeling of the microseisms excitation (Ardhuin, Gualtieri, & Stutzmann, 2015; Tolman, 2014).

Both microseisms peaks are dominated by fundamental mode surface waves (Landès, Hubans, Shapiro, Paul, & Campillo, 2010). Data from dense seismic arrays has shown that teleseismic body waves are also present in the secondary microseisms (e.g., Backus, Burg, Baldwin, & Bryan, 1964; Iyer & Healy, 1972). Their excitation can be associated with specific storms (Gerstoft, Fehler, & Sabra, 2006; Gerstoft, Shearer, Harmon, & Zhang, 2008). Because the energetically most relevant seismic noise results from a nonlinear interaction of solid Earth with the fluid outer layers of the planet, the microseisms excitation pattern and properties show a distinct, non-random seasonality (Hillers, Graham, et al., 2012; Landès et al., 2010; Schimmel, Stutzmann, Ardhuin, & Gallart, 2011; Stehly et al., 2006; Tanimoto, Ishimaru, & Alvizuri, 2006), which finds a similar expression in the associated microbaroms excitation (Landès, Le Pichon, Shapiro, Hillers, & Campillo, 2014) (Fig. 4).

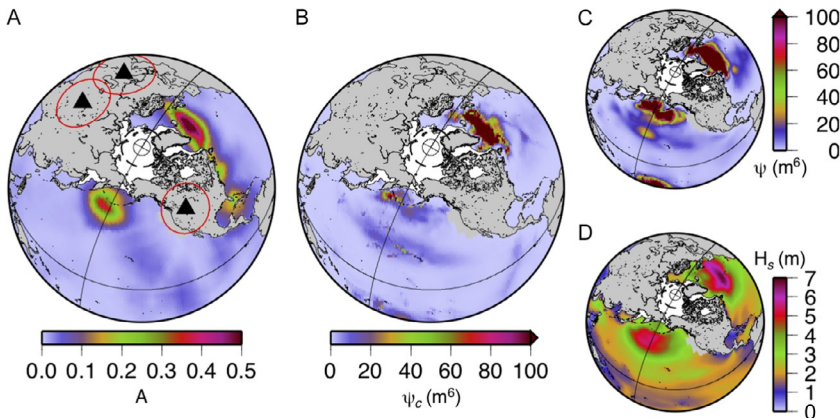


Fig. 4 An example microseism excitation pattern of a 13 day observation window centered on 8 December 2000. (A) Seismological observations, A. (B) Wave–wave interaction modulated by bathymetry, Ψ_c . (C) Original wave–wave interaction Ψ , not modulated by bathymetry. Such patterns are now produced by wave action models based on satellite observations of the ocean wave state. (D) Significant wave height, H_s . White areas denote monthly averaged sea ice coverage, the dashed circle depicts the boundary of the modeling domain (78°N to 78°S), and red circles delineate the minimum back projection range (15°) around each network. From Hillers, G., Graham, N., Campillo, M., Kedar, S., Landè, M., & Shapiro, N. (2012). Global oceanic microseism sources as seen by seismic arrays and predicted by wave action models. *Geochemistry, Geophysics, Geosystems*, 13(1), 1–19.

At frequencies above 1 Hz, a range of natural and anthropogenic excitation mechanisms contribute to the ambient field. Natural phenomena include mostly wind acting on topographic irregularities (Hillers & Ben-Zion, 2011; Withers, Aster, Young, & Chael, 1996), as well as precipitation and runoff (Burtin, Bollinger, Vergne, Cattin, & Nabělek, 2008). Anthropogenic mechanisms are often associated with traffic and industrial activity that leave a distinct 7-day periodicity in the properties of high-frequency ambient noise properties, which is of course related to the synchronized human activities (Hillers, Campillo, Lin, Ma, & Roux, 2012; Inbal et al., 2018; Lewis & Gerstoft, 2012; Ringdal & Bungum, 1977; Young, Chael, Withers, & Aster, 1996).

Theoretically, the reconstruction of the Green’s function from noise correlations is based on the assumption of an equipartitioned wavefield (Section 5.2). This asymptotic regime implies isotropic propagation directions. In most applications, however, both a ballistic and a diffusion component coexist (Hillers, Campillo, et al., 2012; Larose, Roux, & Campillo, 2007). As a consequence of the directional energy flux—which can also prevail if the ballistic component is small or even negligible—the retrieved

function is asymmetric. In these cases, the cross-correlations have not converged to the Green's function. This imperfect Green's function reconstruction leads many authors to prefer the term “cross-correlation computation” or “empirical Green's function estimates” over “Green's function retrieval”. However, [Hadzioannou, Larose, Coutant, Roux, and Campillo \(2009\)](#) and others have demonstrated that the noise propagation directions homogenize reasonably well when averaged over sufficiently long periods. The homogenization and randomization of the noise wavefield is enhanced by the scattering of the seismic waves on the heterogeneities that act as secondary sources. The need for the noise wavefield to randomize, which in practice involves the stacking of records over sufficiently long time-intervals, introduces a frequency dependent limit of the time resolution ([Larose et al., 2007](#)). The concept of stacking over different flux directions is applied in [Campillo and Paul \(2003\)](#), [Paul, Campillo, Margerin, Larose, and Derode \(2005\)](#), [Hillers et al. \(2016\)](#), [Chaput, Clerc, Campillo, Roux, and Knox \(2016\)](#), and [Hillers and Campillo \(2018\)](#), where cross-correlated earthquake coda signals are stacked over a range of source azimuths. [Gouédard et al. \(2008\)](#) also illustrate the effects of ballistic and diffusive propagation on the azimuthally variable properties of the obtained cross-correlations.

We emphasize that anisotropic noise propagation directions do not only lead to asymmetric amplitudes in the reconstructed ballistic arrivals as illustrated in [Fig. 5](#), but can also introduce a systematic arrival time error

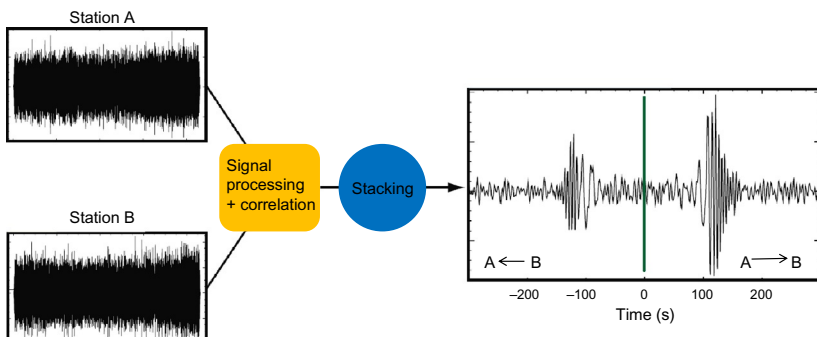


Fig. 5 Illustration of the Green's function reconstruction from seismic noise recorded at station A and B. After data specific processing steps, the records are correlated and stacked to obtain the correlation shown on the right-hand side. We can see the causal (right) and anticausal (left) part of the fundamental Rayleigh waves. The positive times correspond to a wave that propagated from station A to station B, and vice versa for the negative times.

(Froment et al., 2010; Weaver, Froment, & Campillo, 2009). This typically inhibits the resolution of changes in the subsurface velocity structure using time dependent or 4-D imaging. Techniques to mitigate these effects include the iterative correlation approach (Froment, Campillo, & Roux, 2011) and the scaling of the covariance matrix eigenvalue spectrum (Seydoux, de Rosny, & Shapiro, 2017), which can be considered as “directional whitening.” This is in reference to the spectral whitening (Bensen et al., 2007) that is typically employed during the preprocessing stage (Fig. 5) to equilibrate the variable spectral amplitude distribution of the original field. On the other hand, the multiply scattered waves in the noise correlation coda—which are deterministic in the sense that they can be reconstructed at different times because they are an integral part of the medium impulse response—allow high-precision monitoring even if the azimuthal distribution of the noise propagation direction varies (Colombi et al., 2014).

3.2 Noise-based tomographic imaging

Shapiro, Campillo, Stehly, and Ritzwoller (2005) and Sabra et al. (2005) introduced passive seismic surface wave imaging using data from California. This and follow-up work impressed through the obtained high spatial resolution of the method that exceeds the resolution of regional earthquake tomographies simply—but importantly—because the controlled interstation coverage outperforms the sparse illumination with earthquake waves. Since then, surface waves from ambient seismic noise correlations have been used extensively for high-resolution imaging of the lithosphere in many regions; for example, in Europe: Villaseñor, Yang, Ritzwoller, and Gallart (2007), Yang, Ritzwoller, Levshin, and Shapiro (2007); the Americas: Moschetti, Ritzwoller, and Shapiro (2007), Bensen, Ritzwoller, and Shapiro (2008), Ekström, Abers, and Webb (2009), Lin, Ritzwoller, and Snieder (2009), Lin and Ritzwoller (2011), Gaite, Iglesias, Villaseñor, Herraiz, and Pacheco (2012), Ward et al. (2013); Asia: Kang and Shin (2006), Zheng, Sun, Song, Yang, and Ritzwoller (2008), Li, Su, Wang, and Huang (2009); New Zealand and Australia: Lin, Ritzwoller, Townend, Savage, and Bannister (2007), Saygin and Kennett (2010), Arroucau, Rawlinson, and Sambridge (2010).

However, surface waves are not sufficient for exploring the deep structure of the Earth, as they have limited depth resolution. There are different approaches to overcome this limitation. By merging noise correlations and earthquake records the frequency band could be extended, and hence the depth of the investigation (Yang, Li, & Ritzwoller, 2008; Yang, Ritzwoller, Lin,

Moschetti, & Shapiro, 2008; Yao, van der Hilst, & de Hoop, 2006). In some cases, phase velocities of waves with lengths that exceed the network aperture can be extracted from the reconstructed, collapsed surface wavefield (Hillers et al., 2016), which also offers an increase in depth resolution. Roux, Sabra, Gerstoft, and Kuperman (2005) showed that P-waves can be reconstructed using noise correlations at local scale. Large-N arrays facilitate beamforming methods for local P-wave reconstruction (Brenguier et al., 2016). Using dense regional arrays, Lin, Tsai, Schmandt, Duputel, and Zhan (2013), Poli, Pedersen, and Campillo (2012), Ruigrok, Campman, and Wapenaar (2011), and Zhan, Ni, Helmberger, and Clayton (2010) showed the emergence of crustal body wave reflections from noise correlations. Poli, Campillo, Pedersen, and POLENET LAPNET Working Group (2012) could as well extract reflections from the mantle transition zone and Lin et al. (2013) from the core-mantle boundary. Going beyond the local and regional scale Nishida (2013) and Boué et al. (2013) succeeded in extracting global body wave propagation (of P, PP, PKP, S, SS, ScS, P'P', etc. waves).

As stated, noise-based tomographic imaging can be performed in 4-D, but the changes in the subsurface velocity structure must exceed the arrival time uncertainty of the repeatedly reconstructed direct or ballistic surface waves that are associated with variable noise excitation patterns. As a result, only few applications perform time-lapse imaging using ballistic waves (De Ridder & Biondi, 2013; Mordret, Shapiro, & Singh, 2014). Despite the progress in noise-based monitoring and imaging techniques discussed in the following pages, there is still considerable incentive to push for 4-D tomography. This is because tomographic imaging is an established method, its resolution well understood, and work flows have been thoroughly tested and implemented. On the other hand, the mapping of the signals obtained with coda-wave interferometry is a subject of active research programs.

3.3 Noise-based monitoring

The overwhelming majority of noise-based monitoring applications are, however, not based on repeated tomographic images, but on studies of the changes of phase and/or amplitude in the reconstructed Green's function coda waveforms (Fig. 6). With these coda waveforms, relative seismic wave speed changes as small as 10^{-4} can be resolved (Mao et al., 2019; Wang et al., 2017). As stated, this approach benefits from the insensitivity of the coda wave arrival times to changes in the flux direction (Colombi et al., 2014), and from the relatively fast—frequency dependent—convergence time that

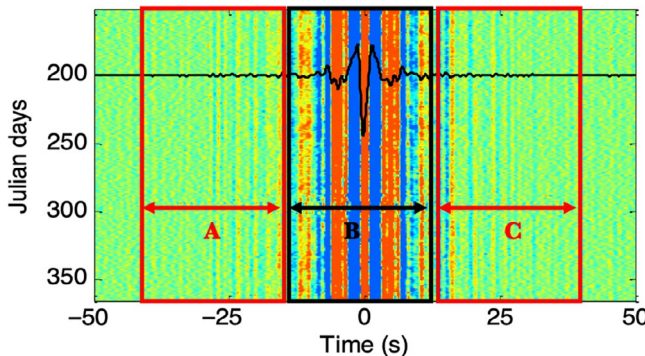
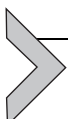


Fig. 6 Six months of daily cross-correlations of two nearby stations. While noise-based tomographic imaging focuses on the surface wave arrivals (B), monitoring applications target the acausal (A) and causal (C) parts of the coda.

now facilitates hourly resolution from dense array data (Mao et al., 2019). The past decade has seen numerous applications from a wide range of scales that together demonstrate the robustness and versatility of continuous cross-correlation based monitoring, which will be detailed in the second part of this chapter.



4. Reflected-wave interferometry

In this section, we outline the basic concept of 1-D reflection interferometry for a single reflector. For more detail on how the method deals with multiple reflections, or how it can be extended to a 2-D and 3-D analysis, we refer to the tutorial by Wapenaar, Draganov, et al. (2010) or the text book on seismic interferometry by Schuster (2009).

The basic concept of reflection interferometry can be well understood with Fig. 7 that is used on the front cover of Schuster's book on seismic interferometry. The signal from a subsurface source is recorded at a first receiver (Fig. 7A). At the same time, parts of this signal are reflected downward by the surface. After interacting with a scatterer, or an interface/plane in 2-D/3-D, the signal is again reflected upwards and recorded by a second receiver (Fig. 7B). When these two signals are cross-correlated (denoted by the cross), the common path from the source to the first receiver is eliminated. What remains is a reflected wave recorded at the second receiver from a virtual source at the first receiver (Fig. 7C). The position of the actual source does not need to be known but should in 1-D lie below

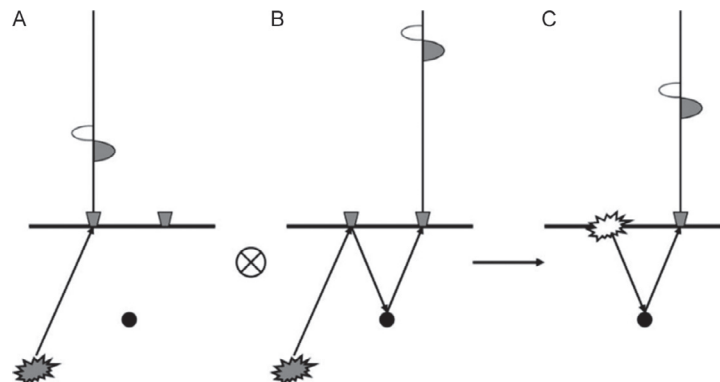


Fig. 7 Basic concept of reflection interferometry. (A) The signal from a subsurface source is recorded at the first receiver. (B) A signal from the same source is reflected downwards at the surface, then upwards at a scatterer and finally recorded by the second receiver. (C) Cross-correlating the previous signals eliminates the common propagation path from the source to the first geophone. The result is interpreted as a reflection response of a source at the first receiver position. *From Schuster, G. (2009). Seismic interferometry. Cambridge University Press.*

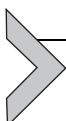
the lowest interface. The first applications of this concept date back to the 1980s and 1990s (Baskir & Weller, 1975; Scherbaum, 1987a, 1987b).

Schuster (2001) showed that by using reflection interferometry, it is possible to reposition (redatum) sources without knowing the velocity model and the position of the original sources, with a process that comes directly from the data. Many others were inspired by his work and developed interferometric methods for exploration geophysics (He et al., 2007; Mikesell et al., 2009; Minato et al., 2007; Wang et al., 2009; Willis et al., 2006; Xiao et al., 2006; Yu & Schuster, 2006). A widely used operation for instance, is the subtraction of surface waves predicted by interferometry from exploration data (Curtis et al., 2006; Dong, He, & Schuster, 2006; Halliday, Curtis, Robertsson, & van Manen, 2007). All possible interferometric transformations are discussed in Schuster (2009).

The method can also be extended to passive noise measurements. Draganov et al. (2007) demonstrated that ambient seismic noise can be turned into virtual exploration seismic reflection data. However, passive lapse-time reflection interferometry has to demonstrate its stability before it will be widely accepted as an alternative or complementary processing tool in exploration contexts.

With reflection interferometry, information hidden in noise or in a complex scattering coda can be reorganized into responses that are easier to

interpret and further process. In other words, the subsurface below a complex overburden can be imaged without knowledge of overburden velocities and near-surface changes (Mehta, Sheiman, Snieder, & Calvert, 2008). It is therefore not surprising that the majority of reflection-interferometry applications target the imaging of the subsurface, in contrast to the more limited applications of time-lapse studies (Draganov, Heller, & Ghose, 2012; Mehta et al., 2008; Zhou et al., 2010).



5. Coda-wave interferometry (CWI)

5.1 Seismic coda waves

When studying a regional seismogram (Fig. 8), we often observe that the P-, S-, and surface wave arrivals are followed by a long-lasting wave train in the tail portion of the seismogram. This wave train is named “coda,” which literally means tail. Coda waves can last more than 10 times the travel-time of direct waves, before reaching the level of seismic noise (Aki, 1969). As it is impossible to model or compute the coda waveform because of the incomplete knowledge of all small-scale heterogeneities, arrival times of coda waves cannot be used with classical imaging techniques; and for a long time it was thought that it was not possible to obtain any useful information from them.

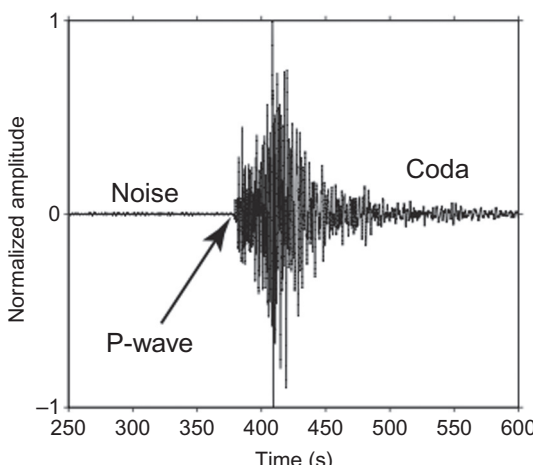


Fig. 8 Record of a seismic trace. It consists of low-amplitude noise and a large-amplitude earthquake signal that begins with the arriving P-wave (the secondary S wave arrival cannot be discerned) and fades out with the decaying coda wavetrain.

[Aki \(1969\)](#) and [Aki and Chouet \(1975\)](#) showed that the energy decay of coda waves with time is a local characteristic parameter, independent of the magnitude and location of the source. They suggested that in a frequency band of 1–10 Hz the energy envelope of the coda decay can be well described by

$$E_\omega(t) \approx \frac{1}{t^\gamma} \exp\left(-\frac{\omega t}{Q_c(\omega)}\right), \quad (6)$$

where $1/t^\gamma$ is a geometrical factor with γ varying between 1 and 2. ω is the pulsation and Q_c is called coda quality factor. Q_c is an empirical parameter that depends on the local characteristics of the crust and on frequency. Q_c is given by a combination of intrinsic (Q_i) and scattering (Q_s) attenuation:

$$\frac{1}{Q_c} = \frac{1}{Q_i} + \frac{1}{Q_s}. \quad (7)$$

$Q_i = \omega \tau_a$ where τ_a is the characteristic time for energy absorption and $Q_s = \omega H^2/D$, where $D = \frac{\nu \ell^*}{2}$ is the diffusion constant depending on the transport mean free path ℓ^* and the wave speed ν . H is a characteristic scale for the thickness of the crust. Since these discoveries, measurements of Q_c have been widely explored to study attenuation properties of the crust throughout the world. Typical Q_c values vary between 50 and 1000 ([Jin & Aki, 1988](#); [Singh & Hermann, 1983](#)). It still remains very difficult to measure Q_s and Q_i separately ([Del Pezzo, Bianco, & Saccorotti, 2001](#)) and thus to determine ℓ^* from attenuation measurements on seismic waves.

[Aki \(1969\)](#) and others ([Aki & Chouet, 1975](#); [Herranz & Espinoza, 1997](#); [Sato, 1977](#)) suggested that the coda was composed of a sum of incoherent waves that are singly scattered from heterogeneities in the Earth's crust. [Hoshiba \(1997\)](#) showed that a combination of single scattering and attenuation can account for some aspects of the seismic coda. However, the Earth is not a simple homogeneous medium with a few scattering points, but on the contrary, heterogeneous at different scales. The scattering of a wave depends on the difference in constitutive parameters between scatterers and the bulk of the propagating medium, such as the wave velocity, and the shape and size of the scatterers compared to the wavelength. [Margerin, Campillo, Shapiro, and van Tiggelen \(1999\)](#) studied the decay of Q_c with earthquake data acquired in Mexico. They could explain the decay of Q_c with a model of guided waves in the crust and scattering. [Hennino et al. \(2001\)](#) resolved the controversy “single or multiple scattering in the seismic coda” in favor of multiple scattering. They

measured the equipartitioning of the energy of seismic coda waves over the different elastic modes (P- and S-waves) from earthquake data in Mexico. In a continuation of these works, [Larose, Margerin, van Tiggelen, and Campillo \(2004\)](#) observed the interference of multiply scattered waves by measuring the weak localization of seismic waves.

The amplitude decay of coda wavetrains holds information about the scattering properties of the propagation medium. However, as random as the signal might seem, coda waves are deterministic. If the medium and the source remain unchanged, the waveform also remains the same from one record to an other. It follows from the multiple scattering process that coda waves sample the medium more efficient compared to direct waves, simply because coda waves spend more time in the medium. This repeated sampling amplifies signatures of weak medium perturbations in the coda-wave properties. So even if the changes are not detectable in the first arrivals, they may become detectable in the coda in the form of small phase-shifts or changes in amplitude. In recent years this sensitivity has been increasingly used for monitoring purposes, and is referred to as *Coda Wave Interferometry* ([Poupine, Ellsworth, & Frechet, 1984](#); [Snieder, 2006](#); [Snieder, Grêt, Douma, & Scales, 2002](#)).

5.2 Different propagation regimes

We explain the different propagation regimes introduced earlier in more detail because understanding the mode of propagation in a given situation is essential to assess the imaging and monitoring resolution limits. Wave propagation in heterogeneous media is governed by the degree of material heterogeneity. The heterogeneity leads to different propagation regimes: single scattering, multiple scattering, and diffusion, and Anderson localization ([Fig. 9](#)). We consider an impulsive source and a receiver at distance L ([Fig. 9](#)) in media with varying degrees of scattering.

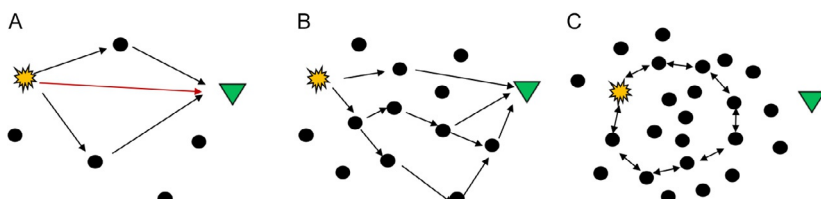


Fig. 9 Different propagation regimes. (A) Ballistic wave propagation and single scattering. (B) Multiple scattering. (C) Anderson localization.

- *Ballistic wave propagation*: As the term “ballistic” suggests, this refers to the wave that travels directly between the source (the “shot” point) and the receiver ([Fig. 9A](#), red arrow). Ballistic implies computable in a closed form, in contrast to the statistical evaluation of multiply scattered energy. In this sense, ballistic waves also include reflections from impedance contrasts.
- *Single scattering*: In the single scattering regime, the relative distance between source, receiver, and scatterers, compared to the wavelength leads to a simple interaction of the wave with a scatterer ([Fig. 9A](#)). Classic inversion techniques can be used to image the position of the scatterer.
- *Multiple scattering and diffusion* ([Fig. 9B](#)): In this regime, there are either many more scatterers in the medium or the distance between source and receiver is so large that the waves are reflected multiple times before being recorded and “forget” about their origin. In this case the equivalence between travel-time and distance cannot be resolved, which makes classical imaging techniques not applicable. Multiple scattering is also illustrated in [Fig. 10](#) which shows snapshots of a finite difference simulation of the diffusion of a circular acoustic wave in a 2-D scattering medium. Eventually, the multiply scattered energy propagation can be described by a diffusion process ([Campillo, 2006](#)).

As a first approximation, the solution of the diffusion equation for the intensity propagation between a source S and receiver R at time t reads

$$p(S, R, t) = \frac{1}{\sqrt{4\pi Dt}} e^{\frac{-\|S-R\|^2}{4Dt}} \quad (8)$$

where D is the previously mentioned diffusion constant that depends on the medium heterogeneity. Eq. (8) stands for 2-D infinite media. To take the free surface into account, a semiinfinite space has to be considered. In this case, the solution is found in terms of the sum of the infinite medium solution and its mirror image from the free surface.

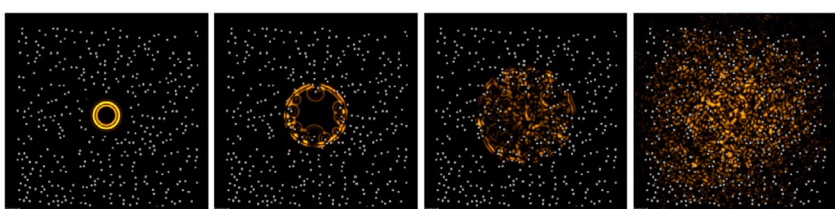


Fig. 10 Finite difference simulation of the scattering of a spherical acoustic wave in a 2-D diffusive medium. The scatterers represented by the white points have a diameter of $\lambda/2$. Source: M. Tanter, ACEL, LOA-ESPCI.

We note that the diffusion equation is associated with a statistically averaging dissipation process and does not describe a time-invariant process as the wave equation (Eq. 1). The diffusion equation describes the energy or intensity flux where all phase information is lost. Making the connection to the discussion in Section 2.1, the backward propagating wavefield can be computed from the diffused state shown in the last picture in Fig. 10 because this is of course a fully deterministic solution obtained by stepping through the wave equation.

- *Diffusion and equipartition:* Equipartition describes the wavefield state at which all possible modes are randomly excited with equal weight on average (Campillo, 2006; Hennino et al., 2001). All possible modes emerge through scattering, and the back-and-forth conversion from one wave type to another through scattering eventually equilibrates. Intuitively, only this state allows the reconstruction of the medium Green's function by cross-correlation. However, equipartition can only be an asymptotic regime in an open and attenuating system like the Earth's crust. Equipartition implies equilibration of energy ratio markers such as H^2/V^2 (Hennino et al., 2001; Shapiro et al., 2000; Weaver, 1982), but the converse statement does not hold (Paul et al., 2005), because a stable ratio can also result from a constant acting excitation mechanism. Typically it can thus not be concluded that an observed time independent H^2/V^2 time series is a signature of equipartition, but the stabilized energy ratio is a good indicator “that the field is entering a regime in which total energy is described by a diffusion” (Campillo, 2006), which supports correlation-based monitoring.
- *Anderson localization* (Fig. 9): For completeness, we also mention the regime of strong localization, also referred to as Anderson localization. In this regime, the wave energy is trapped by the ambient disorder and there is a total absence of diffusion. The phenomenon results from the wave interference between the different scattering paths. In the strong scattering limit, no signal will reach the receiver because the interferences confine the waves inside the disordered medium (Anderson, 1958). However, this regime is commonly studied in condensed matter physics, but not in seismology because of absorption and therefore not relevant for the applications discussed here.

5.3 Characteristic lengths in multiply scattering media

Besides the wavelength λ and the medium dimension L , there are three characteristic lengths that are important in wave propagation in disordered

media: the scattering mean free path ℓ , the transport mean free path ℓ^* and the absorption length ℓ_a (van Rossum & Nieuwenhuizen, 1999).

- *The scattering mean free path ℓ* corresponds to the average distance between successive scattering events. The magnitude of the scattering mean free path depends on the characteristics of the heterogeneous medium and is defined via the total cross section of interaction σ as:

$$\ell = \frac{1}{n\sigma} \quad (9)$$

with

$$\sigma = \int \frac{d\sigma}{d\Omega} d\Omega \quad (10)$$

where n is the number of scatterers per unit volume, $d\sigma$ is the differential cross section and $d\Omega = \sin(\theta)d\theta d\phi$. Note that in a 3-D medium the effective cross section is a surface, while it is a length in a 2-D medium. The medium has “weak” disorder as long as $\ell > \lambda$.

- *The transport mean free path ℓ^** is the characteristic distance along which a wave keeps memory of its incident propagation direction. ℓ^* is closely related to ℓ :

$$\ell^* = \frac{\ell}{1 - \langle \cos(\theta) \rangle} \quad (11)$$

where θ is the angle between the vector of the incident wave and the vector of the scattered wave. $\langle \cos(\theta) \rangle$ is the anisotropy of diffusion and the brackets denote averaging over all solid angles. The physics are subtly different: while ℓ is determined by superposition of the different paths, ℓ^* is also sensitive to interference. Hence, if the differential effective section is isotropic, then $\langle \cos(\theta) \rangle = 0$ and $\ell^* = \ell$.

- *The absorption length ℓ_a* for a system of size $L > \ell_a$ indicates that the waves are significantly absorbed and damped. The expression for ℓ_a is given by:

$$I \propto \exp\left(-\frac{t}{\tau_a}\right) = \exp\left(-\frac{\ell}{\ell_a}\right) \Rightarrow \ell_a = c\tau_a \quad (12)$$

where τ_a is the characteristic absorption time and c is the propagation velocity.

Wave propagation in highly heterogeneous media can be described by the diffusion approximation. The diffusive regime is constrained by the relation of four length scales (Kaveh, 1991):

$$\lambda \ll \ell, \ell^* \ll L \ll \ell_a \quad (13)$$

First, a wavelength that is significantly smaller than the transport mean free path, $\lambda \ll \ell^*$, implies that two consecutive scattering events of the wave are independent. Second, the transport mean free path is significantly smaller than the medium dimension, $\ell^* \ll L$. This is the condition for the multiple scattering regime. Third, the medium dimension is significantly smaller than the absorption length, $L \ll \ell_a$ neglects absorption or dissipation. In practice, the conditions in an open infinite space yield $\lambda \ll \ell^* \leq \ell_a$. The description of the wave propagation of multiply scattered waves with the diffusion approximation is crucial for the accurate localization of time-lapse changes (Section 6.2).

6. Detecting and locating time-lapse Changes

6.1 Conceptual differences between time-lapse changes in velocity and amplitude

There are two types of changes that are detectable in seismic waves: changes in travel-time (phase-shifts) and changes in amplitude or waveform shape (waveform coherence) (Fig. 11).

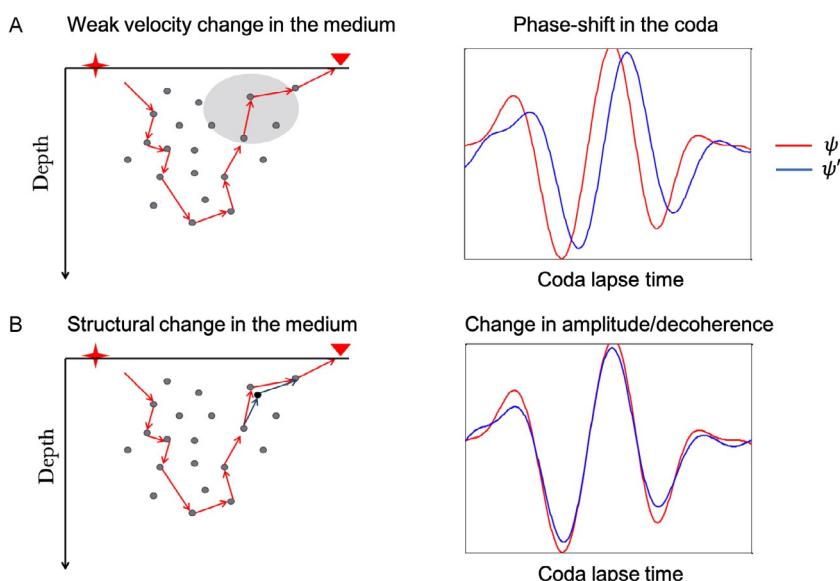


Fig. 11 Conceptual differences between a localized change in the mechanical parameters (gray area) that causes a change in the velocity (phase-shift) and a change in the scattering pattern (structural change) that results in the distortion of the waveform amplitude and/or shape.

In Fig. 11A, the gray area indicates a weak local velocity change. When comparing a wave that passed the medium prior to the appearance of the change Ψ (red), with a wave that passed after the perturbation Ψ' , an arrival time-shift dt is observed at a certain lapse-time t . Such a change in travel-time can often be attributed to variation in the fluid and rock velocities, because of changes in pore pressure (therefore, also in effective or differential pressure) or changes in rock stress because of deformation of the surrounding material.

In Fig. 11B, a structural change in the medium is sketched in the form of an alternative scatterer. This structural change will result in a change in waveform, also referred to as a loss of waveform coherence or decoherence. Changes in amplitude or shape can be used to monitor material damage in form of crack appearance; or fluid migration, as the reflection character changes as a result of replacing for example oil/water with gas (Obermann, Kraft, Larose, & Wiemer, 2015) and therefore changing the scattering properties of the material/subsurface.

In experiments with active sources, the waveform coherence can be directly measured by correlating the signals at different stages of the experiment. Studies analyzing changes in waveform coherence are mainly used in laboratory experiments and for nondestructive testing (Larose, Planès, Rossetto, & Margerin, 2010; Michaels & Michaels, 2005; Planès & Larose, 2013; Rossetto, Margerin, Planès, & Larose, 2011), to quantify defects in materials that are much smaller than one wavelength. These concepts are now also applied in seismology (Obermann et al., 2014, 2015; Obermann, Planès, Larose, & Campillo, 2013; Sanchez-Pastor, Obermann, & Schimmel, 2018).

6.2 Detecting time-lapse changes

For all time-lapse applications, an estimate of the medium reference state is typically used against which the results of continuous measurements can be compared. Let us imagine a spatially homogeneous global velocity change in a medium. This change in the medium will show its signature in the form of a time-shift dt in the (later) arriving waves. In the case of a global velocity change, the time-shift increases proportionally with the time t that the waves spent in the medium. As stated, sufficiently large velocity variations can be resolved from the phase-shift of the first arrivals. If the velocity variation is homogeneous in the medium, the relation between dt and t is linear: $dt/t = \text{const}$. At a constant distance, a negative arrival time change associated with earlier arriving phases translates then directly into a positive, i.e., faster, velocity anomaly

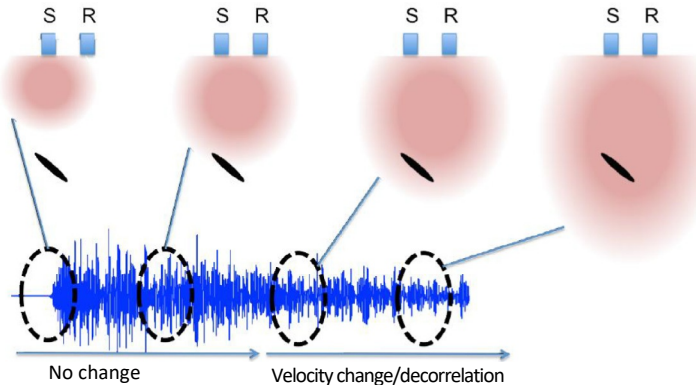


Fig. 12 Schematic view of the spatio-temporal sensitivity of coda waves to a local change (black oval). The diffusive halo of waves propagating in the medium is represented in *brown*. Its characteristic size is governed by \sqrt{Dt} , where D is the diffusion constant in the medium and t the time in the coda. At early times in the coda, the waves propagating from the source S to the receiver R have hardly felt the change. Later on, the waves have likely encountered the change and the coda is partially delayed.

$$dv/v = -dt/t. \quad (14)$$

In many cases, medium perturbations are not global changes with respect to the sampled domain, but remain spatially limited (Fig. 12). In these cases, the linear relationship described in Eq. (14) does not hold and the amplitude of the observed travel-time change ε_{app} does not correspond to the amplitude of the actual velocity change $\frac{dv}{v}$. The measured ε_{app} is influenced by the time in the coda, the position of the change relative to the couple of receivers i and the intensity of the local change $\frac{dv}{v}(x)$. As a result, the measurements tend to underestimate the amplitude of the local perturbation $\varepsilon_{app}^i < \frac{dv}{v}(x)$.

To measure the temporal change from the scattered coda waves, two techniques are most widely adopted: the frequency-domain doublet technique (also referred to as moving window cross spectral technique, MWCS) (Poupinet et al., 1984), and the time-domain stretching technique (Lobkis & Weaver, 2003).

6.2.1 Doublet or moving window cross spectral (MWCS) technique

Poupinet et al. (1984) developed a method to measure velocity changes in the crust from the coda of repetitive earthquakes that have highly similar waveforms. These repetitive earthquakes are commonly referred to as *doublets* or *multiplets*. Hence the name, doublet technique. The technique is

alternatively referred to as moving window cross spectral technique (MWCS) and has been widely used for monitoring velocity changes (Brenguier, Campillo, et al., 2008; Brenguier, Shapiro, et al., 2008; Ratdomopurbo & Poupinet, 1995; Schaff & Beroza, 2004).

The idea of the seismic doublet technique is to measure a time-shift δt_i between a reference signal φ_{Ref} that corresponds to the initial state, and a current signal φ_{Curr} that has encountered a global velocity change in the medium (Fig. 13A). The time-shift is measured in short time windows—that should of course not be shorter than the longest period—centered around various lapse times t_i (Fig. 13B). The relative time-shift $\delta t/t$ is then estimated by a linear regression passing through zero (Fig. 13D). $\delta v/v$ can be obtained according to Eq. (14).

In the time domain, the time delay between the windows may be measured as the peak in correlation between the two signals, but it is generally more precise to measure the delay in the frequency domain. To measure δt in the frequency domain, the windowed segments are Fourier transformed,

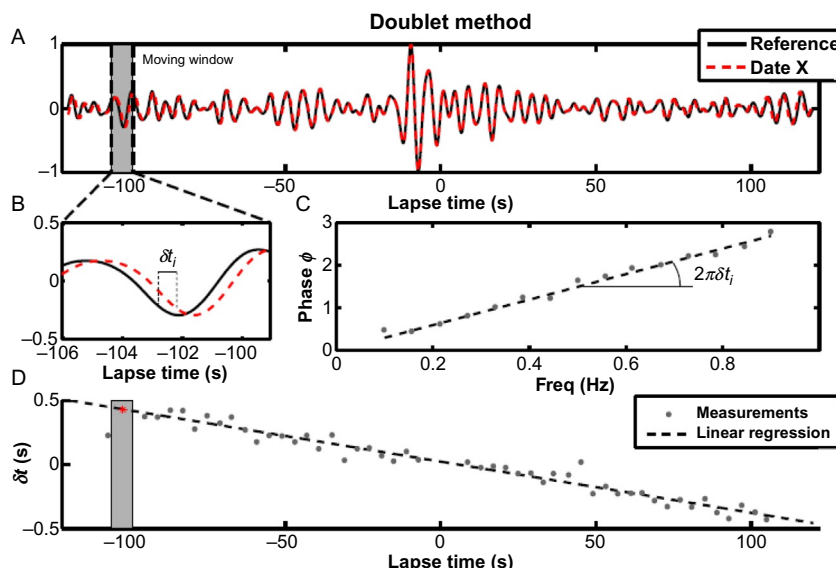


Fig. 13 Illustration of the doublet technique. (A) Reference signal φ_{Ref} (black) and time delayed signal φ_{Curr} (red). (B) Zoom into the windowed cross-correlations functions, marked with the shaded gray area in Fig. 13A. (C) The phase of the cross-spectrum of the windowed cross-correlations. The slope is equal to $2\pi\delta t$. (D) Estimation of $\delta t/t$ via linear regression of the delay measurements in all time windows. Courtesy Hadzioannou, C. (2011). *Ondes sismiques en milieu complexe: Mesure des variations temporelles des vitesses* (Unpublished doctoral dissertation). Université de Grenoble.

and the cross-spectrum $X(f)$ between the two Fourier transformed windowed time series (\mathcal{F}_{Ref} and $\mathcal{F}_{\text{Curr}}$) is calculated as follows:

$$X(f) = \mathcal{F}_{\text{Ref}}(f)\mathcal{F}_{\text{Curr}}^*(f), \quad (15)$$

where the asterisk denotes the complex conjugation and f is the frequency. The complex cross-spectrum can also be represented by its amplitude $|X(f)|$ and phase $\phi(f)$:

$$X(f) = |X(f)|e^{i\phi(f)}. \quad (16)$$

Assuming that the time-shift is constant in each processing window, ϕ is linearly proportional to the frequency f :

$$\phi(f) = 2\pi\delta t_i f. \quad (17)$$

From a linear regression δt_i can be estimated (Fig. 13C). The error can be determined as the squared misfit of the data to the modelled slope. Clarke, Zaccarelli, Shapiro, and Brenguier (2011) refined the analysis and incorporated a weight during the regression, which depends on the cross-coherence at each sampled frequency and that is assigned to each cross-phase value.

6.2.2 Stretching technique

An alternative method to quantify the temporal evolution of the seismic velocity is the stretching technique (Lobkis & Weaver, 2003; Sens-Schönfelder & Wegler, 2006). Here, too, the assumption is that a small global velocity change introduces a relative time-shift between φ_{Curr} and φ_{Ref} which is proportional to the travel-time. The current waveform φ_{Curr} is dilated—positively (stretched) or negatively (compressed)—in time by a factor $t \rightarrow t(1 \pm \varepsilon)$, following an decrease or increase in the medium velocity, respectively. Then, the dilated waveform is correlated with the reference waveform in the time domain:

$$CC(\varepsilon) = \frac{\int_{t_1}^{t_2} \varphi_{\text{Curr}}[t(1 - \varepsilon)]\varphi_{\text{Ref}}[t]dt}{\sqrt{\int_{t_1}^{t_2} \varphi_{\text{Curr}}^2[t(1 - \varepsilon)]dt \int_{t_1}^{t_2} \varphi_{\text{Ref}}^2[t]dt}}, \quad (18)$$

where t_1 and t_2 are the beginning and the end of the time window used. The value of ε , that maximizes the cross-correlation coefficient CC between φ_{Curr} and φ_{Ref} corresponds to the relative velocity change in the medium $\varepsilon = \frac{dv}{v}$ (Fig. 14).

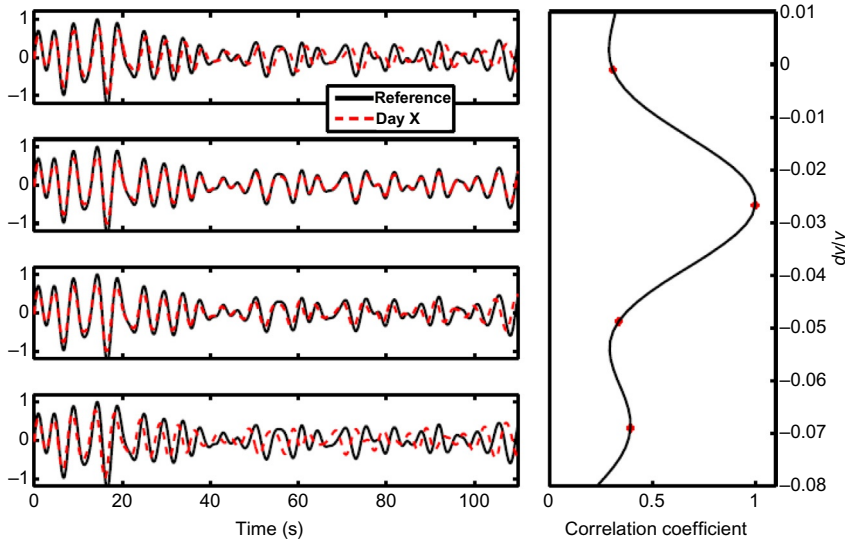


Fig. 14 Stretching method. *Left:* the red signal has been stretched for different values of ϵ . *Right:* the calculated correlation coefficient between the stretched and the reference trace (black) for the different values of ϵ . Courtesy Hadzioannou, C. (2011). *Ondes sismiques en milieu complexe: Mesure des variations temporelles des vitesses* (*Unpublished doctoral dissertation*). Université de Grenoble.

6.2.3 Advantages and disadvantages of the two methods

The two techniques are applied to the coda waveforms of the Green's function estimate that are reconstructed from the ambient field using cross-correlation. The data preprocessing and correlation techniques are the same as in the imaging contexts (Section 3). That is, those data processing steps that have been typically applied to obtain high-SNR correlation functions for ballistic wave reconstruction (Bensen et al., 2007) are also used to obtain good quality noise correlations for monitoring. However, filtering algorithms that target the removal of incoherent noise in the coda waveforms can significantly improve the quality of the relative travel-time change or phase-shift measurements and thus boost the temporal resolution and the overall information gain (Baig, Campillo, & Brenguier, 2009; Hadzioannou, Larose, Baig, Roux, & Campillo, 2011; Moreau, Stehly, Boué, Lu, & Campillo, 2017; Stehly, Cupillard, & Romanowicz, 2011).

Hadzioannou et al. (2009) compared the two techniques quantitatively on a controlled laboratory data-set. They concluded that a strong point of the doublet technique is that it does not suffer from amplitude changes of the waveform and manages clock errors in the origin time without further processing. The processing is also very fast.

The main advantage of the stretching technique reported in that study is its superior stability in the presence of residual noise in the correlations and its increased sensitivity to detect weak changes. This is offset by the less favorable properties of being computationally slower—a best-fitting ϵ is typically found in a simple grid search—and the often only approximately applicable assumption of a linear distortion of the test waveform that underlies this technique.

An empirical, albeit more cumbersome approach, is to compare the results obtained with each method to identify robust signals, and to understand possible discrepancies by analyzing auxiliary wavefield markers (energy, flux direction, partitioning) that can be used as proxies or indicators of the ambient field properties (Hillers et al., 2019). Through such direct comparison Hillers, Retailleau, et al. (2015), Hillers, Ben-Zion, Campillo, and Zigone (2015), and Hillers, Husen, Obermann, Planès, et al. (2015) found that the MWCS method generally yielded more stable and higher-SNR results. The lower performance of the stretching technique is typically attributed to the method's higher sensitivity to changes in the noise amplitude spectrum (Zhan, Tsai, & Clayton, 2013). Using numerical tests, Mikesell, Malcolm, Yang, and Haney (2015) compared the two methods to a third “Dynamic Time Warping” (DTW) approach and also found that in low SNR environments this DTW and the MWCS method outperform the stretching technique. In summary, the applied technique often remains a method of personal choice and convenience.

An essential advantage the stretching technique is that it measures not only the distortion of the waveform but also the residual waveform coherence, or similarity, associated with the optimal dilation. This independent physical parameter yields information about structural changes that affect trajectories. The stretching technique also allows for improved monitoring of localized changes. Instead of analyzing a long coda segment, shorter time windows can be used that should be, again, at least two periods long. For localized changes, the advantage of studying the evolution of time-shifts in the coda, i.e., a deviation from the linear trend, becomes apparent when considering again Fig. 12. With increasing lapse-time in the coda, the size of the diffusive halo, and hence the penetration depth of coda waves, evolves. Note that many coda-interferometry monitoring studies refer to the time in the coda as “coda lapse-time” often using the symbol τ . “Lapse-time dependence” then refers to solutions obtained in different coda windows.

Estimates on the depth of the change can help to constrain its origin. This information can be obtained when studying the evolution of the temporal

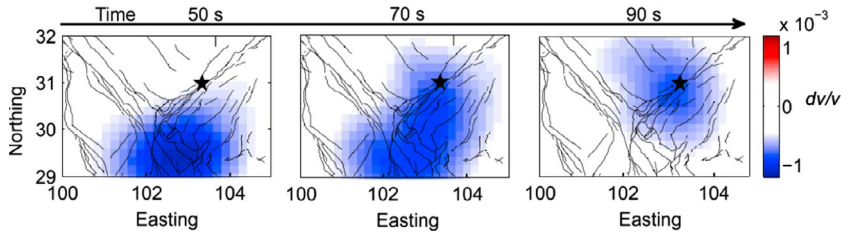


Fig. 15 Spatial distribution of velocity changes in the region around the 2008, $M_w7.9$ Wenchuan earthquake obtained from data at different lapse times in the coda. Modified after Obermann, A., Froment, B., Campillo, M., Larose, E., Planès, T., Valette, B., ... Liu, Q. Y. (2014). Seismic noise correlations to image structural and mechanical changes associated with the $Mw 7.9$ 2008 Wenchuan earthquake. *Journal of Geophysical Research*, 119(4), 3155–3168. 10.1002/2013JB010932.

changes with time in the coda (Obermann et al., 2014; Obermann, Planès, Larose, Sens-Schönfelder, & Campillo, 2013). This is illustrated in Fig. 15, where the spatial distribution of velocity changes in the region of the 2008, $M_w7.9$ Wenchuan earthquake (hypocenter marked with a star) is shown at different lapse times (Obermann et al., 2014). At early times in the coda (50 s), a velocity drop is observed in the Sichuan basin, whereas the sensitivity shifts toward the earthquake location at later times (70 s and 90 s). For the period band used in this study (12–20 s), at early times, the coda is dominated by scattered surface waves that have their highest sensitivity down to around 20 km. The velocity drop is interpreted as loading due to the heavy monsoon rains in this region that mainly affect the upper crust. At later lapse times the significant contribution of body waves in the coda (Obermann, Planès, Larose, Sens-Schönfelder, & Campillo, 2013) allows for sampling of much deeper regions. The velocity drop that is observed at these times is distinct at the earthquake location, indicating that the earthquake caused a significant change of the mechanical parameters at depth.

An inherent part of the procedure involving either technique is the definition of the reference function that ideally is a proxy of the unperturbed medium state. The stack length of the reference, and the choice of the time period, can have an effect on the obtained relative velocity change time series (Sens-Schönfelder, Pomponi, & Peltier, 2014). Brenguier et al. (2014) proposed a modification of the reference stack approach, where the velocity change time series are found as a best-fitting model to all the relative velocity change measurements between all possible combinations of correlation functions along the time axis. Note that in addition to the quadratic scaling of the number of available interstation pairs, the quadratic

scaling of time sample pairs can challenge the computational resources needed to find that best-fitting model. These individual estimates can be obtained with the MWCS or the stretching technique using the above described procedures. The final dv/v time series that yields a neutral average over the analysis period, is obtained with a standard linear least-squares scheme (Brenguier et al., 2014; Gómez-García et al., 2018; Tarantola & Valette, 1982). A tuning parameter is the characteristic length scale that controls the correlation of an obtained dv/v datum with neighboring estimates, leading to a variable temporal resolution of the velocity change time series (Brenguier et al., 2014; Gómez-García et al., 2018; Sanchez-Pastor et al., 2019). In this inversion approach the stationary wavefield assumption can be relaxed. This method can therefore better constrain the dv/v model at times with low-quality cross-correlation functions that can result from wavefield variations.

6.3 Spatial location of CWI time-lapse changes

Estimating the spatial distribution of the changes using coda waves is not a straightforward problem, given the complexity of the multiply scattered wave paths. This is why coda waves measurements were initially limited to detection purposes only. Applying a geometrical regionalization procedure that simplifies the coda wave propagation with straight rays can yield a first-order spatial distribution of the changes, when working with sufficiently dense networks (Brenguier et al., 2014; Brenguier, Shapiro, et al., 2008; Chen, Froment, Liu, & Campillo, 2010; Duputel et al., 2009; Froment, Campillo, Chen, & Liu, 2013; Takagi, Okada, Nakahara, Umino, & Hasegawa, 2012).

Using a more physics-based approach, Pacheco and Snieder (2005) showed that the phase-shift of coda waves induced by a localized velocity change could be modelled using a “statistical” sensitivity kernel. This kernel describes the proportion of scattered wave energy that interacts, on average, with the velocity change. An example sensitivity kernel is shown in Fig. 16. Larose et al. (2010) and Rossetto et al. (2011) showed that a similar sensitivity kernel can describe the coda wave decoherence induced by a variation in the scattering properties which indicates a structural change. The similarities and differences between these kernels are described in Planès, Larose, Margerin, Rossetto, and Sens-Schönfelder (2014) and Margerin, Planès, Mayor, and Calvet (2016).

To compute the spatial distribution of the changes, a linear inverse problem can be solved (Tarantola & Valette, 1982). This was applied; to

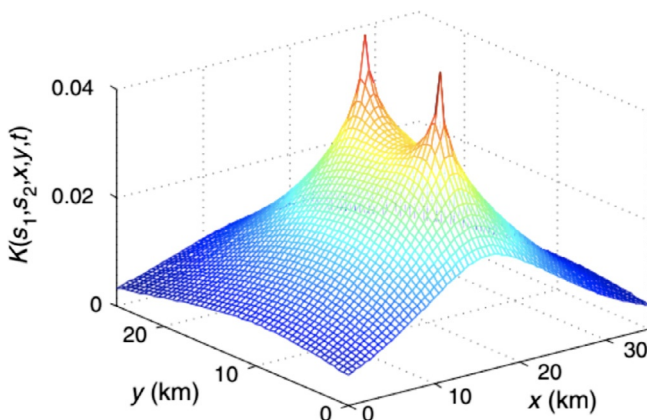


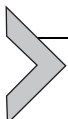
Fig. 16 Spatial representation of the sensitivity kernel that describes the statistical time spent in each area. The two peaks indicate the position of the station pair. The time statistically spent in a region decreases with increasing distance to the stations.

numerical simulations (Kanu & Snieder, 2015 b; Planès & Larose, 2013; Planès, Larose, Rossetto, & Margerin, 2015), locating precursors of volcanic eruptions (Lesage, Reyes-Dávila, & Arámbula-Mendoza, 2014; Obermann, Planès, Larose, & Campillo, 2013; Sanchez-Pastor et al., 2018), assessing fault zone damages (Froment, 2011; Obermann et al., 2014), subsurface changes due to high pressure fluid injections (Hillers, Husen, Obermann, Planès, et al., 2015; Obermann et al., 2015; Sanchez-Pastor et al., 2019), and crack/fissure growth in concrete blocks (Larose et al., 2015, 2010; Zhang et al., 2016). Some of these results will be illustrated in more detail in Section 7. In these applications, the coda waves are assumed to be composed of a single propagation mode; either surface waves or body waves. This assumption allows the use of analytical expressions of the multiply scattered intensity propagator. Therefore, either a 2-D sensitivity kernel describing the 2-D surface wave intensity propagation, or a 3-D sensitivity kernel describing the 3-D body wave intensity propagation is used. However, coda waves are composed of different propagation modes, namely, P, S and surfaces waves, in proportions that depend on the degree of heterogeneity, coda lapse-time, source mechanism, etc. (Hennino et al., 2001; Margerin et al., 1999; Obermann, Planès, Larose, & Campillo, 2013; Perton, Sánchez-Sesma, Rodríguez-Castellanos, Campillo, & Weaver, 2009).

Building sensitivity kernels that describe the full complexity of the coda wave composition is challenging since the elastic radiative transfer equation does not have an analytical solution even for the half space. An alternative

method has been proposed by [Kanu and Snieder \(2015 a\)](#) based on 2-D numerical simulations of acoustic wavefields in heterogeneous media. This approach consists of computing the intensity propagator through an ensemble average of the envelope of the coda wavefield obtained in different realizations of the disorder. This approach has the strong advantage of intrinsically taking into account all of the complexity of the wavefield (mode conversions, inhomogeneous velocity or scattering, topography, etc.). However, the computational cost of the 2-D acoustic simulations is high and the convergence to a stable solution is slow. The approach was recently extended to elastic wave propagation ([Snieder et al., 2019](#)), but has yet to be extended to 3-D.

[Obermann, Planès, Hadzioannou, and Campillo \(2016\)](#) showed that a linear combination of the 2-D surface wave and 3-D body wave kernels is a good description of the sensitivity of the multiply scattered waves as a function of depth and lapse-time in the coda. The downside however, is that this method can, at present, only describe the subsurface with uniform velocity and heterogeneity. [Obermann, Planès, Larose, and Campillo \(2018\)](#) applied this combined kernel to image crustal changes from the 2008 M7.9 Wenchuan earthquake at depth.



7. Applications across scales

Turning noise recordings into useful seismic signals through correlation techniques constitutes a breakthrough concept in a variety of scientific domains; ranging from seismology to acoustic and medical imaging. The wavefield excitation mechanisms are as diverse as the applications. In this section, we attempt to provide a comprehensive overview of the various fields that use diffuse waves to monitor changes in a wide range of materials, including the human body and the Earth's subsurface.

At present, the most prominently emerging fields are at diverging ends of the length scale: nondestructive material testing (mm to m scale) and regional scale (tens to hundreds of km) seismological applications, used to monitor volcanoes or crustal damage and recovery after moderate-size and large earthquakes. In addition, some applications have involved civil and geotechnical structures, including buildings ([Ebrahimian, Rahmani, & Todorovska, 2014](#); [Nakata & Snieder, 2014](#); [Nakata et al., 2013](#); [Snieder, 2006](#)), dams, levees, and underground mines. Landslide and glacial monitoring ([Mainsant et al., 2012](#); [Mordret, Mikesell, Harig, Lipovsky, & Prieto, 2016](#); [Renalier, Jongmans, Campillo, & Bard, 2010](#)) also showed robust

results using time-lapse interferometry. Inspired by the results in seismology and nondestructive testing, seismic interferometry has found its way into passive elastography, which can be interpreted as seismology of the human body. Noise-based monitoring may also be of major interest for industrial applications in the future. However, so far few studies have been undertaken in this context; a promising example is the monitoring of the stress state of geothermal reservoirs (Hillers, Husen, Obermann, Planès, et al., 2015; Obermann et al., 2015; Sanchez-Pastor et al., 2019).

7.1 Nondestructive material testing using diffuse ultrasound

Time-lapse measurements using ultrasound (US) in concrete have been widely adopted in the nondestructive testing community. In pulse-echo configurations, the velocity of ultrasound yields information on the mechanical properties of the material (Anderson & Nerenst, 1952; Komlos, Popovics, Nürnbergová, Babal, & Popovics, 1996), such as its rigidity and state of stress (Lillamand, Chaix, Ploix, & Garnier, 2010), level of chemical (Naffa, Goueygou, Piwakowski, & Buyle-Bodin, 2002) or mechanical damage (Berthaud, 1991). It is also possible to visualize major discontinuities associated with a significant impedance contrast in the concrete, including large cracks, cavities and large pieces of steel, etc.

With US techniques, a better spatial resolution is obtained by increasing the frequency. However, attenuation also increases considerably with frequency, to the extent that the effective range for US inspection is limited (Popovics & Rose, 1994), especially in applications where direct waves are considered. Attenuation relates to two distinct physical phenomena: scattering and intrinsic absorption. In the first case, the information contained in the ultrasonic pulse response is transformed into a complex collection of late waveforms. In the latter it dissipates before it can be recorded. Typically, frequencies between 100 kHz and 5 MHz show multiple scattering, but not yet strong absorption and are used for CWI in concrete (Planès & Larose, 2013). However, the transition from one regime to another is smooth and depends largely on the constitution of the concrete mix. For more details on the different propagation regimes in concrete we refer to Planès and Larose (2013). Despite a long history of nondestructive material testing, the application of CWI in this field is relatively recent. The simplest physical effect that results in a relative velocity change is probably temperature. Larose et al. (2006) acquired acoustic coda waves in a concrete structure at different times of the day, and measured the thermally induced

ultrasonic velocity changes. They confirmed this effect to be in general reversible, and they quantified the concrete relative velocity change to be of the order of $1.6 \times 10^{-3} \text{ K}^{-1}$. This effect was quantitatively confirmed by [Wunderlich and Niederleithinger \(2013\)](#). However, in most cases, temperature variations are considered as having the potential to corrupt CWI measurements. [Zhang et al. \(2013\)](#) proposed using two separate samples: one for the mechanical test and the other as a reference, both being subjected to the same environmental change. Up to now, this thermal bias control procedure is certainly the most reliable way of eliminating environmental effects on CWI.

Applications of CWI to monitor stress changes were studied next. In most cases, the rigidity of the material increases with increasing strain (or stress), which means that the higher the deformation (or stress), the faster the acoustic waves. In 2005, [Michaels and Michaels \(2005\)](#) published the first application of CWI to nondestructive testing. They investigated the effect of both external temperature variations and the damage in an aluminum specimen, in terms of relative velocity change and remnant correlation coefficient (coherence) to discriminate between the overall change induced by temperature variations and the local change induced by a defect. [Grêt, Snieder, and Scales \(2006\)](#) exploited US coda waves to monitor time-varying rock properties in a laboratory environment. They studied velocity changes related to Berea sandstone exposed to uni-axial stress; in granite and aluminum samples exposed to temperature fluctuations, and in sandstone with increased water saturation ([Fig. 17](#)).

[Larose and Hall \(2009\)](#) demonstrated that when the stretching technique is applied to CWI, it can be used to recover the relative velocity change with a precision of 10^{-5} , a level of sensitivity that enables stress change monitoring in concrete with load increments as small as 50 kPa. This is far below the stress levels that might otherwise irreversibly damage the material ([Planès & Larose, 2013](#)).

Going from the laboratory to a larger scale, [Zhang et al. \(2011\)](#) tested CWI on a concrete rail-track prototype. As the real-size concrete sample was subjected to successive loadings, mimicking damage and aging due to traffic (high speed train), the authors demonstrated that the nonlinear elastic constant (the slope of the relative velocity change versus stress during test sequences) increased with load cycles, offering the first demonstration of concrete damage using CWI. [Liu, Bundur, Zhu, and Ferron \(2016\)](#) investigated the efficiency of biomineralization on the self-healing of internal microcracks in cement-based mortar samples. CWI was used

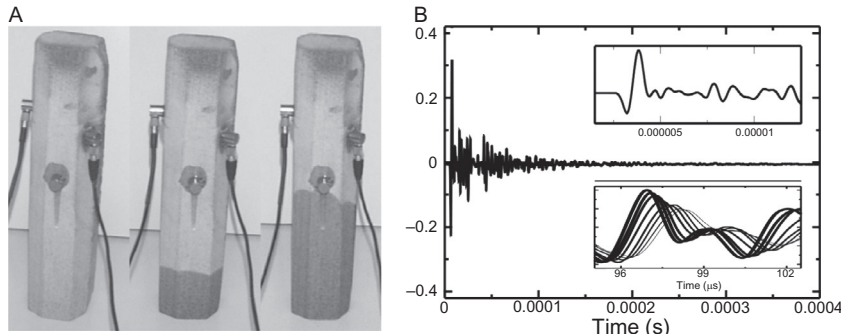


Fig. 17 (A) Berea sandstone sample as the fluid is infiltrating. Ultrasonic source and receiver are glued to the rock. (B) Waveforms recorded in the Berea sandstone block for eight different levels of water saturation. The *insets* show details of the waveforms (*top*) around the first arrival and (*bottom*) in the late coda. The fastest (thickest line) is measured on the dry sandstone, and the slowest (thinnest line) is measured at a water front height of 7 cm. In addition to the velocity change, the amplitudes decrease with increased water content in the sample. The dominant frequency is 0.33 MHz. Modified after Grêt, A., Snieder, R., & Scales, J. (2006). Time-lapse monitoring of rock properties with coda wave interferometry. *Journal of Geophysical Research: Solid Earth*, 111(B3), B03305.

to continuously monitor the repair process (500 kHz pulser source). The samples with active bacteria showed a significantly large change in velocity over time, which the authors attributed to the progressive healing process. Compressive stress tests on samples with and without biomineralization confirmed this interpretation. Other articles report on a wide variety of CWI loading experiments (Masera, Bocca, & Grazzini, 2011; Schurr, Kim, Sabra, & Jacobs, 2011; Shokouhi, Zoëga, & Wiggenhauser, 2010; Zhang et al., 2013) and observe different acousto-elastic coefficients related to the damage state of the concrete. As acousto-elasticity depends on the constitution of the cement formulation, values may vary from one sample to another. However, healthy concrete samples generally show an acousto-elastic constant of the order of 0.1×10^{-3} to 2×10^{-3} MPa $^{-1}$. Acousto-elastic values of damaged concrete are significantly higher; ranging from 2×10^{-3} to 6×10^{-3} MPa $^{-1}$. Note that even higher values are expected for more intense damage.

Some authors estimated the spatial distribution of the medium damage from the spatial and temporal distributions of lapse-time changes measured in the US data. Larose et al. (2010) used the probabilistic sensitivity kernels described in Section 6.3 to locate damage (drilled holes) occurring in a concrete block. Of course, existing technique such as US tomography can already provide a 2-D or 3-D distribution of US velocities, and velocity

changes. There are nevertheless several differences between tomographic techniques and coda-related techniques. Since the US energy propagates more slowly in the diffusive regime than in the ballistic regime used for tomography, the resolution with coda wave techniques is less attractive. Nevertheless, two characteristics support the use of diffuse waves. First, the tiny changes detected by diffuse waves could not be detected by direct waves (tomography), which means that the sensitivity is several orders of magnitude greater with coda waves. Second, tomography requires dense arrays of sources and receivers with a spatial pitch governed by the wavelength, whereas diffuse wave techniques (such as CWI) require much sparser source-receiver arrays with a spatial pitch controlled by the scattering mean free path. These two advantages facilitate on-site applications.

Using inversion with probabilistic sensitivity kernels, [Niederleithinger, Sens-Schönfelder, Grothe, and Wiggenhauser \(2014\)](#) localized compressional load effects in a concrete specimen over various loading cycles ([Fig. 18](#)). [Larose et al. \(2015\)](#) detected and imaged the fracture length evolution in a concrete m-size bloc. [Zhang et al. \(2016\)](#) worked with a 15-ton reinforced concrete beam subjected to a four-point bending test, causing cracking. Using CWI and the probabilistic sensitivity kernels, they detected and located the cracking zones in the core of the concrete beam at an early stage by mapping the changes in the concrete's microstructure; and could monitor the internal stress level in both temporal and spatial domains by mapping the variation in velocity caused by the acousto-elastic effect.

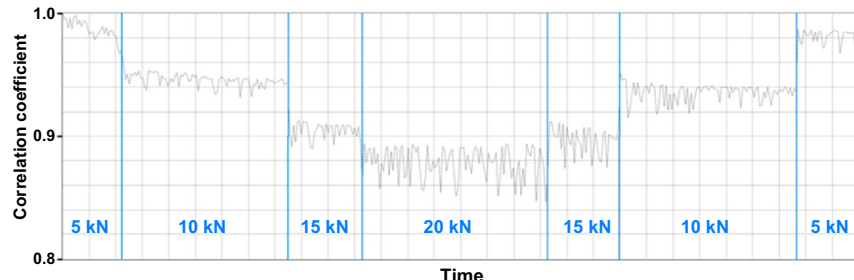
The properties of the diffuse US field allowed the authors to monitor such a massive structure using only 20 transducers, in an acquisition procedure that lasted only a few minutes.

7.2 Passive elastography: Seismology of the human body using shear waves from muscle activities

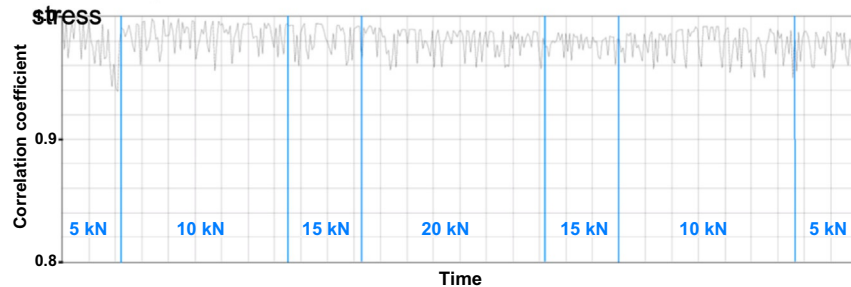
Medical imaging is applied to the soft tissue of living organisms instead of hard rock. Living tissue naturally vibrates due to muscles activities, heart beat, and pulsating arteries. These natural tissue vibrations are often considered as disturbing noise, reducing the quality of classical imaging techniques. We introduce the imaging method here—which can also be extended to time-lapse diagnostics—to highlight the applicability of the wave physics principles in very different propagation regimes.

The idea then, as in seismology, is to take advantage of these shear waves that are naturally present to construct shear elasticity (shear-wave

A Sensor pair close to the induced stress



B Sensor pair at distance to the induced stress



C Coda wave tomography for 20 kN load

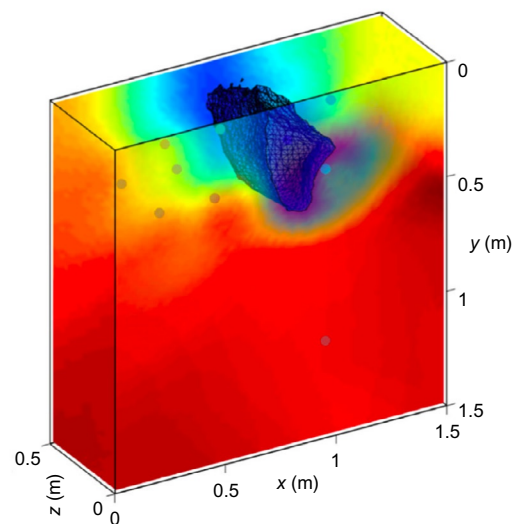


Fig. 18 (A) Correlation coefficient change under load for a sensor pair close to the induced stress. (B) At distance to the induced stress. (C) Probabilistic coda-wave tomography for 20 kN load. The color code indicates the change probability (red: low, blue: high). Modified after Niederleithinger, E., Sens-Schönfelder, C., Grothe, S., & Wiggenhauser, H. (2014). Coda wave interferometry used to localize compressional load effects in a concrete specimen. In EWSHM-7th European workshop on structural health monitoring.

tomography) maps of individual organs. Ultrafast ultrasound scanners that can reach thousands of frames per second (Bercoff, Tanter, & Fink, 2004; Nightingale, Soo, Nightingale, & Trahey, 2002; Sandrin, Catheline, Tanter, Hennequin, & Fink, 1999) are used to measure or reconstruct the noisy speckle pattern, the analogy to the seismic noise recordings. This approach is referred to as passive elastography or seismology of the human body, since no shear-wave sources are used. This passive approach has the potential to mature into an alternative for elastography of deep organs or regions that are challenging to assess; where the high-power ultrasound sources needed for sufficient radiation pressure are difficult to apply. Another advantage is that the method is fully compatible with low-frequency acquisition systems, such as standard two-dimensional and three-dimensional ultrasound and magnetic resonance devices. Sabra, Conti, Roux, and Kuperman (2007) applied correlation techniques to surface waves of a human quadriceps muscle and measured its global viscoelastic properties. Catheline, Benech, Brum, and Negreira (2008) showed that time reversal of elastic waves can be observed inside a soft solid. Inspired by seismic noise correlation and time reversal, Gallot et al. (2011) conducted the first passive elastography experiment—i.e., a shear-wave tomography of soft tissues—in an *in vivo* liver. No longer depending on controlled shear-wave sources, they used low-speed shear waves that are constantly excited by breathing and cardiac processes as a source for the Green's function retrieval. An ultrasonic device in the megahertz frequency band can record the motion of the ultrasonic speckle at a rate of 1000 frames per second. This ultrafast imaging is needed to measure shear-wave propagation in the human body, where the typical frequencies range from 10 to 200 Hz. Fig. 19 shows the tomographic image (sonogram) of the liver region. The interface between the abdominal muscles and the liver is visible around $z = 12$ mm. The passive shear-wave-speed tomography from the correlation width clearly indicates the two regions. The averaged shear-speed estimations agree with the values in the literature.

Zorgani et al. (2015) performed a passive magnetic resonance elastography (MRE) of the brain. They extracted information related to the mechanical properties of the soft brain tissue from hundreds of snapshots of randomly fluctuating shear-wavefields. In the brain, the natural motion is caused by pulsating arteries and cerebrospinal fluid exchange. The total time of an *in vivo* experiment is 11 min, and from this, three components of the displacements can be acquired. Fig. 20 shows the reconstructed shear-wave images.

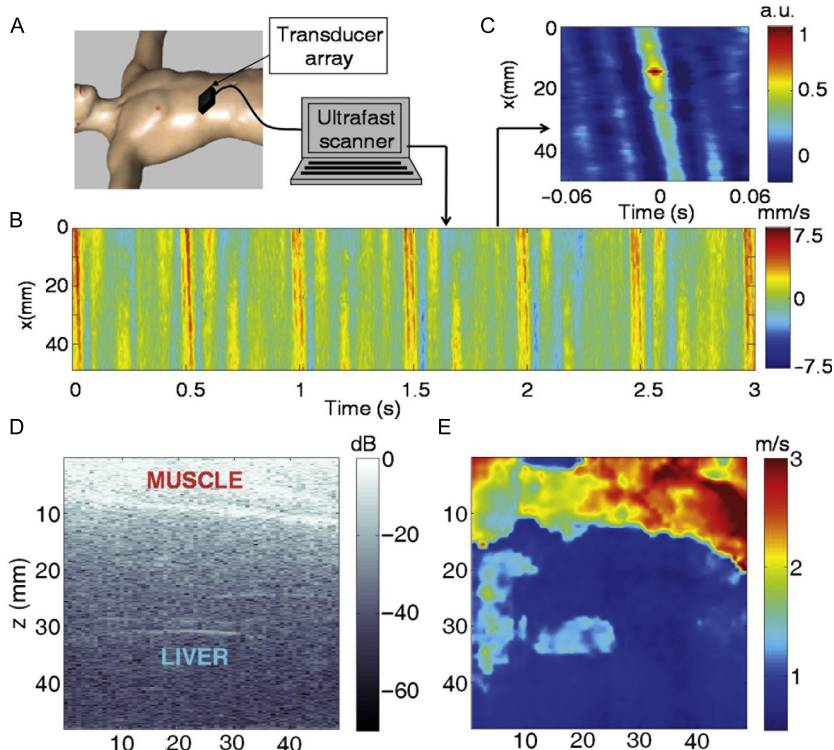


Fig. 19 (A) Experimental setup for the *in vivo* correlation-based tomography: an ultrafast scanner was used to measure the natural displacement field in the liver region. (B) The particle velocity along an acquisition line at 4 cm, and parallel to the array, shows the physiological elastic field. (C) In the correlation map $C(x_0, x_t)$ with $x_0 = 14$ mm, only one direction of propagation emerged from the refocusing field. (D) Sonogram of the liver region. The interface between the abdominal muscles and the liver is visible around $z = 12$ mm. (E) The passive shear-wave-speed tomography from the correlation width clearly shows the two regions. The averaged shear-speed estimations are in agreement with the values in the literature. *Modified from Gallot, T., Catheline, S., Roux, P., Brum, J., Benech, N., & Negreira, C. (2011). Passive elastography: Shear-wave tomography from physiological noise correlation in soft tissues. IEEE Transactions on Ultrasonics, Ferroelectrics, and Frequency Control, 58(6), 1122–1126.*

These *in vivo* experiments demonstrate the pertinence of applying the tools of seismology in the field of medical imaging. Passive elastography can provide benefits for medical applications, whereby the determination of local tissue elasticity can support and improve diagnostic confidence. [Catheline \(2017\)](#) points out that the elasticity maps can be decisive for early cancer detection.

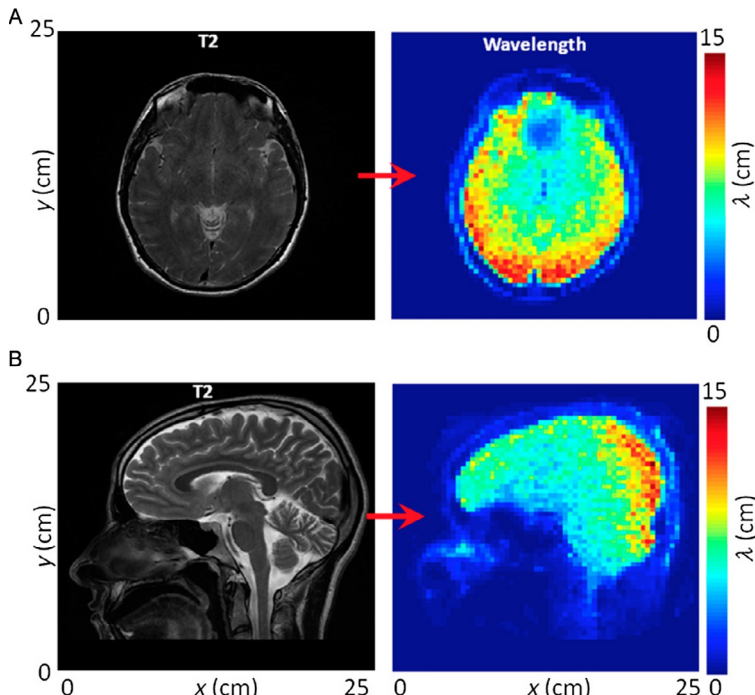


Fig. 20 In vivo brain passive MRE. (A) Axial view and (B) sagittal view of (left) the T2-weighted image and (right) its corresponding shear-wavelength tomography. From Zorgani, A., Souchon, R., Dinh, A.-H., Chapelon, J.-Y., Ménager, J.-M., Lounis, S., ... Catheline, S. (2015). Brain palpation from physiological vibrations using MRI. *Proceedings of the National Academy of Sciences*, 112(42), 12917–12921.

7.3 Monitoring applications on the local scale (meter–kilometer) using anthropogenic and oceanic noise

7.3.1 Monitoring bridges and buildings using traffic noise, earthquakes, and ambient vibrations

Following nondestructive testing approaches Stähler, Sens-Schönfelder, and Niederleithinger (2011) applied the CWI method to an engineering structure, i.e., a concrete bridge under construction. The applied procedure is referred to as “Incremental Launch method” (Leonhardt & Baur, 1971), where the girder is pushed horizontally across pillars. During the launching process, the concrete frame of the bridge thus undergoes severe stress fluctuations between 0.5 and 14 MPa. This should result in measurable velocity variations of approximately 1.5%. As a source, Stähler et al. (2011) dropped a hammer on to an aluminum plate directly coupled to the concrete structure.

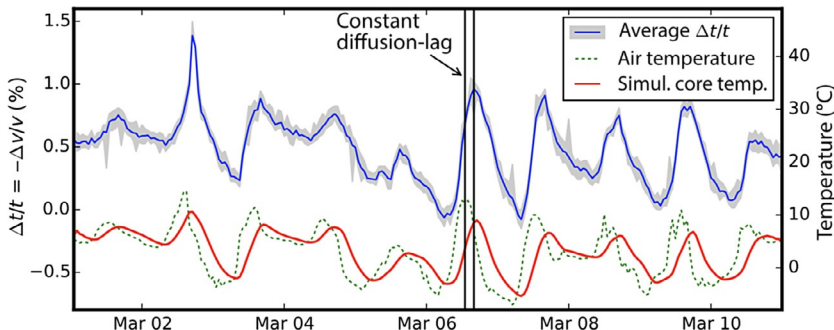


Fig. 21 Relative velocity variations of the first days of March, averaged over 32 receiver pairs, where only velocity variations corresponding to CCs ≥ 0.85 are considered. The shaded area indicates the standard deviation of the velocity variation curve. The air temperature is shown with a dotted line, while the vertical lines show the constant thermal diffusion lag of about 3 h. This shift also fits the simulated core temperature (solid line), assuming a slab-width of 36 cm. From Salvermoser, J., Hadzioannou, C., & Stähler, S. (2015). Structural monitoring of a highway bridge using passive noise recordings from street traffic. *The Journal of Acoustical Society of America*, 138(6), 3864–3872.

With this procedure, they could excite a broad frequency spectrum reaching beyond 4 kHz that was recorded by an array of geophones. To relate observed changes in the elastic wave velocity to the stress changes associated with the load of the frame on the bridge pillars, [Stähler et al. \(2011\)](#) measured the stress–velocity relationship in laboratory experiments with samples of the bridge’s concrete. Using this relationship, their data fit the stress model that was obtained by engineers very well ([Fig. 21](#)). [Salvermoser, Hadzioannou, and Stähler \(2015\)](#) repeated a similar experiment on a highway bridge using cross-correlations of traffic noise as a source of excitation. Over a period of 2 months, they continuously recorded traffic noise on 32 receiver pairs and found a remarkable agreement with core temperature fluctuations on the bridge. The velocity changes ranged from -1.5% to 2.1% , corresponding to temperatures ranging from -23°C to 14°C . The authors showed that they can establish a transfer function that is almost flat and (theoretically) consists only of temperature independent velocity variations. The experiments demonstrate that stress changes can be measured with elastic waves not only in the controlled environment of a laboratory but also in the field, at engineering structures. The temporal resolution is high (≤ 1 h) and the method continuously applicable with minimal logistical effort and at a relatively low cost. One drawback is the limited spatial resolution related to the relatively low frequencies and the late-coda evaluation.

In a different type of application Snieder (2006), Picozzi et al. (2011), Nakata et al. (2013), and Nakata and Snieder (2014) monitored buildings using deconvolution interferometry. For monitoring the structural health of a building, the response of the building to an earthquake needs to be separated from the imprint of soil-structure coupling and from wave propagation below the base of the building. This separation cannot be performed by cross-correlation interferometry. Cross-coherence interferometry produces unphysical wavefields propagating at slower velocity than the true wave speed of the real building, and the attenuation of the waveforms obtained from cross-coherence do not correspond to the travel distance of the waves. Snieder (2006) studied data recorded at the Millikan Library in Pasadena, California, during the 2002 Yorba Linda earthquake and showed that seismic interferometry based on deconvolution, where the wavefields recorded at different floors are deconvolved with waves recorded at a target receiver inside the building, is a technique to extract this building response and thus estimate the velocity of the wave that propagates inside the building. The target receiver behaves as a virtual source, and what is retrieved, is the response of a short building that is cut off at the virtual source. Because this cutoff building is independent from the structure below the virtual source, the technique can be useful for estimating local structure and local damage. Deconvolution interferometry also allows us to estimate the damping factor of the building.

Picozzi et al. (2011) and Nakata et al. (2013) applied deconvolution interferometry to earthquake data from the L'Aquila sequence in Italy and earthquakes in Japan, respectively, to monitor the state of health of the exposed buildings. Nakata and Snieder (2014) tested the method with ambient vibrations instead of earthquakes as source signals. Nakata and Snieder (2014) found that the velocities estimated from ambient vibrations were more stable than those computed from earthquake data. Because the acceleration of the observed earthquake records varies depending on the strength of the earthquakes and the distance from the hypocenter, the velocities estimated from earthquake data vary because of the nonlinear response of the building. On the other hand, from ambient vibrations, they were able to extract the wave velocity due to the linear response of the building. An additional plus for temporal monitoring is the time continuity of ambient vibrations. Nakata and Beroza (2015) found that the seismic velocity in a building in Tokyo decreased about 20% after the 2011 Tohoku earthquake, 400 km away, and only partially recovered over a period of 16 months. This reduction was interpreted as a weakening of the building due to the earthquake ground motion. Natural frequencies and seismic wave velocities of

buildings and other civil structures do not only change in response to strong earthquake shaking, but also due to thermal fluctuations or material aging effects. When earthquake waves are weak and induce only small strains, the structure's natural frequency decreases due to the shaking and bending, but recovers quickly in the aftermath. When earthquakes are large, strong ground motion can introduce permanent changes—damage—to the structure. Nakata and Kashima (2018) studied these effects of strong motion and aging using more than 1600 earthquake waveforms observed in a building in Tsukuba, Japan, across 20 years. The natural frequency and seismic velocities in the building have been decreased over the 20 years (Fig. 22). They were able to separate the components caused by strong earthquake ground motion and by general aging.

7.3.2 Monitoring earthen dams, levees and landslides using localized noise sources

In the USA alone, about 160,000 km of earth levees and 85,000 dams provide flood protection, produce renewable energy for millions of people, store and protect the water supply and provide recreation and areas of natural protection (American Society of Civil Engineers (ASCE), 2013). This number is significantly larger worldwide. A particularly high-severity risk arises from the massive tailing dams, built to contain often toxic waste slurry remaining after processing ore at open-pit and underground mines. These dams are often built in developing countries, with loose regulations and a

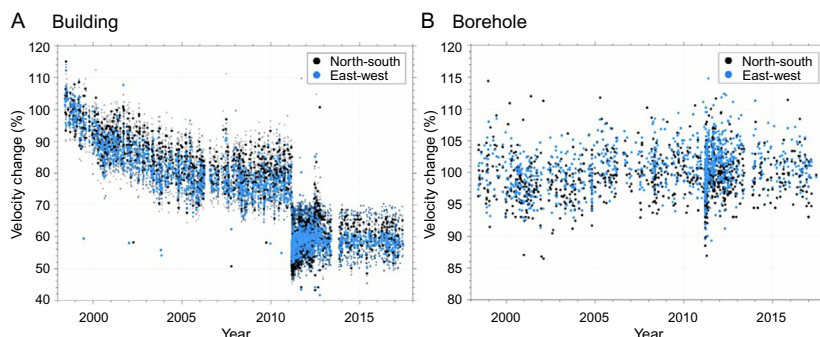


Fig. 22 (A) Averaged velocity changes over all floors in the building in two different components. The 100% velocity is defined as the averaged velocity in 1998. The abrupt change in velocity is caused by the 2011 Tohoku earthquake. (B) Similar to panel (A), but at a borehole at a distance of 20 m. From Nakata, N., & Kashima, T. (2018). Time-lapse changes in seismic response of building over 20 years due to earthquakes and aging. In Eleventh U.S. National Conference on Earthquake Engineering.

preference for cost-saving building methods. The most common tailings dam design is called the upstream method. In this method, the tailings next to the dam wall are allowed to dry, and these solidified tailings are then used as the foundation for subsequent raises to accommodate more tailings. While this wall-design method is very attractive from an economic stand-point, as it requires the least amount of earth moving to increase the dam capacity, it is particularly susceptible to soil liquefaction due to shaking from earthquakes, mine blasts, or other vibrations (MacGregor, Fell, Stapledon, Bell, & Foster, 2014; Martin & McRoberts, 1999) and one of the most likely to fail (Breitenbach, 2010). Over the last decades, several catastrophic tailings dam failures have occurred, causing significant damage to the environment and high loss of life (World Information Service of Energy (WISE)).

The latest catastrophic failure occurred on January 25, 2019, when the tailing dam of an iron mine failed in Belo Horizonte, Brazil, releasing 12 Mio m³ of contaminated slurry and causing more than 300 fatalities. It is estimated that approximately two to five major tailing dam failures occur per year (Davies, 2002), making this failure rate more than 100 times higher than the rate of normal water-storage dams (Azam & Li, 2010). Earth dams and levees are prone to failure in the form of internal erosion of soils which can lead to a runaway failure mechanism (Van Beek, De Bruijn, Knoeff, Bezuijen, & Förster, 2010).

Monitoring levees and dams is time-consuming and labor intensive, resulting in infrequent monitoring of most areas, often only when a specific concern is raised. An additional problem is that internal erosion is often invisible to current methods of inspection until it manifests itself at the exterior surface, which is often too late for an early warning (Fell, Wan, Cyganiewicz, & Foster, 2003). Radars and/or high-resolution cameras are used to monitor small deformations of the dam walls. Unfortunately, these methods measure surface perturbations and are not capable of detecting internal changes in the walls. To mitigate these catastrophic events in the future, there is an urgent need to develop noninvasive, cost-effective methods to monitor the structural stability of these structures over time. In pioneering studies, Planès et al. (2016) and Olivier, Brenguier, de Wit, and Lynch (2017) investigated the potential of seismic interferometric methods to detect internal changes in dams.

Planès et al. (2016) monitored induced failure processes on (a laboratory and) the field-scale embankment structure *Ijdijk*, a calibration levee, a structure that is typical for the Netherlands. During the experiment, the upstream reservoir was filled with water in stages to simulate realistic hydraulic loading

events. Twenty-four vertical component geophones were deployed along three lines on the downstream face of the dam, continuously recording noise during the experiment. To construct stable virtual sources, Planès et al. (2016) used water splashing from an outlet pipe into a drainage canal as a localized source. Most of the signal energy is contained in frequencies from 5 to 100 Hz. For such high frequencies, it becomes essential to use a selection filter (Olivier et al., 2015) to avoid periods with strong anthropogenic activity. Throughout the experiment, Planès et al. (2016) observed temporal variations in seismic wave velocities that reflect variations of elastic moduli and density of the material, themselves related to variations of effective stress and porosity during the loading stages. Some of them could be related to local pore water pressure responses. The *Ijdijk* embankment loaded to partial failure revealed a 30% reduction in averaged surface wave velocity. These responses are consistent with the strong influence of effective stress on surface wave velocity.

Olivier et al. (2017) investigated the applicability of ambient seismic noise techniques to detect internal changes in a tailings dam wall in Tasmania, Australia, during a period of heavy rainfall. The energy source they used for the virtual source reconstruction was similar to Planès et al. (2016): water flowing from a decant system and wind waves on the adjacent reservoir lake. The observed relative velocity variations were sensitive enough to measure and locate increases in the fluid saturation of the soil due to rain. Olivier et al. (2017) also detected subsurface changes in the dam wall in locations consistent with observations of increased seepage between the contact of local topography and the earthen dam wall. In both studies, seismic velocity changes were driven by fluid saturation, changes in ground water level, increased loading from increased dam water level and sudden increases in fluid pore pressure in a section of the dam wall. These results suggest that seismic interferometry can provide a valuable, relatively inexpensive tool to remotely monitor the structural stability of dams and levees over time.

Similar to the failure mechanisms of dams and levees, increases in pore pressure in clay-rich unstable mountain flanks might cause partial or complete liquefaction and lead to rapid mass movements that pose critical problems for risk management worldwide. This solid-to-liquid transition results in a dramatic reduction of mechanical rigidity in the liquefied zones. Mainsant et al. (2012) studied a landslide-prone area in the Swiss Alps and detected rapid decreases in shear-wave velocity several days prior to a landslide of a few thousand m³ that was triggered in 2010 after a rainy period. They used ambient noise in the frequency range 4–25 Hz. The main sources

with constant location in this frequency band are wind in the trees and traffic along a road at the base of the landslide. More studies are needed, but the results show the potential of the method to detect rigidity variations before failure and give early warning prior to catastrophic landslides—if the areas are identified and instrumented.

7.3.3 Monitoring underground mines using active sources and mining noise

Active underground mines are interesting environments that are typically well instrumented and naturally fit between laboratory and crustal scale. Currently, most mines with seismic monitoring networks only use a small fraction of the recorded vibrations, in the form of microseismic events, whereas all other data are discarded. Though CWI in a mining environment is not widely applied, the following two applications suggest that this method can potentially be used for the monitoring of deformation and stress changes in the vicinity of excavations, which is of essential importance for hazard management and mitigation. Depending on the type of energy source, the demands for the seismic equipment can be kept modest.

[Grêt, Snieder, and Özbay \(2006\)](#) carried out a controlled stress-change experiment in a mine pillar with a preinstalled pressure cell at the experimental hard rock mine Edgar Mine in Idaho Springs, CO. They used a hammer source and collected data on a distant geophone. With CWI, they could monitor the in situ stress change as a change in seismic velocity. The data processing they used is basic and can easily be built in a simple, stand-alone instrument.

[Olivier et al. \(2015\)](#) used a passive source approach for CWI in the Boliden's Garpenberg mine in Sweden. As the wavelength of surface waves is too large to provide sufficient sensitivity and resolution for small-scale industrial environments, such as mines, mining activity was used as a noise source (20–240 Hz). With the extracted hourly stable estimates of the Green's function, they measured the immediate and long-term effects of a sudden dynamic stress perturbation on the surrounding rock, which occurred during and after an excavation blast. The blast was accompanied by a significant drop in seismic velocity, which is interpreted as a consequence of damage and plastic deformation. These nonelastic effects are healed by the confining stresses over a period of 5 days until the seismic velocity converges to a new baseline level. The change in the baseline level of the seismic velocity, before and after the blast ([Fig. 23](#)), is indicative of a change in the static stress that is comparable to the results of elastic static stress modeling.

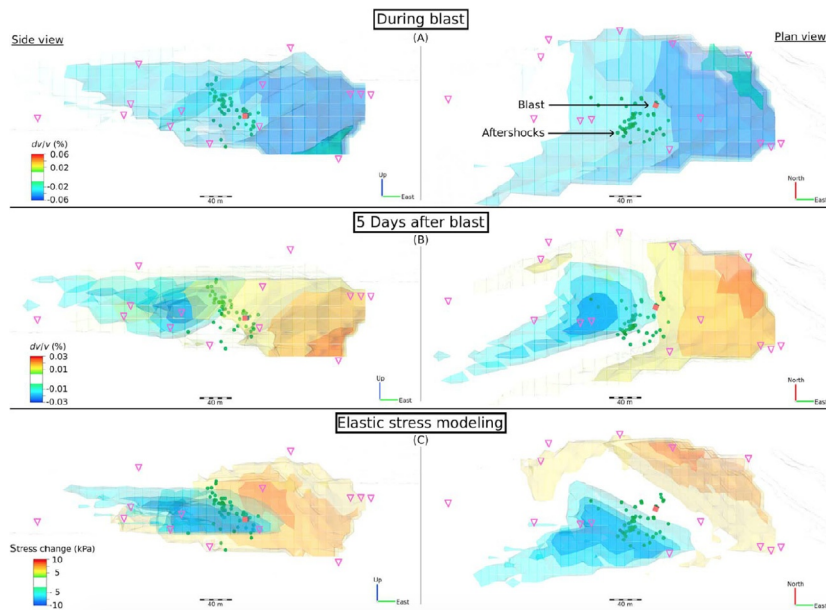


Fig. 23 Comparison of iso-surfaces, of the immediate change in the seismic velocity, the permanent change in the seismic velocity and the modeled volumetric stress change. The permanent change in the seismic velocity (5 days after blast) and the modeled static stress change are qualitatively in agreement for most locations. From Olivier, G., Brenguier, F., Campillo, M., Roux, P., Shapiro, N. M., & Lynch, R. (2015). Investigation of coseismic and postseismic processes using *in situ* measurements of seismic velocity variations in an underground mine. *Geophysical Research Letters*, 42(21), 9261–9269.

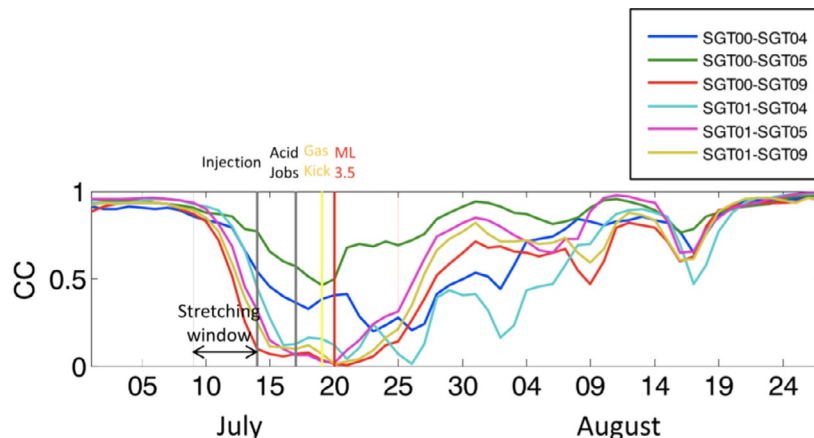
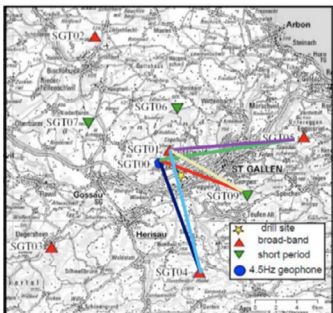
7.3.4 Monitoring reservoirs using the ambient seismic field

Time-lapse imaging is of great importance to monitor the state of a reservoir that is exploited or prone to be exploited. In the petroleum industry and for large-scale off-shore CO₂ projects, such as the Sleipner field in Norway, the method of choice is 4-D reflection seismics (Arts et al., 2002; Chadwick et al., 2010). In the geothermal context and also for small-scale CO₂ projects, this method is not an option due to the high costs and logistic demands. Around the geothermal sites of Soultz-sous-forêt and Rittershoffen in France, noise-directivity analyses and ambient noise tomographies were carried out to retrieve shear-wave velocity models of the upper crust around the reservoirs (Calò, Kinnaert, & Dorbath, 2013; Lehurjeur, Vergne, Maggi, & Schmittbuhl, 2017a, 2017b; Lehurjeur, Vergne, Schmittbuhl, & Maggi, 2015; Lehurjeur et al., 2018). A noise-tomography has also been performed as a first-order exploration for geothermal potential in the Geneva basin

(Planès, Obermann, Atunes, & Lupi, 2019). In this context, the additional contribution of a dispersive surface wave tomography to a reflection survey, is the method's sensitivity to temperature or porosity anomalies. One of the key problems for most potential geothermal sites is that insufficient information is available on the in situ pattern of faults, and on their response to past and present hydrothermal fluid flow. There is therefore a substantial lack of knowledge on the origin of induced seismicity, its link to large-scale fault structures and the relationship between flux of meteoric water and active deformation. Over the last decade, induced seismicity has become an important topic of discussion, especially owing to the concern that industrial activities could cause damaging earthquakes. The problem of induced seismicity is particularly important for the future development of geothermal energy in Europe, as deep geothermal energy exploitation projects such as Basel (2006) and St. Gallen (2013) have been aborted due to the induced earthquakes they created (M_{L} 3.5, M_{L} 3.4, respectively) and an increasing risk aversion of the general population. On 15 November 2017, a M_{L} 5.4 was induced at a geothermal site in Pohang, South Korea, injuring 82 people and causing significant economic damage. In South Korea, the alarming dilemma is that detailed previous site characterizations had not indicated the presence of a fault (active or not).

In these situations seismic interferometry can potentially provide complementary observations about aseismic deformation and therefore of the changing stress state in the subsurface. Obermann et al. (2015) monitored time-lapse changes at the geothermal site of St. Gallen, Switzerland, with noise-cross-correlations. The hydrothermal project in St. Gallen targeted preexisting faults at a depth of 4.5 km. To gain a better understanding of the reservoir, over 4 days, small-scale (100–200 m³) water and acid injectivity tests were performed. The seismicity associated with these tests (roughly 40 events) did not exceed magnitude M_{L} 0.2 and was judged to be well within the expected range. One day after the last injection, gas unexpectedly entered the borehole and operators had to react to prevent a blow-out. The well-control operations in the form of heavy mud injections, lead to a M_{L} 3.5 (Diehl et al., 2014). Obermann et al. (2015) observed a significant loss of waveform coherence in the seismic coda that started with the injections of water and acid into the well (Fig. 24). The perturbation can be horizontally and vertically constrained to the injection site. The waveform decoherence was interpreted as likely being caused by changes in attenuation and/or reflectivity due to the gas. This aseismic response of the subsurface to geo-mechanical well operations yielded additional information on the reservoir dynamics, which could have warned operators, if performed in real-time (Fig. 24).

A



B

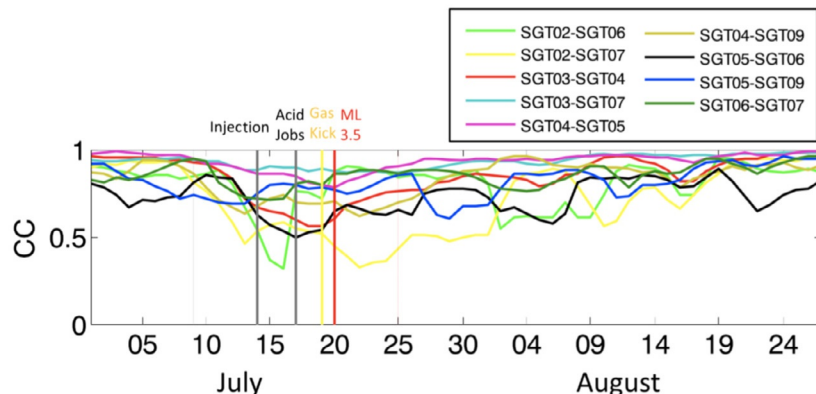
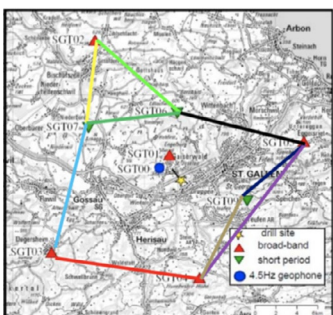


Fig. 24 Monitoring time-lapse changes associated with the deep geothermal project in St. Gallen. Shown is the waveform coherence (CC) for the indicated station pairs: (A) close to the injections and (B) further away from the injections. The vertical lines in the CC plots mark the injection tests, the gas kick and the ML3.5 earthquake. The strong aseismic reservoir response to the injections can be clearly observed. Modified from Obermann, A., Kraft, T., Larose, E., & Wiemer, S. (2015). Potential of ambient seismic noise techniques to monitor the St. Gallen geothermal site (Switzerland). *Journal of Geophysical Research*, 120(6), 4301–4316. 10.1002/2014JB011817.

Hillers, Husen, Obermann, Planès, et al. (2015) studied continuous data records around the 2006 Basel enhanced geothermal project (Häring, Schanz, Ladner, & Dyer, 2008). They detected and located an aseismic transient deformation in response to the hydraulic stimulation of the crystalline basement at a depth of 5 km that was accompanied by more than 10,500 earthquakes in the first 6 days (Dyer, Schanz, Spillmann, Ladner, & Häring, 2010). The obtained velocity change and decorrelation signals indicate a deformation pattern in the overlying sedimentary rocks that appears to be migrating upward. Peak deformation occurred well after the largest M3.5 event, and after the induced seismicity had ceased. Irrespective of the controversial results, the study highlights the possibility to obtain complementary observables during seismically quiet times, i.e., at times when standard microseismicity-based reservoir characterization tools are not available.

Nayak, Brenguier, Manga, et al. (2018) characterized the reservoir responses to earthquakes and fluid extraction at the Salton Sea geothermal field, California. They found that the field experienced a number of sudden velocity reductions (0.035–0.25%) that are likely caused by openings of fractures due to dynamic stress transients (as small as 0.08 MPa and up to 0.45 MPa) from local and regional earthquakes. Depths of velocity changes are estimated at around 0.5–1.5 km, similar to the depths of the injection and production wells. Sanchez-Pastor et al. (2019) monitored responses of the Reykjanes Geothermal System, a high-temperature system on the Reykjanes peninsula in Iceland, to production and stimulation operations. This study was particularly challenging, as the system has been exploited for decades and injection and production are occurring in parallel in several wells. They could distinguish fluctuations associated with injection and production rate drops. Additionally, they observed a slow velocity decrease of 0.4%/year in the area surrounding the power plant, which coincides with subsidence in this region, measured by Keiding, Árnadóttir, Jonsson, Decriem, and Hooper (2010). While all of these studies applied SI posteriori to the well operations, the outcomes made it clear that noise-based SI should be applied in real-time to help detect aseismic deformation processes which might lead to unexpectedly large earthquakes, or unexpected reservoir behavior.

In the petroleum context, we are only aware of time-lapse studies across the Vallhal oilfield, an oil field in the Norwegian sector of the central North Sea. De Ridder and Biondi (2013) and Mordret et al. (2014) performed 4-D noise-based tomographies of Scholte waves (i.e., waves traveling along the interface of a water layer and the sediment layers) that they retrieved

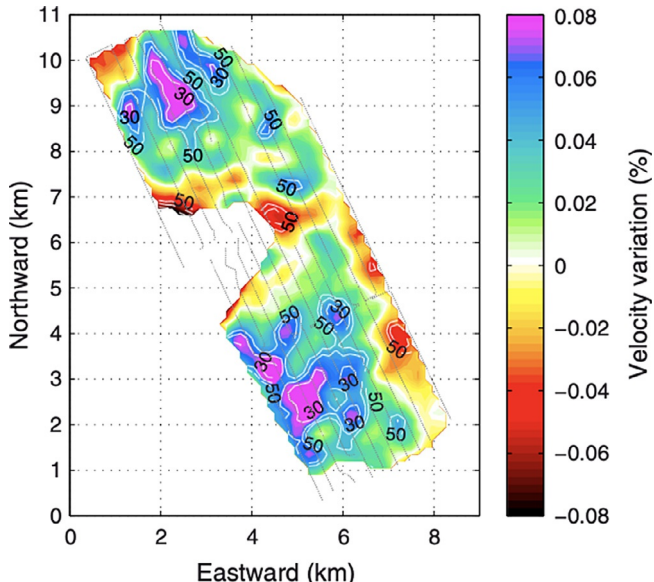


Fig. 25 Relative velocity variations across the Valhall oilfield. Only the time-lapse measurements with interstation distances longer than 0.33 km and pairs of 2004–2005 CCs with correlation coefficients of the direct arrival window higher than 0.9 are used. The contours show the relative errors from 30% to 50% with 10% steps. Areas with errors less than 50% are considered reliable. From Mordret, A., Shapiro, N. M., & Singh, S. (2014). Seismic noise-based time-lapse monitoring of the valhall overburden. *Geophysical Research Letters*, 41(14), 4945–4952.

from cross-correlation of ambient noise at relatively high frequencies (0.55–1.75 Hz, 0.4–1.6 Hz, respectively), in different years. Consequently, the required recording length for stable correlation functions could be reduced to short 6.5 h. Mordret et al. (2014) showed a large patch of increased seismic velocity in the southern part of the oil field and a weaker anomaly in the northern part (Fig. 25). The southern increase of velocity can be attributed to the exploitation of the southern flank of the Valhall reservoir with new wells. When the exploitation started on the southern flank, a new small subsidence bowl started to form on the edge of the older one, which closed the former cracks and tended to increase the seismic velocity. The same time-lapse pattern is found in P-to-S converted wave time-shift and shear-wave splitting delay measurements (Zwartjes, Wills, De Maag, & Hatchell, 2008). Most likely, the northern patch of increased velocity is also related to the subsidence. The results correlate well with 4-D active seismic surveys (De Ridder, 2014; Hatchell, Wills, & Didraga, 2009; Wills, Hatchell, & Bourne, 2008).

7.4 Passive monitoring at the regional scale using the ambient seismic field

7.4.1 Environmental effects

When working with seismic stations deployed at, or close to, the Earth's surface, environmental changes, such as temperature or rainfall and the subsequent pore pressure variations, become relevant and are often superimposed on other signals. This environmental perturbation often has a pronounced seasonal component and is a nuisance for many studies since it masks the signals of interest. [Rivet, Brenguier, and Cappa \(2015\)](#) estimated a transfer function to link fluid pressure and seismic velocity changes at Piton de la Fournaise volcano, La Réunion, France and obtained a "cleaned," flat velocity variation curve. The drawback of this method is that such a transfer function is very location specific and only possible to estimate from long-term data recordings of several years. Other studies, made these environmental influences their principal research target and investigated various aspects that are known to influence shallow seismic wave speeds: seasonal changes from precipitation ([Meier, Shapiro, & Brenguier, 2010](#); [Obermann et al., 2014](#); [Sens-Schönfelder & Wegler, 2006](#); [Tsai, 2011](#); [Wang et al., 2017](#)), temperature changes ([Hillers, Husen, Obermann, Planès, et al., 2015](#); [Meier et al., 2010](#); [Tsai, 2011](#)), freeze–thaw cycles ([Gassenmeier, Sens-Schönfelder, Delatre, & Korn, 2015](#); [James, Knox, Abbott, & Screamton, 2017](#)), long-term variations from climatic forcing ([Lecocq, Longuevergne, Pedersen, Brenguier, & Stammmer, 2017](#)), and snow loading/melting ([Mordret et al., 2016](#)). Most of these processes induce pore pressure changes or strain in the crust that can be measured in terms of seismic velocity changes. [Clements and Denolle \(2018\)](#) reproduced the groundwater level changes in the San Gabriel Valley, California, that are marked by multiyear depletions and rapid recharges, typical of California's cycles of droughts and floods (Fig. 26). Their results are

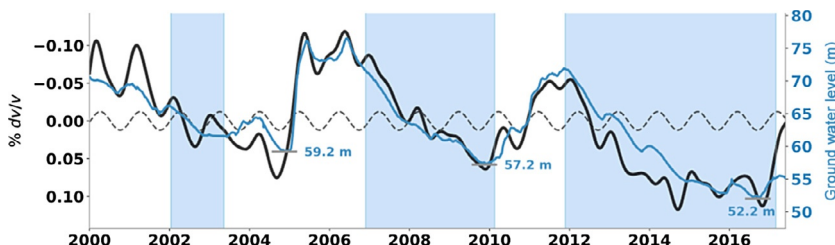


Fig. 26 Time-lapse changes in seismic wave speed related to ground water levels in the San Gabriel Valley, California. Gray bars indicate lowest historical water levels of the Baldwin Park Key Well. Blue patches indicate times of drought. From [Clements, T., & Denolle, M. A. \(2018\). Tracking groundwater levels using the ambient seismic field. Geophysical Research Letters, 45\(13\), 6459–6465.](#)

compatible with the predicted volume of water lost in the San Gabriel Valley during the 2012–2016 drought and thus provided a new, complementary approach to monitor groundwater storage at a regional scale.

7.4.2 Volcano monitoring

Accurate volcanic hazard monitoring is an important step to mitigate the associated risk at local and regional scales. At many volcanoes, standard equipment to deliver near-real-time observables includes GPS, tiltmeters, gas monitoring, cameras, and seismometers. While most of these methods are limited to surface observations, the analysis of seismic data provides a look at the processes occurring in the volcano interior. A standard tool is the study of the presence, quantity, and migration of microseismicity, which can yield important information about forthcoming and ongoing eruptions (Armbuster, Kim, & Rubin, 2014; Peng & Rubin, 2016; Roman, 2017). The ongoing deformations in the subsurface due to the movement of pressurized volcanic fluids alter the elastic and scattering properties of the surrounding medium. In some cases, but rarely, such variations can be detected by classical local-earthquake tomography, as during the March 2009 eruption of Redoubt Volcano, where the presence of a mobile phase at shallow depth beneath the volcano was linked to a reduction in S-wave velocity (Kasatkina, Koulakov, West, & Izbekov, 2014). However, the variations in seismic velocity associated with the transport of magma toward the surface (stress changes of a few kPa) are often too small (<0.1%) to be detected by tomography techniques (Brenguier et al., 2016). Here, CWI emerged as a complementary tool to gain information regarding the volcanic unrest. Brenguier, Shapiro, et al. (2008) first showed that velocity variations obtained from seismic noise cross-correlations correspond with the inflation state of the volcano and that significant velocity drops can be associated with imminent eruptions; observations that have been corroborated in follow-up studies (Fig. 27) (Olivier, Brenguier, Carey, & Donaldson, 2019). Brenguier, Shapiro, et al. (2008) found precursory signals at around two weeks prior to volcanic eruptions at Piton de La Fournaise. This volcano in La Réunion, France is certainly the best studied from a seismic noise imaging point of view (Brenguier et al., 2016; Clarke et al., 2011; Duputel et al., 2009; Mordret, Rivet, Landès, & Shapiro, 2015; Obermann, Planès, Larose, & Campillo, 2013; Rivet, Brenguier, Clarke, Shapiro, & Peltier, 2014; Sens-Schönfelder et al., 2014).

Over the past decade, temporal changes of seismic velocity were studied at other volcanoes around the globe using auto- or cross-correlation of

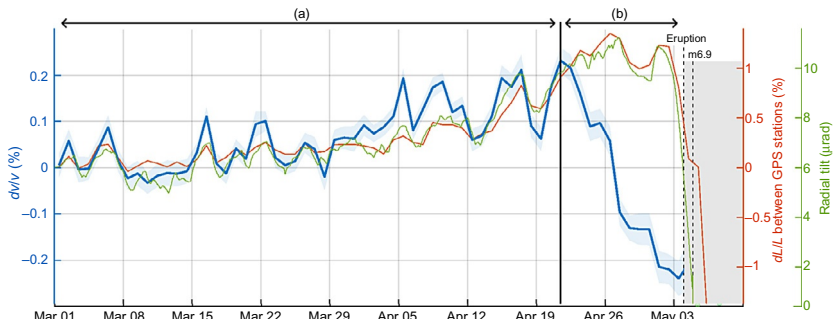


Fig. 27 Average relative daily velocity changes (blue) at Kilauea volcano prior to the 2018 eruption. The velocity changes are well correlated with relative distance (GPS measurements, green) and radial tilt change (red) up to the 20th of April, after which there is rapid decrease in velocity due to secondary processes, while the inflation is still being registered by the GPS and tilt stations. From Olivier, G., Brenguier, F., Carey, R., & Donaldson, C. (2019). Decrease in seismic velocity observed prior to the 2018 eruption of Kilauea volcano with ambient seismic noise interferometry Geophysical Research Letters, AU2 46(7), 3734–3744.

ambient seismic noise: Mt. Etna, Italy (De Plaen et al., 2019); El Hierro, Spain (Sanchez-Pastor et al., 2018); Mt. Ruapehu, New Zealand (Mordret, Jolly, Duputel, & Fournier, 2010); Merapi volcano, Indonesia (Budi-Santoso & Lesage, 2016); Miyakejima volcano, Japan (Anggono, Nishimura, Sato, Ueda, & Ukawa, 2012); Klyuchevskoy volcano group, Kamchatka, Russia (Koulakov et al., 2013); Kilauea, USA (Donaldson, Caudron, Green, Thelen, & White, 2017; Olivier et al., 2019); Colima volcano, Mexico (Lesage et al., 2014). Grêt, Snieder, Aster, and Kyle (2005) also showed that other especially site specific energy sources can be used as a source for CWI measurements; such as Strombolian explosions of large gas bubbles in the lava lake of Mt. Erebus (Antarctica). Typically, the studies do not go beyond the observation of unrest. A more in-depth investigation of the underlying volcanic processes, and a spatial location of the changes, is often missing or not feasible due to the limited number of deployed stations.

Obermann, Planès, Larose, and Campillo (2013) showed that not only velocity changes are of interest in volcano monitoring but also the loss of waveform coherence. Waveform coherence is much more sensitive to very localized structural changes in the subsurface, such as local crack opening and closing that might not yet produce a measurable change in seismic velocity. Using probabilistic sensitivity kernels, Obermann, Planès, Larose, and Campillo (2013) located such precursory changes at Piton de la Fournaise in space (Fig. 28). The location of the potential eruption site is of particular

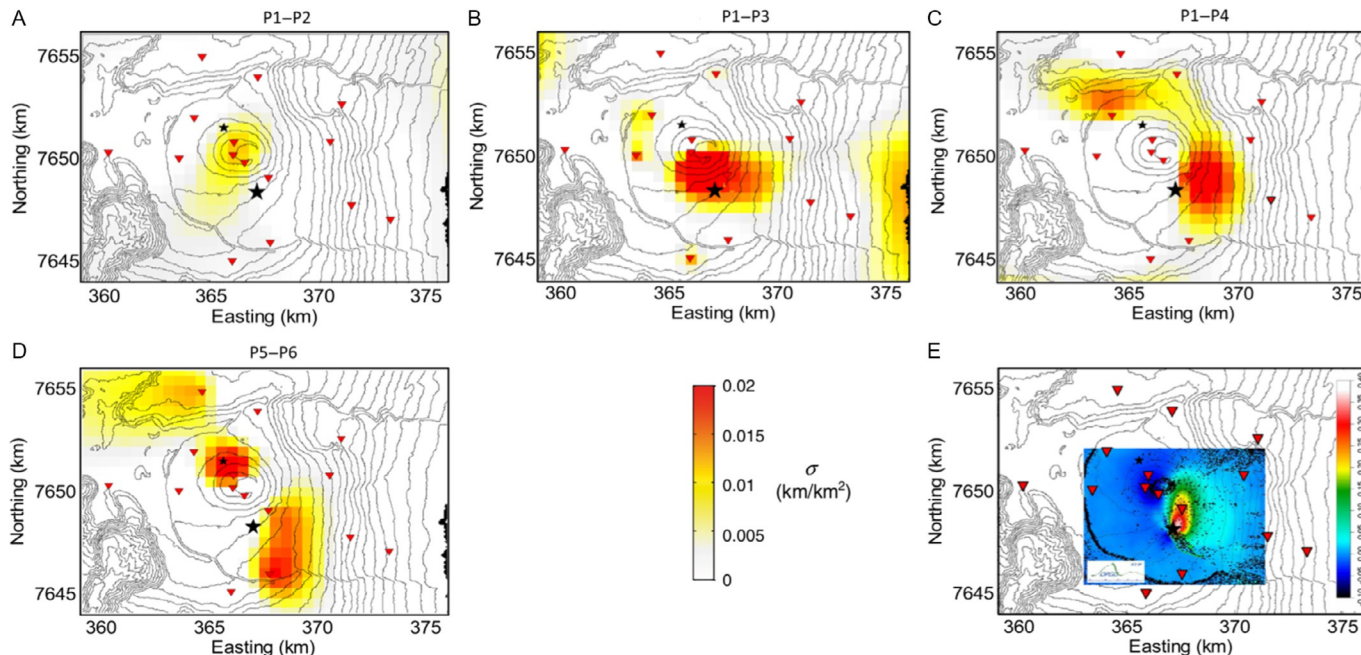


Fig. 28 Changes in waveform coherence at Piton de La Fournaise, prior to and during the 2010 eruptions, shown in the form of scattering cross section density maps. The eruption sites are marked with a star. (A) During the intrusion (September 2010). (B) Prior to the eruption (October 2010). (C) During the October eruption with precursory signal of the December eruption. (D) Changes caused by the December eruption. (E) InSAR-derived coeruptive displacements for the period from September to October 2010, displayed as the East-West component, in meters. Modified from Obermann, A., Planès, T., Larose, E., & Campillo, M. (2013). Imaging pre- and co-eruptive structural and mechanical changes on a volcano with ambient seismic noise. *Journal of Geophysical Research*, 118(12), 6285–6294.

importance for volcanoes that are prone to effusive flank eruption. In combination with other unrest indicators, the local population could receive a warning well ahead in time (typically 2 weeks at Piton de la Fournaise).

Studying the interior dynamics is also of particular importance for submarine volcanoes, where direct surface measurements are not available. [Sanchez-Pastor et al. \(2018\)](#) performed a study at El Hierro submarine volcano in the Canary Islands. An analysis of waveform coherence from phase auto and cross-correlations allowed them to clearly identify different preeruptive phases of this newly appearing volcano.

7.4.3 Monitoring earthquake responses and fault zone processes

CWI was first used with earthquake multiplets ([Peng & Ben-Zion, 2006](#); [Poupinet et al., 1984](#)) and repeated artificial sources ([Nishimura et al., 2000](#)) to infer changes in material properties in the form of a decrease in seismic velocity caused by the strong shaking of large nearby earthquakes. Because of the limiting factors associated with controlled sources and earthquakes, the temporal resolution of the monitored changes is poor and irregular. The introduction of CWI to “tectonic monitoring” came with the technique’s application to correlation functions obtained from the ambient seismic field. [Wegler and Sens-Schöpfeler \(2007\)](#) first applied CWI to autocorrelation functions obtained from ambient noise recordings in the vicinity of an earthquake. They used a single station in the source region of the M_w 6.6 Mid-Niigata earthquake, Japan, and could observe a coseismic drop in velocity of about -0.6% that was assumed to be caused by the stress decrease in the Earth’s crust during the earthquake. [Brenguier, Campillo, et al. \(2008\)](#) used a network along the San Andreas Fault near Parkfield, California, USA and observed coseismic velocity drops of around $0.02\text{--}0.08\%$ that coincided with the occurrence of the 2003, M_w 6.5 San Simeon and 2004, M_w 6.0 Parkfield earthquake. For both earthquakes, they could observe a postseismic relaxation ([Fig. 29](#)). The relaxation varied in time, from 8 months for the San Simeon event at 60 km distance, to about 3 years for the Parkfield event. This long-term recovery process was very similar to the relaxation curve associated with the along-fault displacement deduced from GPS measurements ([Freed, Ali, & Bürgmann, 2007](#); [Johanson, Fielding, Rolandone, & Bürgmann, 2006](#)). [Brenguier, Campillo, et al. \(2008\)](#) concluded that the evolution of the seismic velocity changes after the Parkfield earthquake was governed by postseismic stress relaxation within deeper parts of the fault zone and the surrounding region, as opposed to damage of shallow layers caused by the strong ground shaking in case of the San Simeon event.

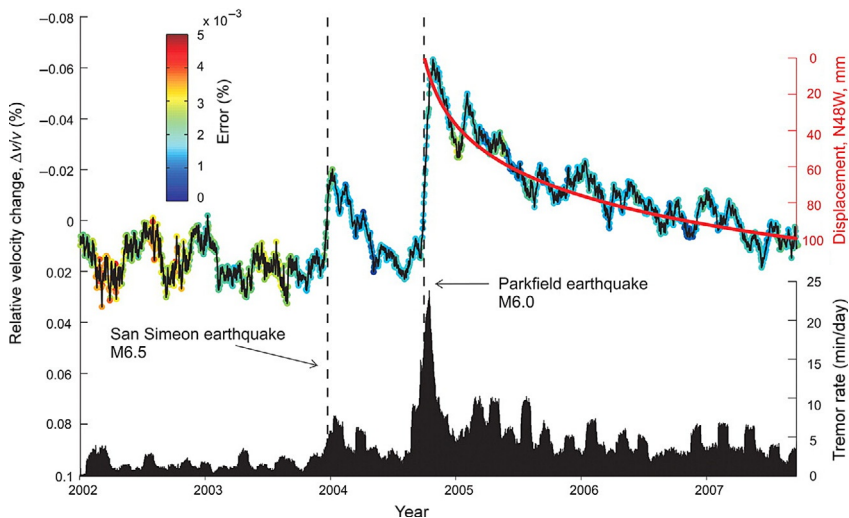


Fig. 29 Seismic velocity changes, surface displacements from GPS, and tremor activity near Parkfield. The red curve represents the postseismic fault-parallel displacements along the San Andreas fault, as measured by GPS. The tremor rates are averaged over a centered 30-day-length moving time window. From Brenguier, F., Campillo, M., Hadzioannou, C., Shapiro, N. M., Nadeau, R. M., & Larose, E. (2008). Postseismic relaxation along the San Andreas fault at Parkfield from continuous seismological observations. *Science*, 321, 1478–1481.

Since then, the technique has found applications in numerous regions of the world, in particular in California and Japan, where large earthquakes occur frequently and dense seismic networks are established; Chile (Richter, Sens-Schönfelder, Kind, & Asch, 2014); Italy (Soldati, Zaccarelli, Faenza, & Michelini, 2015); China (Chen et al., 2010; Froment et al., 2013; Obermann et al., 2014); Japan (Brenguier et al., 2014; Hobiger, Wegler, Shiomi, & Nakahara, 2012, 2016; Minato, Tsuji, Ohmi, & Matsuoka, 2012; Nakata & Snieder, 2011; Sawazaki, Sato, Nakahara, & Nishimura, 2009; Sawazaki & Snieder, 2013; Takagi et al., 2012; Wegler, Nakahara, Sens-Schönfelder, Korn, & Shiomi, 2009); California (Brenguier, Campillo, et al., 2008; Taira, Nayak, Brenguier, & Manga, 2018; Wu et al., 2016). We note the resolution of systematic medium changes in response to slow slip or deep creep events (Hillers et al., 2019; Rivet et al., 2011) that can yield important insights into fault mechanics, and triggering and earthquake interaction processes in tectonically active plate boundary regions. Note, however, that all of these case studies resolved the response of the medium adjacent to or surrounding the earthquake fault, not processes on the fault itself. Monitoring processes on

active faults or in the associated damage zones remains challenging because of their relatively tabular structure that is difficult to resolve using the diffusive halo. Monitoring the properties of fault zone trapped noise and reconstructed trapped modes (Hillers & Campillo, 2016; Hillers, Campillo, Ben-Zion, & Roux, 2014), however, may open a possibility of *in situ* fault zone probing, as well as attempts to reconstruct fault-penetrating direct waves.

To assess the effect of earthquakes on the crust at different depths, the correlations can be analyzed at different frequencies. Shallow changes observed at high frequencies (around 1–5 s) are interpreted as a consequence of near-surface damage during coseismic shaking and postseismic healing. Changes at greater depths, observed at lower frequencies (around 10–30 s), are interpreted as local changes in stress level. They typically show a coseismic drop and a time-varying postseismic recovery process. Hobiger et al. (2012) investigated velocity changes related to the 2008 M_w 6.9 Iwate-Miyagi Nairiku earthquake in Japan within three frequency ranges from 0.125 to 1.0 Hz, sensitive to different depth ranges. While most of the velocity changes are limited to the upper few hundred meters, at some locations, layers down to 2.5 km were affected by the earthquake. Froment et al. (2013) observed clear differences between shallow and deep crustal responses to the M_w 7.9, 2008 Wenchuan earthquake. Obermann et al. (2014) spatially mapped these velocity changes using probabilistic sensitivity kernels (Fig. 30) and could locate damage around the earthquake epicenter and along the rupture zone, limited to the uppermost 3 km of crust. They also observed that the crust below the hypocenter (12–20 s, 15–30 km depth) suffered from significant postseismic changes in its elastic parameters, which could be due to slow transfer of the load caused by the earthquake (poroelastic relaxation).

After the 2011, M_w 9.0 Tohoku earthquake, Brenguier et al. (2014), mapped coseismic velocity changes across Japan. He scaled the velocity changes with dynamic excitation measured by strong motion sensors across the region. The changes highlighted areas with volcanic activity (volcanic chain and Mt. Fuji area). Their results pointed out that coseismic velocity reductions are likely to be mainly caused by dynamic strain that is location dependent. Over-pressurized fluids that are typical for volcanic regions increase the susceptibility, i.e., the seismic velocity change induced by perturbations. This has also been observed for an earthquake M_w 7.6 in the subduction zone off Costa Rica (Chaves & Schwartz, 2016).

Earthquake precursory signals have been targeted using CWI (Stehly, Froment, Campillo, Liu, & Chen, 2015). However, even for large

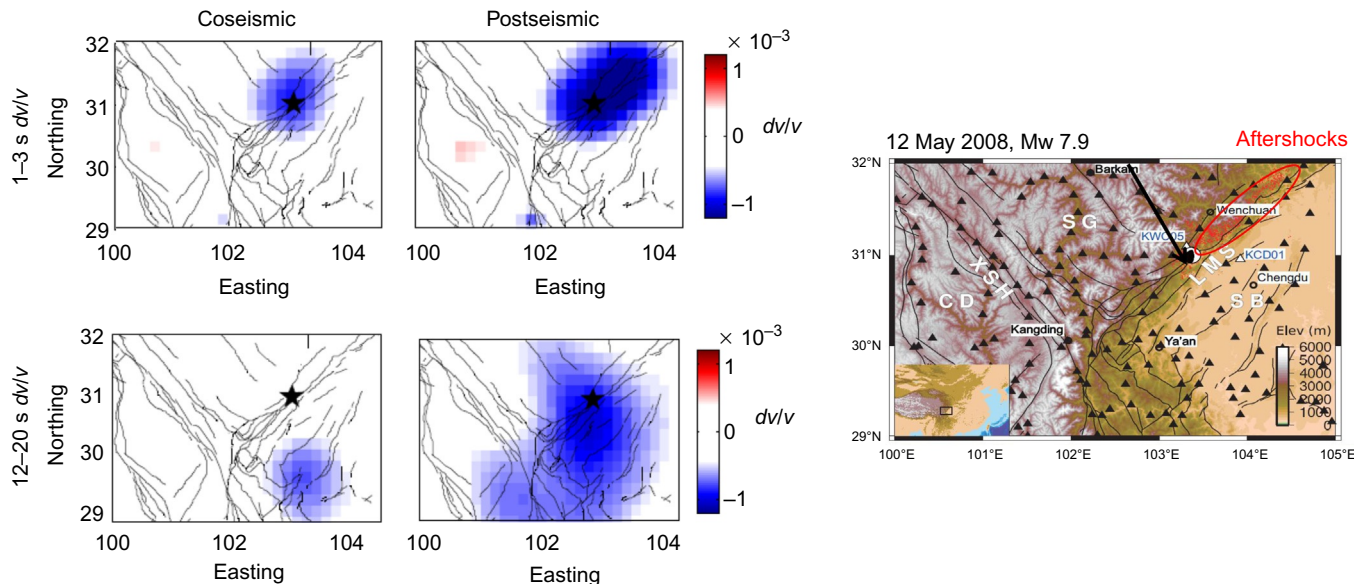
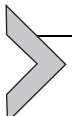


Fig. 30 Spatial distribution of coseismic and postseismic velocity changes related to the 2008, M_w 7.9 Wenchuan earthquake at shallow depth (1–3 s, 1–5 km) and in the crust (12–20 s, 15–20 km). Modified after Obermann, A., Froment, B., Campillo, M., Larose, E., Planès, T., Valette, B., ... Liu, Q. Y. (2014). Seismic noise correlations to image structural and mechanical changes associated with the mw 7.9 2008 Wenchuan earthquake. *Journal of Geophysical Research*, 119(4), 3155–3168. 10.1002/2013JB010932.

earthquake ruptures occurring within densely instrumented areas, as was the case for the 2008, M7.9 Wenchuan earthquake, and a temporal resolution of 1 day, [Stehly et al. \(2015\)](#) did not succeed in detecting any precursory signals as they had been reported in laboratory experiments (e.g., [Latour, Schubnel, Nielsen, Madariaga, & Vinciguerra, 2013](#)). Tests in controlled underground facilities under real stress conditions, such as experiments in the Swiss Alpes ([Gischig et al., 2019](#)), are keenly anticipated to demonstrate the general resolution of precursory signals.



8. Outlook

Interferometric time-lapse applications in seismology gained popularity in the early 2000s after it was demonstrated that surface waves can be retrieved from the ambient seismic field with passive interferometry methods. Since then this concept has been applied in a wide variety of contexts including laboratory experiments, medical applications, nondestructive monitoring of concrete and infrastructures, reservoir monitoring for engineering projects, predictions of volcanic unrest, and the assessment of crustal damage and healing processes after moderate-size and large earthquakes. These developments have been benefiting from advancements in sensor technology and thus from the densification of permanent seismic networks and temporary array installations, but also from the simultaneous progress in data storage capacities, archiving, and distribution. Noise correlation-based analysis techniques constitute a key part of these modern developments that help to increase the scientific gain from the generated data volumes.

These techniques will continue to play a significant role in seismic imaging and monitoring applications as the data availability will likely continue to increase. Emerging technologies like “Distributed Acoustic Sensing” allow now spatially continuous wavefield sampling, and new types of marine sensors will close the vast acquisition gaps of the oceans.

Theoretical advancements are expected from better scattered wave propagation models that can take the mode conversion properly into account. Here, work toward analytical expressions or more efficient computational strategies can both yield significant progress. This will help to better locate or image the detected subsurface changes, which will allow an overall better spatio-temporal resolution of dynamic processes. It can also be envisioned that modern data classification methods that root in machine learning and pattern recognition techniques can contribute to the reconstruction of improved Green’s function estimates by labeling record sections of “proper” noise segments.

Acknowledgment

We thank L. Ermert and the Editor C. Schmelzbach, whose comments helped to improve this chapter.

References

- Aki, K. (1957). Space and time spectra of stationary stochastic waves, with special reference to microtremors. *Bulletin of the Earthquake Research Institute*, 35, 415–456.
- Aki, K. (1969). Analysis of seismic coda of local earthquake as scattered waves. *Journal of Geophysical Research*, 74(2), 615–631.
- Aki, K., & Chouet, B. (1975). Origin of coda waves: Source, attenuation and scattering effects. *Journal of Geophysical Research*, 80(23), 3322–3342.
- Aki, K., & Richards, P. G. (1980). Vol. I. *Quantitative Seismology: Theory and Methods*. WH Freeman & Co.
- Anderson, J., & Nerenst, P. (1952). Wave velocity in concrete. *J Proc*, 48, 613–635.
- Anderson, P. W. (1958). Absence of diffusion in certain random lattices. *Physical Review Letters*, 100, 1492.
- Anggono, T., Nishimura, T., Sato, H., Ueda, H., & Ukawa, M. (2012). Spatio-temporal changes in seismic velocity associated with the 2000 activity of Miyakejima volcano as inferred from cross-correlation analyses of ambient noise. *Journal of Volcanology and Geothermal Research*, 247, 93–107.
- Ardhuin, F., Gualtieri, L., & Stutzmann, E. (2015). How ocean waves rock the Earth: Two mechanisms explain microseisms with periods 3 to 300 s. *Geophysical Research Letters*, 42, 765–772. <https://doi.org/10.1002/2014GL062782>.
- Ardhuin, F., Stutzmann, E., Schimmel, M., & Mangeney, A. (2011). Ocean wave sources of seismic noise. *Journal of Geophysical Research: Oceans*, 116(C9), 1–21.
- Armbruster, J. G., Kim, W.-Y., & Rubin, A. M. (2014). Accurate tremor locations from coherent S and P waves. *Journal of Geophysical Research: Solid Earth*, 119(6), 5000–5013.
- Arroucau, P., Rawlinson, N., & Sambridge, M. (2010). New insight into Cainozoic sedimentary basins and Palaeozoic suture zones in southeast Australia from ambient noise surface wave tomography. *Geophysical Research Letters*, 37, L07303.
- Arts, R. J., Elsayed, R., Van Der Meer, L., Eiken, O., Ostmo, S., Chadwick, A., & Zinszner, B. (2002). Estimation of the mass of injected CO₂ at Sleipner using time-lapse seismic data. In *64th EAGE conference & exhibition*.
- American Society of Civil Engineers. (2013). *Levees, In 2013 report card for America's infrastructure*. American Society of Civil Engineers.
- Azam, S., & Li, Q. (2010). Tailings dam failures: A review of the last one hundred years. *Geotechnical News*, 28(4), 50–54.
- Backus, M., Burg, J., Baldwin, D., & Bryan, E. (1964). Wide band extraction of mantle p waves from ambient noise. *Geophysics*, 29, 672–692.
- Baig, A. M., Campillo, M., & Brenguier, F. (2009). Denoising seismic noise correlations. *Journal of Geophysical Research*, 114, 1–12. <https://doi.org/10.1029/2008JB006085>.
- Bakulin, A., & Calvert, R. (2004). Virtual source: New method for imaging and 4D below complex overburden. *SEG technical program expanded abstracts 2004* (pp. 2477–2480). Society of Exploration Geophysicists.
- Baskir, E., & Weller, C. E. (1975). Sourceless reflection seismic exploration. *Geophysics*, 40, 158–159.
- Bensen, G. D., Ritzwoller, M. H., Barmin, M. P., Levshin, A. L., Lin, F., Moschetti, M. P., ... Yang, Y. (2007). Pre-eruptive migration of earthquakes at the Piton de la Fournaise volcano (Réunion Island). *Geophysical Journal International*, 169, 1239–1260.

- Bensen, G. D., Ritzwoller, M. H., & Shapiro, N. M. (2008). Broadband ambient noise surface wave tomography across the United States. *Journal of Geophysical Research*, 113(B5), 1239–1260.
- Bercoff, J., Tanter, M., & Fink, M. (2004). Supersonic shear imaging: a new technique for soft tissue elasticity mapping. *IEEE Transactions on Ultrasonics, Ferroelectrics, and Frequency Control*, 51(4), 396–409.
- Berthaud, Y. (1991). Damage measurements in concrete via an ultrasonic technique. Part I experiment. *Cement and Concrete Research*, 21(1), 73–82.
- Bonnefoy-Claudet, S., Cotton, F., & Bard, P. (2006). The nature of noise wavefield and its applications for site effects studies: A literature review. *Earth-Science Reviews*, 79(3–4), 205–227.
- Boué, P., Poli, P., Campillo, M., Pedersen, H., Briad, X., & Roux, P. (2013). Teleseismic correlations of ambient seismic noise for deep global imaging of the Earth. *Geophysical Journal International*, 194(2), 844–848.
- Breitenbach, A. J. (2010). Overview: Tailings disposal and dam construction practices in the 21st century. In *International conference on tailings & mine waste, tailings and mine waste: Vol. 10* (pp. 49–57).
- Brenguier, F., Campillo, M., Hadzioannou, C., Shapiro, N. M., Nadeau, R. M., & Larose, E. (2008). Postseismic relaxation along the San Andreas fault at Parkfield from continuous seismological observations. *Science*, 321, 1478–1481.
- Brenguier, F., Campillo, M., Takeda, T., Aoki, Y., Shapiro, N., Briand, X., ... Miyake, H. (2014). Mapping pressurized volcanic fluids from induced crustal seismic velocity drops. *Science*, 345(6192), 80–82.
- Brenguier, F., Rivet, D., Obermann, A., Nakata, N., Boué, P., Lecocq, T., ... Shapiro, N. (2016). 4-D noise-based seismology at volcanoes: Ongoing efforts and perspectives. *Journal of Volcanology and Geothermal Research*, 321, 182–195.
- Brenguier, F., Shapiro, N. M., Campillo, M., Ferrazzini, V., Duputel, Z., Coutant, O., & Nercissian, A. (2008). Towards forecasting volcanic eruptions using seismic noise. *Nature Geoscience*, 1, 126–130.
- Bromirski, P. D., & Duennebier, F. K. (2002). The near-coastal microseism spectrum: Spatial and temporal wave climate relationships. *Journal of Geophysical Research*, 107(B8), 1–20.
- Budi-Santoso, A., & Lesage, P. (2016). Velocity variations associated with the large 2010 eruption of Merapi volcano, Java, retrieved from seismic multiplets and ambient noise cross-correlation. *Geophysical Journal International*, 206(1), 221–240.
- Burtin, A., Bollinger, L., Vergne, J., Cattin, R., & Nábělek, J. L. (2008). Spectral analysis of seismic noise induced by rivers: A new tool to monitor spatiotemporal changes in stream hydrodynamics. *Journal of Geophysical Research*, 113, 1–14. <https://doi.org/10.1029/2007JB005034>.
- Calò, M., Kinnaert, X., & Dorbath, C. (2013). Procedure to construct three-dimensional models of geothermal areas using seismic noise cross-correlations: Application to the Soultz-sous-Forêts enhanced geothermal site. *Geophysical Journal International*, 194(3), 1893–1899.
- Campillo, M. (2006). Phase and correlation of ‘random’ seismic fields and the reconstruction of the green function. *Pure and Applied Geophysics*, 163, 475–502. <https://doi.org/10.1007/s00024-005-0032-8>.
- Campillo, M., & Paul, A. (2003). Long-range correlations in the diffuse seismic coda. *Science*, 299, 547–549.
- Campillo, M., & Roux, P. (2015). Crust and lithospheric structure—Seismic imaging and monitoring with ambient noise correlations. In G. Schubert (Ed.), Vol. 1. *Treatise on geophysics* (pp. 391–417). Oxford, UK: Elsevier. (Ed.).
- Catheline, S. (2017). Passive elastography: A shear wave tomography of the human body. *The Journal of the Acoustical Society of America*, 141(5), 3527. 3527.

- Catheline, S., Benech, N., Brum, J., & Negreira, C. (2008). Time reversal of elastic waves in soft solids. *Physical Review Letters*, 100(6), 064301.
- Cessaro, R. K. (1994). Sources of primary and secondary microseisms. *Bulletin of the Seismological Society of America*, 84, 142–148.
- Chadwick, A., Williams, G., Delepine, N., Clochard, V., Labat, K., Sturton, S., et al. (2010). Quantitative analysis of time-lapse seismic monitoring data at the Sleipner CO₂ storage operation. *The Leading Edge*, 29(2), 170–177.
- Chaput, J., Clerc, V., Campillo, M., Roux, P., & Knox, H. (2016). On the practical convergence of coda-based correlations: A window optimization approach. *Geophysical Journal International*, 204(2), 736–747. <https://doi.org/10.1093/gji/ggv476>.
- Chaves, E. J., & Schwartz, S. Y. (2016). Monitoring transient changes within overpressured regions of subduction zones using ambient seismic noise. *Science Advances*, 2(1), e1501289.
- Chen, J. H., Froment, B., Liu, Q. Y., & Campillo, M. (2010). Distribution of seismic wave speed changes associated with the 12 May 2008 Mw 7.9 Wenchuan earthquake. *Geophysical Research Letters*, 37(L18302), 1–4. <https://doi.org/10.1029/2010GL044582>.
- Chevrot, S., Sylvander, M., Benahmed, S., Ponsolles, C., Lefvre, J. M., & Paradis, D. (2007). Source locations of secondary microseisms in western Europe: Evidence for both coastal and pelagic sources. *Journal of Geophysical Research*, 112, B11301.
- Claerbout, J. F. (1968). Synthesis of a layered medium from its acoustic transmission response. *Geophysics*, 33(2), 264–269.
- Clarke, D., Zaccarelli, L., Shapiro, N. M., & Brenguier, F. (2011). Assessment of resolution and accuracy of the moving window cross spectral technique for monitoring crustal temporal variations using ambient seismic noise. *Geophysical Journal International*, 186, 867–882.
- Clements, T., & Denolle, M. A. (2018). Tracking groundwater levels using the ambient seismic field. *Geophysical Research Letters*, 45(13), 6459–6465.
- Colombi, A., Chaput, J., Brenguier, F., Hillers, G., Roux, P., & Campillo, M. (2014). On the temporal stability of the coda of ambient noise correlations. *Comptes Rendus Geoscience*, 346(11–12), 307–316.
- Curtis, A., Gerstoft, P., Sato, H., Snieder, R., & Wapenaar, K. (2006). Seismic interferometry—Turning noise into signal. *The Leading Edge*, 25(9), 1082–1092.
- Davies, M. P. (2002). Tailings impoundment failures are geotechnical engineers listening? *Geotechnical News*, 20(3), 31–36.
- Del Pezzo, E., Bianco, F., & Saccorotti, G. (2001). Separation of intrinsic and scattering Q for volcanic tremor: An application to Etna and Masaya volcanoes. *Geophysical Research Letters*, 28, 3083–3086.
- De Plaen, R. S., Cannata, A., Cannavo, F., Caudron, C., Lecocq, T., & Francis, O. (2019). Temporal changes of seismic velocity caused by volcanic activity at Mt. Etna revealed by the autocorrelation of ambient seismic noise. *Frontiers in Earth Science*, 6, 251.
- De Ridder, S. A. L. (2014). Passive seismic surface-wave interferometry for reservoir-scale imaging (Unpublished doctoral dissertation). Stanford University.
- De Ridder, S. A. L., & Biondi, B. L. (2013). Daily reservoir-scale subsurface monitoring using ambient seismic noise. *Geophysical Research Letters*, 40(12), 2969–2974.
- Derode, A., Larose, E., Campillo, M., & Fink, M. (2003). How to estimate the Green's function of a heterogeneous medium between two passive sensors? Application to acoustic waves. *Applied Physics Letters*, 83(15), 3054–3056.
- Derode, A., Larose, E., Tanter, M., de Rosny, J., Tourin, A., Campillo, M., & Fink, M. (2003). Recovering the Green's function from field-field correlations in an open scattering medium. *The Journal of the Acoustical Society of America*, 113(6), 2973–2976.
- Diehl, T., Kraft, T., Kissling, E., Deichmann, N., Clinton, J., & Wiemer, S. (2014). High-precision relocation of induced seismicity in the geothermal system below St. Gallen (Switzerland). *Geophysical Research Abstracts, EGU General Assembly*, 16 (EGU2014-12541-1).

- Donaldson, C., Caudron, C., Green, R. G., Thelen, W. A., & White, R. S. (2017). Relative seismic velocity variations correlate with deformation at ki-lauea volcano. *Science Advances*, 3(6), e1700219.
- Dong, S., He, R., & Schuster, G. T. (2006). Interferometric prediction and least squares subtraction of surface waves. *SEG technical program expanded abstracts 2006* (pp. 2783–2786). Society of Exploration Geophysicists.
- Draganov, D., Campman, X., Thorbecke, J., Verdel, A., & Wapenaar, K. (2009). Reflection images from ambient seismic noise. *Geophysics*, 74(5), A63–A67.
- Draganov, D., Heller, K., & Ghose, R. (2012). Monitoring CO₂ storage using ghost reflections retrieved from seismic interferometry. *International Journal of Greenhouse Gas Control*, 11, S35–S46.
- Draganov, D., Wapenaar, K., Mulder, W., Singer, J., & Verdel, A. (2007). Retrieval of reflections from seismic background-noise measurements. *Geophysical Research Letters*, 34(4), 1–4.
- Duputel, Z., Ferrazzini, V., Brenguier, F., Shapiro, N. M., Campillo, M., & Nercessian, A. (2009). Real time monitoring of relative velocity changes using ambient seismic noise at the Piton de la Fournaise volcano (La Réunion) from January 2006 to June 2007. *Journal of Volcanology and Geothermal Research*, 184(1), 164–173.
- Dyer, B. C., Schanz, U., Spillmann, T., Ladner, F., & Häring, M. O. (2010). Application of microseismic multiplet analysis to the Basel geothermal reservoir stimulation events. *Geophysical Prospecting*, 58(5), 791–807.
- Ebrahimian, M., Rahmani, M., & Todorovska, M. I. (2014). Nonparametric estimation of wave dispersion in high-rise buildings by seismic interferometry. *Earthquake Engineering & Structural Dynamics*, 43(15), 2361–2375.
- Ekström, G., Abers, G. A., & Webb, S. C. (2009). Determination of surface-wave phase velocities across USArray from noise and Aki's spectral formulation. *Geophysical Research Letters*, 36, 1–5, L18301.
- Elgar, S., Herbers, T. H. C., & Guza, R. T. (1994). Reflection of ocean surface gravity waves from a natural beach. *Journal of Physical Oceanography*, 24, 1503–1511.
- Fell, R., Wan, C. F., Cyganiewicz, J., & Foster, M. (2003). Time for development of internal erosion and piping in embankment dams. *Journal of Geotechnical and Geoenvironmental Engineering*, 129(4), 307–314.
- Fink, M. (1992). Time reversal of ultrasonic fields, Part I: Basic principles. *IEEE Transactions on Ultrasonics, Ferroelectrics, and Frequency Control*, 39(5), 555–566.
- Freed, A. M., Ali, S. T., & Bürgmann, R. (2007). Evolution of stress in Southern California for the past 200 years from coseismic, postseismic and interseismic stress changes. *Geophysical Journal International*, 169(3), 1164–1179.
- Friedrich, A., Kruger, F., & Klinge, K. (1998). Ocean-generated microseismic noise located with the Grafenberg array. *Journal of Seismology*, 2, 47–64.
- Froment, B. (2011). Utilisation du bruit sismique ambiant dans le suivi temporel de structures géologiques (Unpublished doctoral dissertation). Université de Grenoble.
- Froment, B., Campillo, M., Chen, J. H., & Liu, Q. Y. (2013). Deformation at depth associated with the May 12, 2008 Mw 7.9 Wenchuan earthquake from seismic ambient noise monitoring. *Geophysical Research Letters*, 40, 78–82. <https://doi.org/10.1029/2012GL053995>.
- Froment, B., Campillo, M., & Roux, P. (2011). Reconstructing the green's function through iteration of correlations. *Comptes Rendus Geoscience*, 343, 623–632. <https://doi.org/10.1016/j.crte.2011.03.001>.
- Froment, B., Campillo, M., Roux, P., Gouédard, P., Verdel, A., & Weaver, R. L. (2010). Estimation of the effect of nonisotropically distributed energy on the apparent arrival time in correlations. *Geophysics*, 75(5), SA85–SA92.
- Gaite, B., Iglesias, A., Villaseñor, A., Herraiz, M., & Pacheco, J. F. (2012). Crustal structure of Mexico and surrounding regions from seismic ambient noise tomography. *Geophysical Journal International*, 188(3), 1413–1424.

- Gallot, T., Catheline, S., Roux, P., Brum, J., Benech, N., & Negreira, C. (2011). Passive elastography: Shear-wave tomography from physiological-noise correlation in soft tissues. *IEEE Transactions on Ultrasonics, Ferroelectrics, and Frequency Control*, 58(6), 1122–1126.
- Gallot, T., Catheline, S., Roux, P., & Campillo, M. (2012). A passive inverse filter for Green's function retrieval. *The Journal of the Acoustical Society of America*, 131(1), EL21–EL27. <https://doi.org/10.1121/1.3665397>.
- Garnier, J., & Papanicolaou, G. (2016). *Passive imaging with ambient noise*. Cambridge, UK: Cambridge University Press (Eds.).
- Gassenmeier, M., Sens-Schönfelder, C., Delatre, M., & Korn, M. (2015). Monitoring of environmental influences on seismic velocity at the geological storage site for CO₂ in Ketzin (Germany) with ambient seismic noise. *Geophysical Journal International*, 200(1), 524–533.
- Gerstoft, P., Fehler, M. C., & Sabra, K. G. (2006). When Katrina hit California. *Geophysical Research Letters*, 33, L1730.
- Gerstoft, P., Shearer, P. M., Harmon, N., & Zhang, J. (2008). Global P, PP, and PKP wave microseisms observed from distant storms. *Geophysical Research Letters*, 35, L23306.
- Gischig, V., Amann, F., Bethmann, F., Brixel, B., Doetsch, J., Gholizadeh Doonechaly, N., ... Giardini, D. (2019). Hydraulic stimulation and fluid circulation experiments in underground laboratories: Stepping up the scale towards engineered geothermal systems. *Geomechanics for Energy and the Environment*.
- Gómez-García, C., Brenguier, F., Boué, P., Shapiro, N. M., Droznin, D. V., Droznina, S. Y., ... Gordeev, E. I. (2018). Retrieving robust noise-based seismic velocity changes from sparse data sets: Synthetic tests and application to Klyuchevskoy volcanic group (Kamchatka). *Geophysical Journal International*, 214(2), 1218–1236.
- Gouédard, P., Roux, P., Campillo, M., & Verdel, A. (2008). Convergence of the two-point correlation function toward the Green's function in the context of a seismic-prospecting data set. *Geophysics*, 73(6), 47–53. <https://doi.org/10.1190/1.2985822>.
- Grêt, A., Snieder, R., Aster, R. C., & Kyle, P. R. (2005). Monitoring rapid temporal change in a volcano with coda wave interferometry. *Geophysical Research Letters*, 32(6), L06304.
- Grêt, A., Snieder, R., & Özbay, U. (2006). Monitoring in situ stress changes in a mining environment with coda wave interferometry. *Geophysical Journal International*, 167(2), 504–508.
- Grêt, A., Snieder, R., & Scales, J. (2006). Time-lapse monitoring of rock properties with coda wave interferometry. *Journal of Geophysical Research: Solid Earth*, 111(B3), B03305.
- Gutenberg, B. (1936). On microseisms. *Bulletin of the Seismological Society of America*, 26(2), 111–117.
- Hadjioannou, C., Larose, E., Baig, A., Roux, P., & Campillo, M. (2011). Improving temporal resolution in ambient noise monitoring of seismic wave speed. *Journal of Geophysical Research: Solid Earth (1978–2012)*, 116(B7), B07304.
- Hadjioannou, C., Larose, E., Coutant, O., Roux, P., & Campillo, M. (2009). Stability of monitoring weak changes in multiply scattering media with ambient noise correlation: Laboratory experiments. *The Journal of the Acoustical Society of America*, 125(6), 3688–3695.
- Halliday, D. F., Curtis, A., Robertsson, J. O. A., & van Manen, D.-J. (2007). Interferometric surface-wave isolation and removal. *Geophysics*, 72(5), A69–A73.
- Häring, P. C., Schanz, U., Ladner, F., & Dyer, B. C. (2008). Characterisation of the Basel 1 enhanced geothermal system. *Geothermics*, 37, 469–495.
- Hasselmann, K. (1963). A statistical analysis of the generation of microseisms. *Revista Geográfica*, 1(2), 177–210.
- Hatchell, P. J., Wills, P. B., & Didraga, C. (2009). Production induced effects on near-surface wave velocities at valhall. In *71st EAGE Conference and Exhibition incorporating SPE EUROPEC 2009*.

- He, R., Hornby, B., & Schuster, G. (2007). 3D wave-equation interferometric migration of VSP free-surface multiples. *Geophysics*, 72(5), S195–S203.
- Henrino, R., Tregoures, N., Shapiro, N. M., Margerin, L., Campillo, M., van Tiggelen, B. A., & Weaver, R. L. (2001). Observation of equipartition of seismic waves. *Physical Review Letters*, 86(15), 3447–3450.
- Herraiz, M., & Espinoza, A. F. (1997). Coda waves: A review. *Pure and Applied Geophysics*, 125(4), 499–577.
- Hillers, G., & Ben-Zion, Y. (2011). Seasonal variations of observed noise amplitudes at 2–18 Hz in southern California. *Geophysical Journal International*, 184(2), 860–868.
- Hillers, G., Ben-Zion, Y., Campillo, M., & Zigone, D. (2015). Seasonal variations of seismic velocities in the San Jacinto fault area observed with ambient seismic noise. *Geophysical Journal International*, 202, 920–932. <https://doi.org/10.1093/gji/ggv151>.
- Hillers, G., & Campillo, M. (2016). Fault zone reverberations from cross-correlations of earthquake waveforms and seismic noise. *Geophysical Journal International*, 204(3), 1503–1517. <https://doi.org/10.1093/gji/ggv515>.
- Hillers, G., & Campillo, M. (2018). Fault zone imaging from correlations of aftershock waveforms. *Pure and Applied Geophysics*, 175, 2643–2667. <https://doi.org/10.1007/s00024-018-1836-7>.
- Hillers, G., Campillo, M., Ben-Zion, Y., & Roux, P. (2014). Seismic fault zone trapped noise. *Journal of Geophysical Research*, 119(7), 5786–5799. <https://doi.org/10.1002/2014JB011217>.
- Hillers, G., Campillo, M., Brenguier, F., Moreau, L., Agnew, D., & Ben-Zion, Y. (2019). Seismic velocity change patterns along the San Jacinto fault zone following the 2010 M7.2 El Mayor-Cucapah and M5.4 Collins Valley earthquakes. *Journal of Geophysical Research Solid Earth*, 124. <https://doi.org/10.1029/2018JB017143>.
- Hillers, G., Campillo, M., Lin, Y. Y., Ma, K. F., & Roux, P. (2012). Anatomy of the high-frequency ambient seismic wave field at the TCDP borehole. *Journal of Geophysical Research*, 117, B06301. <https://doi.org/10.1029/2011JB008999>.
- Hillers, G., Graham, N., Campillo, M., Kedar, S., Landès, M., & Shapiro, N. (2012). Global oceanic microseism sources as seen by seismic arrays and predicted by wave action models. *Geochemistry, Geophysics, Geosystems*, 13(1), 1–19.
- Hillers, G., Husen, S., Obermann, A., Planès, T., Campillo, M., & Larose, E. (2015). Noise-based monitoring and imaging of aseismic transient deformation induced by the 2006 Basel reservoir stimulation. *Geophysics*, 80(4), KS51–KS68. <https://doi.org/10.1190/GEO2014-0455.1>.
- Hillers, G., Husen, S., Obermann, A., Planès, T., Larose, E., & Campillo, M. (2015). Noise-based monitoring and imaging of aseismic transient deformation induced by the 2006 Basel reservoir stimulation. *Geophysics*, 80(4), 51–68. <https://doi.org/10.1190/GEO2014-0455.1>.
- Hillers, G., Retailleau, L., Campillo, M., Inbal, A., Ampuero, J. P., & Nishimura, T. (2015). In situ observations of velocity changes in response to tidal deformation from analysis of the high-frequency ambient wavefield. *Journal of Geophysical Research*, 120, 210–225. <https://doi.org/10.1002/2014JB011318>.
- Hillers, G., Roux, P., Campillo, M., & Ben-Zion, Y. (2016). Focal spot imaging based on zero lag cross correlation amplitude fields: Application to dense array data at the San Jacinto fault zone. *Journal of Geophysical Research Solid Earth*, 121, 8048–8067. <https://doi.org/10.1002/2016JB013014>.
- Hobiger, M., Wegler, U., Shiomi, K., & Nakahara, H. (2012). Coseismic and postseismic elastic wave velocity variations caused by the 2008 Iwate-Miyagi Nairiku earthquake, Japan. *Journal of Geophysical Research*, 117(B9), 1–19.
- Hobiger, M., Wegler, U., Shiomi, K., & Nakahara, H. (2016). Coseismic and post-seismic velocity changes detected by passive image interferometry: Comparison of one great and five strong earthquakes in Japan. *Geophysical Journal International*, 205(2), 1053–1073.

- Hoshiba, M. (1997). Seismic coda wave envelope in depth-dependent S wave velocity structure. *Physics of the Earth and Planetary Interiors*, 104, 15–22.
- Inbal, A., Cristea-Platon, T., Ampuero, J. P., Hillers, G., Agnew, D., & Hough, S. E. (2018). Sources of long-range anthropogenic noise in southern California and implications for tectonic tremor detection. *Bulletin of the Seismological Society of America*, 108(6), 3511–3527. <https://doi.org/10.1785/0120180130>.
- Iyer, H. M., & Healy, J. H. (1972). Evidence for the existence of locally generated body waves in the short-period noise at the large aperture seismic array. *Bulletin of the Seismological Society of America*, 62, 13–29.
- James, S. R., Knox, H. A., Abbott, R. E., & Screamton, E. J. (2017). Improved moving window cross-spectral analysis for resolving large temporal seismic velocity changes in permafrost. *Geophysical Research Letters*, 44(9), 4018–4026.
- Jin, A., & Aki, K. (1988). Spatial and temporal correlation between coda Q and seismicity in China. *Bulletin of the Seismological Society of America*, 78, 741–769.
- Johanson, I. A., Fielding, E. J., Rolandone, F., & Bürgmann, R. (2006). Coseismic and postseismic slip of the 2004 Parkfield earthquake from space-geodetic data. *Bulletin of the Seismological Society of America*, 96(4B), S269–S282.
- Kang, T. S., & Shin, J. S. (2006). Surface-wave tomography from ambient seismic noise of accelerograph networks in southern Korea. *Geophysical Research Letters*, 33, L17303.
- Kanu, C., & Snieder, R. (2015a). Numerical computation of the sensitivity kernel for monitoring weak changes with multiply scattered acoustic waves. *Geophysical Journal International*, 203(3), 1923–1936.
- Kanu, C., & Snieder, R. (2015b). Time-lapse imaging of a localized weak change with multiply scattered waves using numerical-based sensitivity kernel. *Journal of Geophysical Research: Solid Earth*, 120(8), 5595–5605.
- Kasatkina, E., Koulikov, I., West, M., & Izbekov, P. (2014). Seismic structure changes beneath Redoubt Volcano during the 2009 eruption inferred from local earthquake tomography. *Journal of Geophysical Research: Solid Earth*, 119(6), 4938–4954.
- Kaveh, M. (1991). *Analogy in optics and micro-electronics*. Haarlem: Kluwer Academic.
- Kedar, S., Longuet-Higgins, M., Webb, F., Graham, N., Clayton, R., & Jones, C. (2008). The origin of deep ocean microseisms in the North Atlantic Ocean. *Proceedings of Royal Society A*, 464, 777–793. <https://doi.org/10.1098/rspa.2007.0277>.
- Keiding, M., Árnadóttir, T., Jonsson, S., Decriem, J., & Hooper, A. (2010). Plate boundary deformation and man-made subsidence around geothermal fields on the Reykjanes Peninsula, Iceland. *Journal of Volcanology and Geothermal Research*, 194(4), 139–149.
- Komlos, K., Popovics, S., Nürnbergerová, T., Babal, B., & Popovics, J. S. (1996). Ultrasonic pulse velocity test of concrete properties as specified in various standards. *Cement and Concrete Composites*, 18(5), 357–364.
- Koulikov, I., Gordeev, E. I., Dobretsov, N. L., Vernikovsky, V. A., Senyukov, S., Jakovlev, A., & Jaxybulatov, K. (2013). Rapid changes in magma storage beneath the Klyuchevskoy group of volcanoes inferred from time-dependent seismic tomography. *Journal of Volcanology and Geothermal Research*, 263, 75–91.
- Landès, M., Hubans, F., Shapiro, N. M., Paul, A., & Campillo, M. (2010). Origin of deep ocean microseisms by using teleseismic body waves. *Geophysical Journal Research*, 115(B05302), 1–14.
- Landès, M., Le Pichon, A., Shapiro, N., Hillers, G., & Campillo, M. (2014). Explaining global patterns of microbarom observations with wave action models. *Geophysical Journal International*, 199, 1328–1337. <https://doi.org/10.1093/gji/ggu324>.
- Larose, E., de Rosny, J., Margerin, L., Anache, D., Gouédard, P., Campillo, M., & van Tiggelen, B. (2006). Observation of multiple scattering of kHz vibrations in a concrete structure and application to monitoring weak changes. *Physical Review E*, 73(1), 016609.

- Larose, E., & Hall, S. (2009). Monitoring stress related velocity variation in concrete with a 2×10^{-5} relative resolution using diffuse ultrasound. *The Journal of the Acoustical Society of America*, 125(4), 1853–1856.
- Larose, E., Margerin, L., van Tiggelen, B. A., & Campillo, M. (2004). Weak Localization of seismic waves. *Physical Review Letters*, 93(4), 1–4.
- Larose, E., Obermann, A., Digulescu, A., Planès, T., Chaix, J. F., Mazerolle, F., & Moreau, G. (2015). Locating and characterizing a crack in concrete with LOCADIFF: A four-point bending test. *The Journal of the Acoustical Society of America*, 138(1), 232–241.
- Larose, E., Planès, T., Rossetto, V., & Margerin, L. (2010). Locating a small change in a multiple scattering environment. *Applied Physics Letters*, 96(204101), 1–3.
- Larose, E., Roux, P., & Campillo, M. (2007). Reconstruction of Rayleigh–Lamb dispersion spectrum based on noise obtained from an air-jet forcing. *The Journal of the Acoustical Society of America*, 122(6), 3437–3444.
- Latour, S., Schubnel, A., Nielsen, S., Madariaga, R., & Vinciguerra, S. (2013). Characterization of nucleation during laboratory earthquakes. *Geophysical Research Letters*, 40(19), 5064–5069.
- Lecocq, T., Longuevergne, L., Pedersen, H. A., Brenguier, F., & Stammler, K. (2017). Monitoring ground water storage at mesoscale using seismic noise: 30 years of continuous observation and thermo-elastic and hydrological modeling. *Scientific Reports*, 7(1), 14241.
- Lehujeur, M., Vergne, J., Maggi, A., & Schmittbuhl, J. (2017a). Ambient noise tomography with non-uniform noise sources and low aperture networks: Case study of deep geothermal reservoirs in northern Alsace, France. *Geophysical Supplements to the Monthly Notices of the Royal Astronomical Society*, 208(1), 193–210.
- Lehujeur, M., Vergne, J., Maggi, A., & Schmittbuhl, J. (2017b). Vertical seismic profiling using double-beamforming processing of nonuniform anthropogenic seismic noise: The case study of Rittershoffen, Upper Rhine Graben, France. *Geophysics*, 82(6), B209–B217.
- Lehujeur, M., Vergne, J., Schmittbuhl, J., & Maggi, A. (2015). Characterization of ambient seismic noise near a deep geothermal reservoir and implications for interferometric methods: A case study in northern Alsace, France. *Geothermal Energy*, 3(1), 3.
- Lehujeur, M., Vergne, J., Schmittbuhl, J., Zigone, D., Le Chenadec, A., & Team, EstOF (2018). Reservoir imaging using ambient noise correlation from a dense seismic network. *Journal of Geophysical Research: Solid Earth*, 123(8), 6671–6686.
- Leonhardt, F., & Baur, W. (1971). Erfahrungen mit dem Takschiebeverfahren im Bruecken-vund Hochbau. *Beton und Stahlbetonbau*, 66(7), 161–167.
- Lesage, P., Reyes-Dávila, G., & Arámbula-Mendoza, R. (2014). Large tectonic earthquakes induce sharp temporary decreases in seismic velocity in volcán de colima, mexico. *Journal of Geophysical Research: Solid Earth*, 119(5), 4360–4376.
- Lewis, M. A., & Gerstoft, P. (2012). Shear wave anisotropy from cross-correlation of seismic noise in the Parkfield pilot hole. *Geophysical Journal International*, 188, 626–630. <https://doi.org/10.1111/j.1365-246X.2011.05285.x>.
- Li, H. Y., Su, W., Wang, C. Y., & Huang, Z. X. (2009). Ambient noise Rayleigh wave tomography in western Sichuan and eastern Tibet. *Earth and Planetary Science Letters*, 282(1–4), 201–211.
- Lillamand, I., Chaix, J.-F., Ploix, M.-A., & Garnier, V. (2010). Acoustoelastic effect in concrete material under uni-axial compressive loading. *Ndt & E International*, 43(8), 655–660.
- Lin, F., Ritzwoller, M. H., Townend, J., Savage, M., & Bannister, S. (2007). Ambient noise Rayleigh wave tomography of New Zealand. *Geophysical Journal International*, 170(2), 649–666.
- Lin, F. C., & Ritzwoller, M. H. (2011). Helmholtz surface wave tomography for isotropic and azimuthally anisotropic structure. *Geophysical Journal International*, 186, 1104–1120. <https://doi.org/10.1111/j.1365-246X.2011.05070.x>.

- Lin, F. C., Ritzwoller, M. H., & Snieder, R. (2009). Eikonal tomography: Surface wave tomography by phase front tracking across a regional broad-band seismic array. *Geophysical Journal International*, 177, 1091–1110. <https://doi.org/10.1111/j.1365-246X.2009.04105.x>.
- Lin, F. C., Tsai, V. C., Schmandt, B., Duputel, Z., & Zhan, Z. (2013). Extracting seismic core phases with array interferometry. *Geophysical Research Letters*, 40(6), 1049–1053.
- Liu, S., Bundur, Z. B., Zhu, J., & Ferron, R. D. (2016). Evaluation of self-healing of internal cracks in biomimetic mortar using coda wave interferometry. *Cement and Concrete Research*, 83, 70–78.
- Lobkis, O. I., & Weaver, R. L. (2001). On the emergence of the green's function in the correlations of a diffuse field. *The Journal of the Acoustical Society of America*, 110(6), 3011–3017.
- Lobkis, O. I., & Weaver, R. L. (2003). Coda-wave interferometry in finite solids: Recovery of P-to-S conversion rates in an elastodynamic billiard. *Physical Review Letters*, 90(254302), 1–4.
- Longuet-Higgins, M. S. (1950). A theory of the origin of microseisms. *Philosophical Transactions of the Royal Society A*, 243, 1–35.
- MacGregor, P., Fell, R., Stapledon, D., Bell, G., & Foster, M. (2014). *Geotechnical engineering of dams*. CRC Press.
- Mainsant, G., Larose, E., Brönnimann, C., Jongmans, D., Michoud, C., & Jaboyedoff, M. (2012). Ambient seismic noise monitoring of a clay landslide: Toward failure prediction. *Journal of Geophysical Research*, 117, F01030.
- Mao, S., Campillo, M., van der Hilst, R. D., Brenguier, F., Stehly, L., & Hillers, G. (2019). High temporal resolution monitoring of small variations in crustal strain by dense seismic arrays. *Geophysical Research Letters*, 46, 128–137. <https://doi.org/10.1029/2018GL079944>.
- Margerin, L., Campillo, M., Shapiro, N. M., & van Tiggelen, B. (1999). Residence time of diffuse waves in the crust and the physical interpretation of coda Q. Application to seismograms recorded in Mexico. *Geophysical Journal International*, 138, 343–352.
- Margerin, L., Planès, T., Mayor, J., & Calvet, M. (2016). Sensitivity kernels for coda-wave interferometry and scattering tomography: Theory and numerical evaluation in two-dimensional anisotropically scattering media. *Geophysical Journal International*, 204(1), 650–666.
- Martin, T. E., & McRoberts, E. C. (1999). Some considerations in the stability analysis of upstream tailings dams. In *Proceedings of the sixth international conference on tailings and mine waste*. Vol. 99 (pp. 287–302).
- Masera, D., Bocca, P., & Grazzini, A. (2011). Coda wave interferometry method applied in structural monitoring to assess damage evolution in masonry and concrete structures. *Journal of Physics: Conference Series*, 305, 012108.
- Mehta, K., Sheiman, J. L., Snieder, R., & Calvert, R. (2008). Strengthening the virtual-source method for time-lapse monitoring. *Geophysics*, 73(3), S73–S80.
- Meier, U., Shapiro, N. M., & Brenguier, F. (2010). Detecting seasonal variations in seismic velocities within Los Angeles basin from correlations of ambient seismic noise. *Geophysical Journal International*, 181, 985–996.
- Michaels, J. E., & Michaels, T. E. (2005). Detection of structural damage from the local temporal coherence of diffuse ultrasonic signals. *IEEE Transactions on Ultrasonics, Ferroelectrics and Frequency Control*, 52(10), 1769–1782.
- Mikesell, D., van Wijk, K., Calvert, A., & Haney, M. (2009). The virtual refraction: Useful spurious energy in seismic interferometry. *Geophysics*, 74(3), A13–A17.
- Mikesell, T., Malcolm, A. E., Yang, D., & Haney, M. M. (2015). A comparison of methods to estimate seismic phase delays: Numerical examples for coda wave interferometry. *Geophysical Journal International*, 202, 347–360. <https://doi.org/10.1093/gji/ggv138>.

- Minato, S., Onishi, K., Matsuoka, T., Okajima, Y., Tsuchiyama, J., Nobuoka, D., ... Iwamoto, T. (2007). Crosswell seismic survey without borehole source. *SEG technical program expanded abstracts 2007* (pp. 1357–1361). Society of Exploration Geophysicists.
- Minato, S., Tsuji, T., Ohmi, S., & Matsuoka, T. (2012). Monitoring seismic velocity change caused by the 2011 Tohoku-oki earthquake using ambient noise records. *Geophysical Research Letters*, 39(9).
- Mordret, A., Jolly, A. D., Duputel, Z., & Fournier, N. (2010). Monitoring of phreatic eruptions using interferometry on retrieved cross-correlation function from ambient seismic noise: Results from Mt. Ruapehu, New Zealand. *Journal of Volcanology and Geothermal Research*, 191(1–2), 46–59.
- Mordret, A., Mikesell, T. D., Harig, C., Lipovsky, B. P., & Prieto, G. A. (2016). Monitoring southwest greenland's ice sheet melt with ambient seismic noise. *Science Advances*, 2(5), e1501538.
- Mordret, A., Rivet, D., Landès, M., & Shapiro, N. M. (2015). 3-D shear-velocity anisotropic model of Piton de la Fournaise volcano (La Réunion Island) from ambient seismic noise. *Journal of Geophysical Research: Solid Earth*, 120(1), 406–427.
- Mordret, A., Shapiro, N. M., & Singh, S. (2014). Seismic noise-based time-lapse monitoring of the valhall overburden. *Geophysical Research Letters*, 41(14), 4945–4952.
- Moreau, L., Stehly, L., Boué, P., Lu, Y., & Campillo, M. (2017). Improving ambient noise correlation functions with an SVD-based Wiener filter. *Geophysical Journal International*, 211, 418–426. <https://doi.org/10.1093/gji/ggx306>.
- Moschetti, M. P., Ritzwoller, M. H., & Shapiro, N. M. (2007). Surface wave tomography of the western United States from ambient seismic noise: Rayleigh wave group velocity maps. *Geochemistry, Geophysics, Geosystems*, 8, Q08010.
- Naffa, S. O., Goueygou, M., Piwakowski, B., & Buyle-Bodin, F. (2002). Detection of chemical damage in concrete using ultrasound. *Ultrasonics*, 40(1–8), 247–251.
- Nakata, N., & Beroza, G. C. (2015). Stochastic characterization of mesoscale seismic velocity heterogeneity in Long Beach, California. *Geophysical Journal International*, 203(3), 2049–2054.
- Nakata, N., Gaultieri, L., & Fichtner, A. (2019). *Seismic ambient noise*. New York: Cambridge University Press. <https://doi.org/10.1017/9781108264808>.
- Nakata, N., & Kashima, T. (2018). Time-lapse changes in seismic response of building over 20 years due to earthquakes and aging. *Eleventh U.S. National Conference on Earthquake Engineering*.
- Nakata, N., & Snieder, R. (2011). Near-surface weakening in Japan after the 2011 Tohoku-Oki earthquake. *Geophysical Research Letters*, 38(17), L17302.
- Nakata, N., & Snieder, R. (2014). Monitoring a building using deconvolution interferometry. II: Ambient-vibration analysis. *Bulletin of the Seismological Society of America*, 104(1), 204–213. <https://doi.org/10.1785/0120130050>.
- Nakata, N., Snieder, R., Kuroda, S., Ito, S., Aizawa, T., & Kunimi, T. (2013). Monitoring a building using deconvolution interferometry. I: Earthquake-data analysis. *Bulletin of the Seismological Society of America*, 103(3), 1662–1678.
- Nayak, A., Brenguier, F., & Manga, M. (2018). Monitoring reservoir response to earthquakes and fluid extraction, Salton sea geothermal field, California. *Science Advances*, 4(1), e1701536.
- Niederleithinger, E., Sens-Schönfelder, C., Grothe, S., & Wiggenhauser, H. (2014). Coda wave interferometry used to localize compressional load effects in a concrete specimen. In *EWSHM-7th European workshop on structural health monitoring*.
- Nightingale, K., Soo, M. S., Nightingale, R., & Trahey, G. (2002). Acoustic radiation force impulse imaging: In vivo demonstration of clinical feasibility. *Ultrasound in Medicine & Biology*, 28(2), 227–235.
- Nishida, K. (2013). Global propagation of body waves revealed by cross-correlation analysis of seismic hum. *Geophysical Research Letters*, 40(9), 1691–1696.

- Nishida, K., Kobayashi, N., & Fukao, Y. (2002). Origin of Earth's ground noise from 2 to 20 mHz. *Geophysical Research Letters*, 28(10), 1–4.
- Nishimura, T., Uchida, N., Sato, H., Ohtake, M., Tanaka, S., & Hamaguchi, H. (2000). Temporal changes of the crustal structure associated with the M6. 1 earthquake on September 3, 1998, and the volcanic activity of Mount Iwate, Japan. *Geophysical Research Letters*, 27(2), 269–272.
- Obermann, A., Froment, B., Campillo, M., Larose, E., Planès, T., Valette, B., ... Liu, Q. Y. (2014). Seismic noise correlations to image structural and mechanical changes associated with the Mw 7.9 2008 Wenchuan earthquake. *Journal of Geophysical Research*, 119(4), 3155–3168. <https://doi.org/10.1002/2013JB010932>.
- Obermann, A., Kraft, T., Larose, E., & Wiemer, S. (2015). Potential of ambient seismic noise techniques to monitor the St. Gallen geothermal site (Switzerland). *Journal of Geophysical Research*, 120(6), 4301–4316. <https://doi.org/10.1002/2014JB011817>.
- Obermann, A., Planès, T., Hadzioannou, C., & Campillo, M. (2016). Lapse-time-dependent coda-wave depth sensitivity to local velocity perturbations in 3-D heterogeneous elastic media. *Geophysical Journal International*, 207(1), 59–66.
- Obermann, A., Planès, T., Larose, E., & Campillo, M. (2013). Imaging pre- and co-eruptive structural and mechanical changes on a volcano with ambient seismic noise. *Journal of Geophysical Research*, 118(12), 6285–6294.
- Obermann, A., Planès, T., Larose, E., & Campillo, M. (2018). 4-D imaging of subsurface changes with coda waves: Numerical studies of 3-D combined sensitivity kernels and applications to the Mw 7.9, 2008 Wenchuan earthquake. *Pure and Applied Geophysics*, 176(3), 1–12. <https://doi.org/10.1007/s0024-018-2014-7>.
- Obermann, A., Planès, T., Larose, E., Sens-Schönfelder, C., & Campillo, M. (2013). Depth sensitivity of seismic coda waves to velocity perturbations in an elastic heterogeneous medium. *Geophysical Journal International*, 194(1), 372–382.
- Olivier, G., Brenguier, F., Campillo, M., Roux, P., Shapiro, N. M., & Lynch, R. (2015). Investigation of coseismic and postseismic processes using in situ measurements of seismic velocity variations in an underground mine. *Geophysical Research Letters*, 42(21), 9261–9269.
- Olivier, G., Brenguier, F., Carey, R., & Donaldson, C. (2019). Decrease in seismic velocity observed prior to the 2018 eruption of Kilauea volcano with ambient seismic noise interferometry. *Geophysical Research Letters*, 46, 3734–3744.
- Olivier, G., Brenguier, F., de Wit, T., & Lynch, R. (2017). Monitoring the stability of tailings dam walls with ambient seismic noise. *The Leading Edge*, 36(4), 350a1–350a6.
- Pacheco, C., & Snieder, R. (2005). Time-lapse travel time change of multiply scattered acoustic waves. *The Journal of the Acoustical Society of America*, 118, 1300–1310.
- Paul, A., Campillo, M., Margerin, L., Larose, E., & Derode, A. (2005). Empirical synthesis of time-asymmetrical green functions from the correlation of coda waves. *Journal of Geophysical research*, 110(B8), B08302.
- Peng, Y., & Rubin, A. M. (2016). High-resolution images of tremor migrations beneath the Olympic Peninsula from stacked array of arrays seismic data. *Geochemistry, Geophysics, Geosystems*, 17(2), 587–601.
- Peng, Z., & Ben-Zion, Y. (2006). Temporal changes of shallow seismic velocity around the Karadere-Düzce branch of the north Anatolian fault and strong ground motion. *Pure and Applied Geophysics*, 163(2–3), 567–600.
- Perton, M., Sánchez-Sesma, F. J., Rodríguez-Castellanos, A., Campillo, M., & Weaver, R. L. (2009). Two perspectives on equipartition in diffuse elastic fields in three dimensions. *The Journal of the Acoustical Society of America*, 126(3), 1125–1130.
- Picozzi, M., Parolai, S., Mucciarelli, M., Milkereit, C., Bindi, D., Ditommaso, R., ... Zschau, J. (2011). Interferometric analysis of strong ground motion for structural health monitoring: The example of the L'Aquila, Italy, seismic sequence of 2009. *Bulletin of the Seismological Society of America*, 101(2), 635–651.

- Planès, T., & Larose, E. (2013). A review of ultrasonic CodaWave interferometry in concrete. *Cement and Concrete Research*, 53, 248–255.
- Planès, T., Larose, E., Margerin, L., Rossetto, V., & Sens-Schönfelder, C. (2014). Decorrelation and phase-shift of coda waves induced by local changes: Multiple scattering approach and numerical validation. *Waves in Random and Complex Media*, 2(24), 1–27.
- Planès, T., Larose, E., Rossetto, V., & Margerin, L. (2015). Imaging multiple local changes in heterogeneous media with diffuse waves. *The Journal of the Acoustical Society of America*, 2(137), 660–667.
- Planès, T., Mooney, M., Rittgers, J., Parekh, M., Behm, M., & Snieder, R. (2016). Time-lapse monitoring of internal erosion in earthen dams and levees using ambient seismic noise. *Géotechnique*, 66(4), 301–312.
- Planès, T., Obermann, A., Atunes, V., & Lupi, M. (2019). Ambient-noise tomography of the greater Geneva Basin in a geothermal exploration context. *Geophysical Journal International*.
- Poli, P., Campillo, M., & Pedersen, H. A. POLENET LAPNET Working Group. (2012). Body-wave imaging of Earth's mantle discontinuities from ambient seismic noise. *Science*, 338(6110), 1063–1065.
- Poli, P., Pedersen, H. A., & Campillo, M. (2012). Emergence of body waves from cross-correlation of seismic noise. *Geophysical Journal International*, 188(B7), 549–558.
- Popovics, J. S., & Rose, J. L. (1994). A survey of developments in ultrasonic NDE of concrete. *IEEE Transactions on Ultrasonics, Ferroelectrics, and Frequency Control*, 41(1), 140–143.
- Poupinet, G., Ellsworth, W. L., & Frechet, J. (1984). Monitoring velocity variations in the crust using earthquake doublets: An application to the Calaveras fault, California. *Journal of Geophysical Research*, 89(B7), 5719–5731.
- Ratdomopurbo, A., & Poupinet, G. (1995). Monitoring a temporal change of seismic velocity in a volcano: Application to the 1992 eruption of Mt. Merapi (Indonesia). *Geophysical Research Letters*, 22(7), 775–778.
- Renalier, F., Jongmans, D., Campillo, M., & Bard, P. Y. (2010). Shear wave velocity imaging of the Avignonet landslide (France) using ambient noise cross correlation. *Journal of Geophysical Research: Earth Surface*, 115(F3), 1–14.
- Richter, T., Sens-Schönfelder, C., Kind, R., & Asch, G. (2014). Comprehensive observation and modeling of earthquake and temperature-related seismic velocity changes in northern Chile with passive image interferometry. *Journal of Geophysical Research: Solid Earth*, 119(6), 4747–4765.
- Ringdal, F., & Bungum, H. (1977). Noise level variation at NORSTAR and its effect on detectability. *Bulletin of the Seismological Society of America*, 67(2), 479–492.
- Rivet, D., Brenguier, F., & Cappa, F. (2015). Improved detection of preeruptive seismic velocity drops at the Piton de La Fournaise volcano. *Geophysical Research Letters*, 42(15), 6332–6339.
- Rivet, D., Brenguier, F., Clarke, D., Shapiro, N. M., & Peltier, A. (2014). Long-term dynamics of Piton de la Fournaise volcano from 13 years of seismic velocity change measurements and GPS observations. *Journal of Geophysical Research: Solid Earth*, 119(10), 7654–7666.
- Rivet, D., Campillo, M., Shapiro, N. M., Cruz-Atienza, V., Radiguet, M., Cotte, N., & Kostoglodov, V. (2011). Seismic evidence of nonlinear crustal deformation during a large slow slip event in Mexico. *Geophysical Research Letters*, 38, L08308.
- Roman, D. C. (2017). Automated detection and characterization of harmonic tremor in continuous seismic data. *Geophysical Research Letters*, 44(12), 6065–6073.
- Rossetto, V., Margerin, L., Planès, T., & Larose, E. (2011). Locating a weak change using diffuse waves: Theoretical approach and inversion procedure. *Journal of Applied Physics*, 109(034903), 1–11.

- Roux, P., & Kuperman, W. A. the NPAL Group. (2004). Extracting coherent wave fronts from acoustic ambient noise in the ocean. *The Journal of the Acoustical Society of America*, 116(4), 1995–2003. <https://doi.org/10.1121/1.1797754>.
- Roux, P., Sabra, K. G., Gerstoft, P., & Kuperman, W. A. (2005). P-waves from cross-correlation of seismic noise. *Geophysical Research Letters*, 32, L19303.
- Ruigrok, E., Campman, X., & Wapenaar, K. (2011). Extraction of P-wave reflections from microseisms. *Comptes Rendus Geoscience*, 343, 512–525.
- Sabra, K. G., Conti, S., Roux, P., & Kuperman, W. A. (2007). Passive in vivo elastography from skeletal muscle noise. *Applied Physics Letters*, 90(19), 194101.
- Sabra, K. G., Gerstoft, P., Roux, P., Kuperman, W. A., & Fehler, M. (2005). Extracting time domain Green's function estimates from ambient seismic noise. *Geophysical Research Letters*, 32, L03310.
- Sabra, K. G., Roux, P., & Kuperman, W. A. (2005). Emergence rate of the time-domain-Green's function from the ambient noise cross-correlation function. *The Journal of the Acoustical Society of America*, 118(6), 3524–3531. <https://doi.org/10.1121/1.2109059>.
- Salvermoser, J., Hadzioannou, C., & Stähler, S. (2015). Structural monitoring of a highway bridge using passive noise recordings from street traffic. *The Journal of the Acoustical Society of America*, 138(6), 3864–3872.
- Sanchez-Pastor, P., Obermann, A., & Schimmel, M. (2018). Detecting and locating precursory signals during the 2011 El Hierro, Canary Islands, submarine eruption. *Geophysical Research Letters*, 45(10), 288–297. <https://doi.org/10.1029/2018GL079550>.
- Sanchez-Pastor, P., Obermann, A., Schimmel, M., Weemstra, C., Verdel, A., & Jousset, P. (2019). Short- and long-term variations in the Reykjanes geothermal reservoir from seismic noise interferometry. *Geophysical Research Letters*, 46, 5788–5798. <http://doi.org/10.1029/2019GL082352>.
- Sandrin, L., Catheline, S., Tanter, M., Hennequin, X., & Fink, M. (1999). Time-resolved pulsed elastography with ultrafast ultrasonic imaging. *Ultrasonic imaging*, 21(4), 259–272.
- Sato, H. (1977). Energy propagation including scattering effects, single isotropic scattering approximation. *Journal of Physics of the Earth*, 25, 27–41.
- Sato, H., Fehler, M. C., & Maeda, T. (2012). *Seismic wave propagation and scattering in the heterogeneous earth*. Berlin, Heidelberg: Springer (Eds.).
- Sawazaki, K., Sato, H., Nakahara, H., & Nishimura, T. (2009). Time-lapse changes of seismic velocity in the shallow ground caused by strong ground motion shock of the 2000 Western-Tottori earthquake, Japan, as revealed from coda deconvolution analysis. *Bulletin of the Seismological Society of America*, 99(1), 352–366.
- Sawazaki, K., & Snieder, R. (2013). Time-lapse changes of P-and S-wave velocities and shear wave splitting in the first year after the 2011 Tohoku earthquake, Japan: Shallow subsurface. *Geophysical Journal International*, 193(1), 238–251.
- Saygin, E., & Kennett, B. (2010). Ambient seismic noise tomography of Australian continent. *Tectonophysics*, 481, 116–125.
- Schaff, D. P., & Beroza, G. C. (2004). Coseismic and postseismic velocity changes measured by repeating earthquakes. *Journal of Geophysical Research*, 109, B10302.
- Scherbaum, F. (1987a). Seismic imaging of the site response using microearthquake recordings. Part II. Application to the Swabian Jura, Southwest Germany, seismic network. *Bulletin of the Seismological Society of America*, 77(6), 1924–1944.
- Scherbaum, F. (1987b). Seismic imaging of the site response using microearthquake recordings. part i. method. *Bulletin of the Seismological Society of America*, 77(6), 1905–1923.
- Schimmel, M., Stutzmann, E., Ardhuin, F., & Gallart, J. (2011). Polarized Earth's ambient microseismic noise. *Geochem. Geophys. Geosyst.*, 12(7). <https://doi.org/10.1029/2011GC003661>.
- Schurr, D. P., Kim, J.-Y., Sabra, K. G., & Jacobs, L. J. (2011). Damage detection in concrete using coda wave interferometry. *NDT & E International*, 44(8), 728–735.

- Schuster, G. (2009). *Seismic interferometry*. Cambridge University Press.
- Schuster, G. T. (2001). Theory of daylight/interferometric imaging-tutorial. *63rd EAGE conference & exhibition*.
- Sens-Schönenfelder, C., Pomponi, E., & Peltier, A. (2014). Dynamics of Piton de la Fournaise volcano observed by passive image interferometry with multiple references. *Journal of Volcanology and Geothermal Research*, 276, 32–45.
- Sens-Schönenfelder, C., & Wegler, U. (2006). Passive image interferometry and seasonal variations of seismic velocities at Merapi Volcano, Indonesia. *Geophysical Research Letters*, 33(21), L21302.
- Seydoux, L., de Rosny, J., & Shapiro, N. M. (2017). Pre-processing ambient noise cross-correlations with equalizing the covariance matrix eigenspectrum. *Geophysical Journal International*, 210, 1432–1449. <https://doi.org/10.1093/gji/ggx250>.
- Shapiro, N. M., & Campillo, M. (2004). Emergence of broadband Rayleigh waves from the correlations of ambient seismic noise. *Geophysical Research Letters*, 31(7), L07614.
- Shapiro, N. M., Campillo, M., Margerin, L., Singh, S. K., Kostoglodov, V., & Pachero, J. (2000). The energy partitioning and the diffuse character of the seismic coda. *Bulletin of the Seismological Society of America*, 90, 655–665.
- Shapiro, N. M., Campillo, M., Stehly, L., & Ritzwoller, M. H. (2005). High-resolution surface wave tomography from ambient seismic noise. *Science*, 307(5715), 1615–1618.
- Shokouhi, P., Zoëga, A., & Wiggenhauser, H. (2010). Nondestructive investigation of stress-induced damage in concrete. *Advances in Civil Engineering*, 2010, 1–9, 740189.
- Singh, S. K., & Hermann, R. B. (1983). Regionalization of crustal Q in the continental United States. *Journal of Geophysical Research*, 88, 527–538.
- Snieder, R. (2006). The theory of coda wave interferometry. *Pure and Applied Geophysics*, 163(2), 455–473.
- Snieder, R., Grêt, A., Douma, H., & Scales, J. (2002). Coda wave interferometry for estimating nonlinear behavior in seismic velocity. *Science*, 295(5563), 2253–2255.
- Soldati, G., Zaccarelli, L., Faenza, L., & Michelini, A. (2015). Monitoring of crustal seismic velocity variations in the L'Aquila fault zone inferred from noise cross-correlation. *Geophysical Journal International*, 202(1), 604–611.
- Stähler, S. C., Sens-Schönenfelder, C., & Niederleithinger, E. (2011). Monitoring stress changes in a concrete bridge with coda wave interferometry. *The Journal of the Acoustical Society of America*, 129(4), 1945–1952.
- Stehly, L., Campillo, M., & Shapiro, N. M. (2006). A study of the seismic noise from its long-range correlation properties. *Journal of Geophysical Research*, 111, 1–12.
- Stehly, L., Cupillard, P., & Romanowicz, B. (2011). Towards improving ambient noise tomography using simultaneously curvelet denoising filters and SEM simulations of qseismic ambient noise. *Comptes Rendus Geoscience*, 343, 591–599. <https://doi.org/10.1016/j.crte.2011.03.005>.
- Stehly, L., Froment, B., Campillo, M., Liu, Q. Y., & Chen, J. H. (2015). Monitoring seismic wave velocity changes associated with the Mw 7.9 Wenchuan earthquake: Increasing the temporal resolution using curvelet filters. *Geophysical Journal International*, 201(3), 1939–1949.
- Stutzmann, E., Schimmel, M., Patau, G., & Maggi, A. (2009). Global climate imprint on seismic noise. *Geochemistry, Geophysics, Geosystems*, 10(11). <https://doi.org/10.1029/2009GC002619>.
- Taira, T., Nayak, A., Brenguier, F., & Manga, M. (2018). Monitoring reservoir response to earthquakes and fluid extraction, Salton Sea geothermal field, California. *Sci Adv*, 4(1), 1–11. <https://doi.org/10.1126/sciadv.1701536>.
- Takagi, R., Okada, T., Nakahara, H., Umino, N., & Hasegawa, A. (2012). Coseismic velocity change in and around the focal region of the 2008 Iwate–Miyagi Nairiku earthquake. *Journal of Geophysical Research*, 117(B06315).

- Tanimoto, T., Ishimaru, S., & Alvizuri, C. (2006). Seasonality of particle motion of microseisms. *Geophysical Journal International*, 166, 253–266. <https://doi.org/10.1111/j.1365-246X.2006.02931.x>.
- Tarantola, A., & Valette, B. (1982). Generalized nonlinear inverse problems solved using the least squares criterion. *Revista Geográfica*, 20(2), 219–232.
- Tolman, H. L. (2014). *User manual and documentation of WAVEWATCH-III version 4.18*.
- Tsai, V. C. (2011). Understanding the amplitudes of noise correlation measurements. *Journal of Geophysical Research*, 116, B09311.
- Tsai, V. C., & Moschetti, M. C. (2010). An explicit relationship between time-domain noise correlation and spatial autocorrelation (SPAC) results. *Geophysical Journal International*, 182, 454–460. <https://doi.org/10.1111/j.1365-246X.2010.04633.x>.
- Van Beek, V. M., De Bruijn, H. T. J., Knoeff, J. G., Bezuijen, A., & Förster, U. (2010). Levee failure due to piping: A full-scale experiment (pp. 283–292). *Scour and erosion*.
- van Rossum, M. W. C., & Nieuwenhuizen, T. M. (1999). Multiple scattering of classical waves: Microscopy, mesoscopy and diffusion. *Reviews of Modern Physics*, 71, 313.
- Villasenor, A., Yang, Y., Ritzwoller, M. H., & Gallart, J. (2007). Ambient noise surface wave tomography of the Iberian Peninsula: Implications for shallow seismic structure. *Geophysical Research Letters*, 34, L11304.
- Wang, Q.-Y., Brenguier, F., Campillo, M., Lecointre, A., Takeda, T., & Aoki, Y. (2017). Seasonal crustal seismic velocity changes throughout Japan. *Journal of Geophysical Research: Solid Earth*, 122(10), 7987–8002.
- Wang, Y., Luo, Y., & Schuster, G. T. (2009). Interferometric interpolation of missing seismic data. *Geophysics*, 74(3), SI37–SI45.
- Wapenaar, K., Draganov, D., & Robertsson, J. O. A. (2008). *Seismic interferometry: History and present status*. Society of Exploration Geophysicists.
- Wapenaar, K., Draganov, D., Snieder, R., Campman, X., & Verdel, A. (2010). Tutorial on seismic interferometry: Part 1 Basic principles and applications. *Geophysics*, 75(5), 75A195–75A209.
- Wapenaar, K., Slob, E., Snieder, R., & Curtis, A. (2010). Tutorial on seismic interferometry: Part 2 Underlying theory and new advances. *Geophysics*, 75(5), 75A211–75A227.
- Ward, K. M., Porter, R. C., Zandt, G., Beck, S. L., Wagner, L. S., Minaya, E., & Tavera, H. (2013). Ambient noise tomography across the Central Andes. *Geophysical Journal International*, 194(3), 1559–1573.
- Weaver, R. L. (1982). On diffuse waves in solid media. *The Journal of the Acoustical Society of America*, 71, 1608–1609.
- Weaver, R. L., Froment, B., & Campillo, M. (2009). On the correlation of non-isotropically distributed ballistic scalar diffuse waves. *The Journal of the Acoustical Society of America*, 126(4), 1817–1826. <https://doi.org/10.1121/1.3203359>.
- Weaver, R. L., & Lobkis, O. I. (2001). Ultrasonics without a source: Thermal fluctuation correlations at MHz frequencies. *Physical Review Letters*, 87(13), 134301.
- Wegler, U., Nakahara, H., Sens-Schönfelder, C., Korn, M., & Shiomi, K. (2009). Sudden drop of seismic velocity after the 2004 Mw 6.6 mid-Niigata earthquake, Japan, observed with passive image interferometry. *Journal of Geophysical Research: Solid Earth*, 114(B6), 1–11.
- Wegler, U., & Sens-Schönfelder, C. (2007). Fault zone monitoring with passive image interferometry. *Geophysical Journal International*, 168, 1029–1033.
- Willis, M. E., Lu, R., Campman, X., Nafi Toksöz, M., Zhang, Y., & Hoop, M. V. d. (2006). A novel application of time-reversed acoustics: Salt-dome flank imaging using walkaway VSP surveys. *Geophysics*, 71(2), A7–A11.
- Wills, P. B., Hatchell, P. J., & Bourne, S. J. (2008). Time-lapse measurements of shallow horizontal wave velocity over a compacting field. In *70th EAGE conference and exhibition incorporating SPE EUROPEC 2008*.

- Withers, M. M., Aster, R. C., Young, C. J., & Chael, E. P. (1996). High-frequency analysis of seismic background noise as a function of wind speed and shallow depth. *Bulletin of the Seismological Society of America*, 86(5), 1507–1515.
- Wu, C., Delorey, A., Brenguier, F., Hadzioannou, C., Daub, E. G., & Johnson, P. (2016). Constraining depth range of S wave velocity decrease after large earthquakes near Parkfield, California. *Geophysical Research Letters*, 43(12), 6129–6136.
- Wunderlich, C., & Niederleitinger, E. (2013). Evaluation of temperature influence on ultrasound velocity in concrete by coda wave interferometry. *Nondestructive testing of materials and structures* (pp. 227–232). Springer.
- Xiao, X., Zhou, M., & Schuster, G. T. (2006). Salt-flank delineation by interferometric imaging of transmitted P-to-S-waves. *Geophysics*, 71(4), SI197–SI207.
- Yang, Y., Li, A., & Ritzwoller, M. H. (2008). Crustal and uppermost mantle structure in southern Africa revealed from ambient noise and teleseismic tomography. *Geophysical Journal International*, 174(1), 235–248.
- Yang, Y., & Ritzwoller, M. H. (2008). Characteristics of ambient seismic noise as a source for surface wave tomography. *Geochemistry, Geophysics, Geosystems*, 9, Q02008.
- Yang, Y., Ritzwoller, M. H., Lin, F. C., Moschetti, M. P., & Shapiro, N. M. (2008). The structure of the crust and uppermost mantle beneath the Western US revealed by ambient noise and earthquake tomography. *Journal of Geophysical Research*, 113, B12310.
- Yang, Y. J., Ritzwoller, M. H., Levshin, A. L., & Shapiro, N. M. (2007). Ambient noise Rayleigh wave tomography across Europe. *Geophysical Journal International*, 168(1), 259–274.
- Yao, H., van der Hilst, R. D., & de Hoop, M. V. (2006). Surface-wave array tomography in SE Tibet from ambient seismic noise and two-station analysis: Phase velocity maps. *Geophysical Journal International*, 166, 732–744.
- Young, C. J., Chael, E. P., Withers, M. M., & Aster, R. C. (1996). A comparison of the high-frequency (>1 Hz) surface and subsurface noise environment at three sites in the United States. *Bulletin of the Seismological Society of America*, 86(5), 1516–1528.
- Yu, J., & Schuster, G. T. (2006). Crosscorrelogram migration of inverse vertical seismic profile data. *Geophysics*, 71(1), S1–S11.
- Zhan, Z., Ni, S., Helmberger, D. V., & Clayton, R. W. (2010). Retrieval of Moho reflected shear wave arrivals from ambient seismic noise. *Geophysical Journal International*, 1, 408–420.
- Zhan, Z., Tsai, V. C., & Clayton, R. W. (2013). Spurious velocity changes caused by temporal variations in ambient noise frequency content. *Geophysical Journal International*, 194, 1574–1581. <https://doi.org/10.1093/gji/ggt170>.
- Zhang, P. Z., Wen, X. Z., Shen, Z. K., & Chen, J. H. (2010). Oblique, high-angle, listric-reverse faulting and associated development of strain: The Wenchuan earthquake of May 12, 2008, Sichuan, China. *Annual Review of Earth and Planetary Sciences*, 38, 353–382. <https://doi.org/10.1146/annurev-earth-040809-152602>.
- Zhang, Y., Abraham, O., Larose, E., Planes, T., Le Duff, A., Lascoup, B., & Durand, O. (2011). Following stress level modification of real size concrete structures with coda wave interferometry (CWI). *AIP conference proceedings: Vol. 1335* (pp. 1291–1298).
- Zhang, Y., Abraham, O., Tournat, V., Le Duff, A., Lascoup, B., Loukili, A., ... Durand, O. (2013). Validation of a thermal bias control technique for Coda Wave Interferometry (CWI). *Ultrasonics*, 53(3), 658–664.
- Zhang, Y., Planès, T., Larose, E., Obermann, A., Rospars, C., & Moreau, G. (2016). Diffuse ultrasound monitoring of stress and damage development on a 15-ton concrete beam. *The Journal of the Acoustical Society of America*, 139(4), 1691–1701.
- Zheng, S. H., Sun, X. L., Song, X. D., Yang, Y. J., & Ritzwoller, M. H. (2008). Surface wave tomography of China from ambient seismic noise correlation. *Geochemistry, Geophysics, Geosystems*, 9, Q05020.

- Zhou, R., Huang, L., Rutledge, J. T., Fehler, M., Daley, T. M., & Majer, E. L. (2010). Coda-wave interferometry analysis of time-lapse VSP data for monitoring geological carbon sequestration. *International Journal of Greenhouse Gas Control*, 4(4), 679–686.
- Zorgani, A., Souchon, R., Dinh, A.-H., Chapelon, J.-Y., Ménager, J.-M., Lounis, S., ... Catheline, S. (2015). Brain palpation from physiological vibrations using MRI. *Proceedings of the National Academy of Sciences*, 112(42), 12917–12921.
- Zwartjes, P. M., Wills, P., De Maag, J. W., & Hatchell, P. (2008). Shallow and deep time-lapse effects on valhall lofs converted wave data. *70th EAGE conference and exhibition incorporating SPE EUROPEC 2008*.